

**BOROHYDRIDE-BASED SOLID ELECTROLYTES AND
POLYMER COMPOSITE SEPARATORS FOR LITHIUM-ION
BATTERIES**

A Dissertation
Presented to
The Academic Faculty

by

Aashray Narla

In Partial Fulfillment
of the Requirements for the Degree
Doctor of Philosophy in the
School of Materials Science and Engineering

Georgia Institute of Technology
December 2023

COPYRIGHT © 2023 BY AASHRAY NARLA

**BOROHYDRIDE-BASED SOLID ELECTROLYTES AND
POLYMER COMPOSITE SEPARATORS FOR LITHIUM-ION
BATTERIES**

Approved by:

Dr. Gleb Yushin, Advisor
School of Materials Science and
Engineering
Georgia Institute of Technology

Dr. Seung Soon Jang
School of Materials Science and
Engineering
Georgia Institute of Technology

Dr. Faisal Alamgir
School of Materials Science and
Engineering
Georgia Institute of Technology

Dr. Alexander Alexeev
School of Mechanical Engineering
Georgia Institute of Technology

Dr. Preet Singh
School of Materials Science and
Engineering
Georgia Institute of Technology

Date Approved: [Dec 01, 2023]

[To the students of the Georgia Institute of Technology]

ACKNOWLEDGEMENTS

First and foremost, I would like to thank my advisor, Dr. Gleb Yushin for I could not have accomplished this PhD without your counsel, motivation, knowledge, prowness, and patience. It has been a great journey working with you in the last five years and the experience will be a life-long inspiration for me. I would also like to thank the committee members of my dissertation: Dr. Alamgir, Dr. Singh, Dr. Alamgir, Dr. Jang and Dr. Alexeev for your time and valuable feedback.

There are many former and current members in the Yushin group who have helped and motivated me throughout my PhD journey. I would like to thank Yiran and Kostia for educating me on solid electrolytes, teaching me how to get around doing experiments and discussing various aspects of the projects. I would like thank Ah-Young and Doyoub in helping me out with data analysis and experimental setups and Rebecca for discussing various aspects of my project. I had the opportunity to work and mentor undergraduate students over the last five years who have helped immensely: Alp, Mohammed and Shaunak.

I would like to thank other former and current group members who helped me throughout my PhD study: Samik, Wenbin, Wenqiang, Yice, Kevin, Juzef and Sasha and many others. I would also like to thank my friends from MSE who helped me study for classes and prepare for the qualifying exam: Katie, Keara, Blake, Chris, Venkat, and Rupesh.

I have had the opportunity to make great friends from the lab and outside who have made my PhD journey a lot smoother by being there for me during all my adversities. Ashwin, Billy, Vismay, Abiram, Rizky, Fujia and Munir have been great friends who all I hope to continue to banter with everyday.

Lastly, I would like to extend my gratitude to my parents and my brother for their unconditional love, trust, encouragement, and everything they did for me. I would not be the person I am today without your sacrifices.

TABLE OF CONTENTS

ACKNOWLEDGEMENTS	iv
LIST OF TABLES	viii
LIST OF FIGURES	ix
LIST OF SYMBOLS AND ABBREVIATIONS	xiv
SUMMARY	xvii
CHAPTER 1. Introduction	1
1.1 Motivation for Solid Electrolytes	1
1.2 Motivation for New Separator Technology	6
1.3 Dissertation Overview	8
CHAPTER 2. Background	9
2.1 Introduction to Lithium-Ion Batteries (LIBs)	9
2.1.1 Introduction and Overview	9
2.1.2 Active Materials – Cathodes and Anodes	15
2.1.3 Electrolytes	18
2.2 Inactive LIB Components	20
2.2.1 Separators	20
2.2.2 Binders	21
2.2.3 Current Collectors	22
2.2.4 Carbon Additives	22
2.3 Solid Electrolytes for LIBs	23
2.4 Methods and Characterization	28
2.4.1 Coin Cell Preparation	28
2.4.2 Scanning Electron Microscopy (SEM)	29
2.4.3 Transmission Electron Microscope (TEM)	30
2.4.4 X-Ray Diffraction (XRD)	30
2.4.5 X-Ray Photoelectron Spectroscopy (XPS)	31
2.4.6 Differential Scanning Calorimetry (DSC)	32
2.4.7 Electrochemical Characterization	33
CHAPTER 3. Anion Substituted Borohydride-based Solid electrolytes for high energy lithium ion batteries.	37
3.1 Introduction and Background	37
3.2 Experimental Methods of Anion Substituted Borohydride Based Solid Electrolytes	45
3.2.1 Synthesis of Anion Substituted Borohydride SSEs	45
3.2.2 SSE Characterization	46
3.2.3 Electrochemical Characterization	47
3.3 Results and Discussion	49

3.3.1	Synthesis of Melt-Synthesized Borohydride Based SSEs	49
3.3.2	Electrochemical testing for Ionic Conductivity and Cyclic Voltammetry.	60
3.3.3	Electrochemical performance of All-Solid-State Batteries with 3LiBH ₄ -LiCl	74
3.4	Conclusions	89
CHAPTER 4. A Nanodiamond-Enhanced Nanofiber Separator for High-Energy Lithium-Ion Batteries		91
4.1	Introduction and Background	91
4.2	Experimental Section	94
4.2.1	Preparation of ND-functionalized membranes	94
4.2.2	Materials characterizations	95
4.2.3	Cell assembly and electrochemical tests	97
4.3	Results and discussion	97
4.4	Conclusion	111
CHAPTER 5. Conclusions and Future Work		113
5.1	Anion Substituted Borohydride-based Solid Electrolytes for High Energy Lithium-Ion Batteries (LIBs)	113
5.1.1	Conclusions	113
5.1.2	Future Work Directions	114
5.2	A Nanodiamond Enhanced Separator for High Energy Dense Lithium Ion Batteries (LIBs)	115
5.2.1	Conclusions	115
5.2.2	Future Work	116
APPENDIX A. Permission Licenses for the Reuse of Copyright Materials		118
REFERENCES		122

LIST OF TABLES

Table 1. Summary of studies on halide-based and pure LiBH_4 in various cell architectures
40

LIST OF FIGURES

Figure 1. Graphic representation of ISEs half cells using composite cathodes containing a mixture SSE, and active materials. ^[6]	4
Figure 2. Graphic representation of a LIB using a graphite anode and LCO cathode. ^[14]	10
Figure 3. Transport of oxidants towards the electrode (in grey) which is subsequently adsorbed onto the surface. After the electrochemical reaction takes place, due to a concentration gradient, the reduced product is transported back to the bulk of electrolyte.	12
Figure 4. Movement of Li-ions along, across and through the grain boundaries. Generally, Li-ion conduction through the grains is very low. ^[58]	24
Figure 5. Coin cell fabrication schematic and systematic assembly. ^[75]	28
Figure 6. Constructive interferences of x-rays demonstrated through Bragg's law. ^[76]	31
Figure 7. Schematic diagram of an XPS. A hemispherical analyzer is used to detect the irradiated electrons. ^[77]	32
Figure 8. Example heat flow of a polymer during DSC measurements.	33
Figure 9. Randles equivalent circuit representation.	35
Figure 10. Nyquist plot of a Randles equivalent circuit with a diffusion element.	36
Figure 11. Low temperature phase polymorph of LiBH_4 , with lithium ions present in the tetrahedral positions with the BH_4^- anions layered to form an orthorhombic structure. ^[84]	38
Figure 12. High temperature phase polymorph of LiBH_4 , with lithium ions distributed along the tetrahedra.	39
Figure 13. The left crystal structure is a representation of the low temperature phase of $\text{Li}_2\text{B}_{10}\text{H}_{10}$ which is cubic ^[105] . The structure on the right is a distorted cubic structure, which suggests the Li-ions are constantly in motion on this disordered Li sublattice, implying that the high temperature $\text{Li}_2\text{B}_{12}\text{H}_{12}$ polymorph is a potential Li^+ superionic conductor ^[102] .	44
Figure 14. Symmetric CR2032 coin cells for EIS testing to measure ionic conductivity.	48
Figure 15. A symmetric CR2032 coin cell with SS (positive electrode) and Li (negative electrode) to measure electronic conductivity.	49

- Figure 16. (a) is a picture of the solid solution in the molten form at 340°C, where we notice a homogenous mixture and part (b) shows the solidification of the electrolyte at room temperature. 50
- Figure 17. (a) SEM image of 3LiBH₄-LiCl and (b) EDS map of the pellet, where red and green color/shades represent boron and chlorine respectively; (c) a LiCl rich phase and (d) EDS map of the LiCl-rich phase, where red and green shades represent boron and chlorine, respectively. 51
- Figure 18. 3LiBH₄-LiCl SSE low temperature orthorhombic phase compared to the high temperature hexagonal phase. 52
- Figure 19. XRD plots of Fluorine, Chlorine, Bromine and Iodine substituted LiBH₄ SSE. Rietveld analysis of these different anion substitute/doped LiBH₄ show the increase in unit volume size with increasing halogen anion size. 54
- Figure 20. (a) Binding energy of LiCl; (b) Binding energy of LiBH₄ and (c) Binding energy of 3LiBH₄-LiCl. 55
- Figure 21. Varying LiCl concentration with LiBH₄ and Reitveld shows saturation of anion substitution at 1:1 ratio of LiBH₄ and LiCl. 57
- Figure 22. DSC isotherms of LiBH₄ substituted with various halide salts and varying LiCl. 58
- Figure 23. Heating and cooling curves of 3LiBH₄-LiCl, with phase transition hysteresis. 59
- Figure 24. Lithium symmetric cell equivalent circuit to fit a Nyquist plot. 61
- Figure 25. A lithium symmetric cell with SSE at 100°C fitted with the equivalent circuit mentioned above. 62
- Figure 26. Nyquist plot of a SS symmetric cells with 3LiBH₄-LiCl, with a diffusive peak which is unique to a blocking electrode case. 63
- Figure 27. Li⁺ ion conductivities of LiBH₄ based SSEs with different halide salts substituted. 64
- Figure 28. Effect of transition temperature hysteresis on ionic conductivity of 3LiBH₄-LiCl SSE. 66
- Figure 29. CV was performed on SSEs sandwiched between SS and Li foil. We have the CV plots for 3LiBH₄-LiCl in this figure. 67

- Figure 30. Formation of lithium dendrites from repeated stripping and plating. First voids are formed and form a 3 interphase point between the solid electrolyte, lithium and the void. These act as nucleation points for lithium dendrites to grow. 69
- Figure 31. Voltage response to current pulses (DC cycling of Li//HPSE//Li) at different current densities. 70
- Figure 32. Voltage response to a current pulse at high current densities (0.5 mA cm^{-2}) and (c) long-term cycling of symmetric cells of $3\text{LiBH}_4\text{-LiCl}$. 71
- Figure 33. XPS analysis of pristine and cycled (Li//HPSE//Li) $3\text{LiBH}_4\text{-LiCl}$. 73
- Figure 34. DSC isotherms of SSE, the electrodes alone and SSE mixed with various active materials. 75
- Figure 35. Melt-infiltration of solid electrolytes into electrodes which drastically reduces processing time and complexity of all solid electrolyte battery.^[119] 76
- Figure 36. (a) melt-infiltrated silicon-carbon composite electrode with $3\text{LiBH}_4\text{-LiCl}$ electrolyte, (b) an EDS map of the cross section image of the infiltrated silicon-carbon anode. The green, blue, red and orange respectively represent chlorine, silicon, oxygen and carbon. (C) a magnified image of a melt-infiltrated silicon-carbon electrode, (d) a respective EDS map of the electrode using the same color scheme as (b). 78
- Figure 37. (a) the half-cell performance of the silicon-carbon anodes using the $3\text{LiBH}_4\text{-LiCl}$ SSE which is cycled between 1 to 0.1V (vs. Li^+/Li). The cell shows great capacity of around 800 mAh g^{-1} ; (b) the voltage profile of the silicon half-cell with respect to the normalized capacity (c) dQ/dV plot of the half-cell to show lithiation and delithiation of lithium into and out of the electrodes. 79
- Figure 38. (a) the half-cell performance of the NCM11 cathode infiltrated with Li_2OHCl and using the $3\text{LiBH}_4\text{-LiCl}$ SSE pellet which is cycled between 3 to 4V (vs. Li^+/Li). The cell shows great capacity of around 100 mAh g^{-1} ; (b) the voltage profile of the NMC111 half-cell with respect to the normalized capacity; (c) is dQ/dV plot of the half-cell to show lithiation and delithiation of lithium into and out of the electrodes. 81
- Figure 39. (a) the half-cell performance of the graphite anodes using the $3\text{LiBH}_4\text{-LiCl}$ SSE which is cycled between 1 to 0.1V (vs. Li^+/Li). The cell shows great capacity of around 100 mAh g^{-1} ; (b) the voltage profile of the silicon half-cell with respect to the normalized capacity (c) dQ/dV plot of the half-cell to show lithiation and delithiation of lithium into and out of the electrodes and (d) the charge discharge plot for graphite cycled between 1 to 0.01V (vs. Li^+/Li). 82
- Figure 40. (a) and (b) silicon-carbon nanocomposite particles after cycling for 50 cycles at 800 mAh g^{-1} between 1V to 0.1V (vs. Li^+/Li); we notice widespread cracking and delamination of the particles from the electrolytes; (c) NCM particles which have

delaminated and cracking after cycling at 100 mAh g^{-1} for 100 cycles and finally; (d) the graphite particles which have delaminated after cycling at 250 mAh g^{-1} for 50 cycles.

Figure 41. (a) comparison of initial discharge capacity of varying mass loading of NMC111; (b) the long term cycling of NMC111 with a mass loading of 1 mg cm^{-2} ; (c) is a long term cycling plot of a higher mass loading full cell; (d) voltage vs normalized capacity curve to study the hysteresis of the cell. 86

Figure 42. (a) EIS curves for a Si half-cell at various cycling times; (b) is the EIS curves for the graphite half-cell at various cycling times; (c) EIS curves for the NMC/SSE/Si-C nanocomposite before and after cycling. 88

Figure 43. (a) Schematic of the synthesis of ND functionalized nanofiber separator and (b) its advantages over traditional polypropylene separator in Li batteries. 99

Figure 44. (a) Photo of produced membranes containing 0 wt.%, 1 wt.% and 5 wt.% NDs; (b) FTIR and (c) XRD profiles of the pristine polymer and composite polymers. 100

Figure 45. (a) SEM and (b-c) TEM images of PVDF-HFP@1%ND. (d) SEM and (e-f) TEM images of PVDF-HFP@5%ND. 101

Figure 46. (a) Thermal stability of different membranes at temperatures from 50 to $175 \text{ }^\circ\text{C}$ (kept 20 min at each temperature); (b) DSC curves of different samples; (c) a shape-retention study of PVDF-HFP@5%ND and PP membranes (area of $\sim 9 \text{ cm}^2$) at $130 \text{ }^\circ\text{C}$ for up to 10 days; (d) strength-strain plots of ND-functionalized PVDF-HFP membranes after hot press. 103

Figure 47. A comparison for the contact angles of ND functionalized and Celgard PP separators after contacting a drop of electrolyte solution for 1 s. 105

Figure 48. DSC cycles and crystallinity of (a) pure PVDF-HFP (0 wt. % ND); (b) PVDF-HFP@1%ND and PVDF-HFP@5%ND membranes; (c) a graphical representation of how semi-crystalline polymer are disrupted by NDs to form disordered polymer chains and reduce crystallinity; (d) Li^+ diffusion coefficients of PVDF-HFP membranes with different mass fractions of NDs calculated by NMR. 105

Figure 49. (a) Cycling performance of Li cells with Celgard 2400 and PVDF-HFP@5%ND separators in the potential range 2.8–4.4 V (vs. Li/Li^+); (b) voltage profiles at different stages of cycling; (c) long-term cycling performance and (d) voltage profile of the cells at C/3 between 2.8–4.2 V (vs. Li/Li^+). 108

Figure 50. (a) LSV curves of Li/separator/stainless steel cells with PP and PVDF-HFP@5%ND separators at a scan rate of 10 mV s^{-1} from 2.5 to 6.5 V (vs. Li/Li^+); (b) voltage hysteresis of the cells using Celgard and PVDF-HFP@5%ND separators. 109

Figure 51. (a) Top-view and (b, c) cross-section SEM images of the Li anode from the cell with PVDF-HFP@5%ND separator after cycling; (d) Top-view and (e, f) cross-section SEM images of the Li anode from the cell with PP separator after cycling. 110

Figure 52. (a) CV curves of the cells with PVDF-HFP@5%ND separator at a scan rate of 0.2 mV s^{-1} ; (b) Nyquist plots of the cells before and after long-term cycling at C/2. 111

Figure 53. ND m-aramid polymer composite with high degree of ND agglomeration. 117

LIST OF SYMBOLS AND ABBREVIATIONS

AM	Active Materials
Al	Aluminum
ASLBs	All-Solid Lithium-ion Batteries
CEI	Cathode Electrolyte Interface
CMC	Carboxymethyl Cellulose
CSE	Composite Solid Electrolyte
Cu	Copper
CV	Cyclic Voltammetry
DEC	Diethyl Carbonate
DMC	Dimethyl Carbonate
DSC	Differential Scanning Calorimetry
EC	Ethylene Carbonate
EMC	Ethylmethyl Carbonate
EIS	Electrochemical Impedance Spectroscopy
ESW	Electrochemical stability Window
EVs	Electric Vehicles
EVTOLs	Electric Vertical Take-off and Landing Aircrafts
FAST	Field Assisted Sintering Technique
FEC	Fluoroethylene Carbonate
HOMO	Highest Occupied Molecular Orbital
ISEs	Inorganic Solid Electrolytes
LCO	Lithium Cobalt Oxide

LE	Liquid Electrolytes
LFP	Lithium Iron Phosphate
LMB	Lithium Metal Batteries
LIBs	Lithium-ion Batteries
LiPON	Lithium Phosphorous OxyNitride
LLZO	Lithium Lanthanum Zirconium Oxide
LUMO	Lowest Unoccupied Molecular Orbital
NASICON	Sodium (NA) Super Ionic CONductor
Nb	Niobium
NCA	Lithium Nickel Cobalt Aluminum Oxide
NDs	Nanodiamonds
Ni	Nickel
NMC	Lithium Nickel Manganese Cobalt Oxide
NMP	N-Methylpyrrolidone
OCV	Open Circuit Voltage
PE	Polyethylene
PP	Polypropylene
PVDF	Polyvinylidene fluoride
PVDF-HFP	Poly(vinylidene fluoride-co-hexafluoropropylene)
SBR	Styrene-Butadiene Rubber
SE	Solid Electrolyte
SEM	Scanning Electron Microscope
SEI	Solid Electrolyte Interphase
SPE	Solid Polymer Electrolyte
SS	Stainless Steel

SSE Solid State Electrolyte
Ta Tantalum
TEM Transmission Electron Microscope
VC Vinylene Carbonate
XPS X-Ray Photoelectron Spectroscopy
XRD x-Ray Diffraction
nm nanometer
A° Angstroms
 μ Chemical Potential
 θ Theta

SUMMARY

Lithium-ion batteries (LIBs) have garnered a lot of interest over the past decade due to their high-energy and power density, prolonged cyclability and long shelf-life. While electric vehicles (EVs) and portable electronics necessitate long range and battery life respectively, we are reaching the limits of energy densities of conventional LIBs that use intercalation active materials and liquid electrolytes. As the current LIB technology additionally relies on highly flammable and toxic electrolytes that are detrimental to the environment, solid electrolyte LIBs have gained more interest over the past years. The solid-state LIBs may offer higher energy densities, lower toxicity and lower flammability compared to their liquid electrolyte equivalents. However, current solid-state electrolytes (SSE) suffer from poor ionic conductivity, low volumetric density, high cost, complicated synthesis, and slow manufacturability at high yields. In this work, we explore low-melting point anion-substituted/doped borohydride SSEs synthesized by a novel melt-synthesis process capable of being quickly manufacturable at high yields. We systematically investigate the structure and composition of various borohydride SSEs and study the key electrochemical properties such as critical current density to realize their use in all solid-state LIBs. We further fabricate all solid-state LIBs using the melt infiltration method, to assess the borohydride solid electrolyte performance with various LIB active materials. The cycling data of such cells presented similar voltage profiles and capacity retentions to the cells of the same electrodes with liquid organic electrolytes. The promising performance characteristics of such cells will open new opportunities for the accelerated adoption of all solid-state LIBs for safer electric vehicles (EVs).

Additionally to the work on SSEs, we study separators for conventional LIBs. Current LIB technology uses separators made from polyolefins, such as polypropylene and polyethylene, which generally tend to suffer from low porosity, low wettability, and slow ionic conductivity and tend to perform poorly against heat-triggering reactions that may cause potentially catastrophic thermal event issues, such as fire. To overcome these limitations, in this dissertation, we report that a porous composite membrane consisting of poly(vinylidene fluoride-*co*-hexafluoropropylene) (PVDF-HFP) nanofibers functionalized with nanodiamonds (NDs) that can realize a more thermally resistant, mechanically robust, and ionically conductive separator. We systematically investigate the role of NDs in the polymer matrix of the membrane to improve the thermal, mechanical, crystalline, and electrochemical properties of the composites. Taking advantages of these mechanistic characteristics, the ND-functionalized nanofiber separator enables high-capacity and stable cycling of lithium anode cells with $\text{LiNi}_{0.8}\text{Mn}_{0.1}\text{Co}_{0.1}\text{O}_2$ (NMC811) as the cathode, much superior to those using conventional polyolefin separators in otherwise identical cells.

CHAPTER 1. INTRODUCTION

1.1 Motivation for Solid Electrolytes

Energy storage has become fundamental to our society, as we see its widespread adoption from consumer electronics to electric vehicles (EVs). Over the past few decades, lithium-ion batteries (LIBs) have become an attractive rechargeable battery chemistry for energy storage for these applications primarily due to their high energy and power density, long shelf life and prolonged cyclability. In addition, LIBs can be efficiently be used to store renewable energy, helping society to move towards a greener and a more sustainable future.

It is essential to develop less toxic, safer, ideally more energy dense LIBs compared to those that rely on conventional polymer separators and organic liquid electrolytes (LE) - based LIBs. The development of high performance and lost-cost all solid-state lithium-ion batteries (ASLBs) may be a promising solution. The use of nonflammable solid-state electrolytes (SSEs) may enhance safety, calendar life and cycle life performance of LIBs. In-addition, SSE-based batteries are more thermally stable and may not require advanced and expensive cooling systems. To ensure that the use of SSEs doesn't increase LIB pack cost and weight, it is important that ASLBs could be sufficiently cheap, lightweight, manufacturable rapidly with high yield at a global scale, and ideally be compatible with existing LIB manufacturing equipment. None of the existing SSE solutions satisfy such criteria. Many crucial issues for performance and scalability still need to be addressed to enable large scale ASLB adoption.

Solid electrolytes can be broadly classified into: (a) inorganics solid electrolytes (ISEs), (b) solid polymer electrolytes (SPEs) and (c) composite solid electrolytes (CSEs). The multi-scale Li^+ conduction is unique to the SSEs fundamental structure. ISEs are crystalline or glassy type SSEs which commonly rely on the presence of vacancies, interstitial sites or correlated interstitials for the movement of Li^+ across crystal units at an atomic scale. On a macroscopic scale, at near room temperature or below Li^+ conduction typically occurs across and along grain boundaries of the SSEs. ISEs can be further distinguished into multiple sub-classes based on their composition, microstructure and properties: sodium (NA) Super Ionic CONductor (NASICON) type, Garnet type, nitride based, perovskites, anti-perovskites, sulfides, chlorides, borohydrides and closo-borohydrides.^[1-3] SPEs are commonly solid solutions of an alkali metal salt (e.g., Li salt) and a polymer where the movement of Li^+ occurs along the polymer chains due to segmental motion of polymer chains. Lastly, composite solid electrolytes use ceramic fillers such as Garnet and NASICON and others in solid polymer electrolytes.^[2, 3]

As different classes of SSEs originate from fundamentally different structures and chemistries, the drawbacks of each of these classes tend to be stem from inherent drawbacks of the structure or chemistry itself. Many ISEs suffer from manufacturing difficulties and mechanical instabilities upon cycling- or operation-induced stresses being brittle ceramics, poor interfacial mechanics due to high melting point and resulting poor and less stable interfacial contact, Li dendrite growth along grain boundaries, particularly at high current densities and complicated fabrication methods, to name a few^[2]. SPEs on the other hand, though being often cheaper and easier to manufacture, suffer from low attainable Li^+ conductivity, poor thermal stability at high operating temperatures, poor

mechanical strength, and poor protection against Li dendrite penetration. The scalable, low-cost manufacturing of ISEs and ISE-based ASLBs remains an important challenge that is yet to be addressed. Typically, cells are made by combining cathode pellets, anode pellets and electrolyte pellets together to form full cells. Cathode or anode composite pellets are a mixture of SSEs, active material, and electrically conductive materials, such as carbon black, graphene or carbon nanotubes (CNTs). High pressure and temperature is used to compress the pellets together to minimize voids and defects, and even cycle the cells stably.^[4] Due to the low deformability of ISEs, electrodes require higher volume and mass fraction of electrolytes relative to liquid electrolyte used in modern LIB manufacturing, which further reduces both volumetric and gravimetric capacities of both electrodes and thus minimize ASLB attainable performance. On a product design level, applying constant high pressure often isn't tenable and practical for consumer products and increases the pack cost and weight for automotive applications. In addition to complicated manufacturing processing, mechanical delamination often occurs during cycling due to volumetric expansion of active materials, which may be an even more serious issue when using conversion type electrodes that exhibit particularly large volume changes. Not many studies have been done on cell cycling of above mentioned ISEs with conversion type electrodes, such as silicon-based anode materials or lithium-sulfide and iron fluoride-based cathode materials.

Although there is work to show long term stability of solid electrolytes with intercalation type electrodes, these electrodes have been typically processed and assembled by high energy ball milling or various high energy physical mixing methods.^[4, 5] These high energy mixing methods aren't easily scalable on an industrial level. Hence, it has

become important to develop new processing techniques that are scalable on an industrial level.

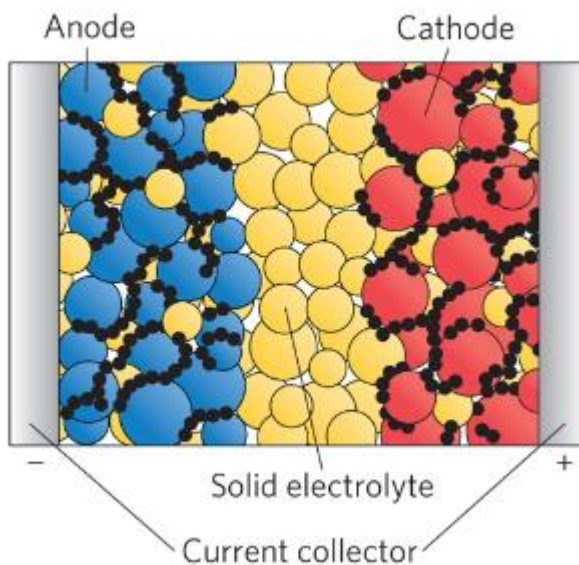


Figure 1. Graphic representation of ISEs half cells using composite cathodes containing a mixture SSE, and active materials.^[6]

Ideally, SSEs need to meet the following requirements: (1) intrinsically have a high Li^+ conductivity, (2.a) be stable across a sufficiently wide electrochemical stability window (ESW) or form stable and ionically conductive passivation layer on the surface of both the anodes and cathodes, (2.b) in case of Li metal batteries – be practically stable in the presence of a Li metal anode and possess sufficient mechanical, structural, thermal and chemical properties to prevent lithium dendrite growth, (3) comprise cheap and abundant materials, (4) allow easy processing/manufacturing of ASLBs, and viable enough for industrial scale up (preferably compatible with conventional LIB manufacturing equipment), (5) be mechanically deformable to a sufficient degree to accommodate volume changes in active materials during battery operation, (6) be thermally stable to operate at

elevated temperatures (e.g., not needed cooling during self-heated upon fast charging or during exothermic side reactions, etc.) and (7) exhibit relatively low density to enable light weight for LIBs.^[7]

Sulfide based ISEs exhibit high ionic conductivity of over $10^{-3} \text{ S cm}^{-1}$ at 60°C , comparable to that of liquid electrolytes, and are soft which assists with reducing the interfacial resistance at active material interfaces but generally suffer from narrow ESWs, moderately high glass transition temperature, 2x higher density relative to liquid organic electrolytes, undesirable reactivity to the environment (e.g., H_2O) producing harmful gases, such as H_2S ^[7]. Similarly, Garnets such as Lithium Lanthanum Zirconium Oxide (LLZO) and other similar SSEs, display high ionic conductivities of over $10^{-3} \text{ S cm}^{-1}$ at 60°C , but are extremely heavy (over 4x higher density relative to liquid organic electrolytes), relatively brittle, sensitive to H_2O , CO , and CO_2 (form resistive layer) and require the use of expensive fabrication and sintering techniques for flawless fabrication. The sintering techniques such as Field Assisted Sintering technique (FAST) and spark assisted sintering, which occur at lower temperatures to reduce lithium diffusion, aren't scalable for large production of highly conductive Garnet type SSEs^[8]. Although Garnet electrolytes have moderately good mechanical properties (e.g., moderately high modulus and fracture toughness), the interfacial stability has always been a hindrance. By products such as Li_2CO_3 and LiOH may be formed in contact with air; acting as resistive layers. Doping LLZO with tantalum (Ta), aluminum (Al) or niobium (Nb) helps to reduce resistance of the solid electrolyte interphase (SEI) on the surface of Li metal anode.^[9, 10] Thin film SSEs such as lithium phosphorous oxynitride (LiPON) and lithium phosphate have garnered a lot of interest over time but for applications limited to micro-batteries/thin film batteries.^[10]

These SSEs are deposited by using energy intensive techniques such as RF/DC sputtering or vapor deposition that become too expensive for large scale production of batteries.^[10] Adding to expensive production costs, they suffer from low ionic conductivity, which isn't functional for fast charging and discharging applications. Metal borohydrides received much less attention from the scientific community in spite being interesting SSE candidates due to their low density (comparable to liquid electrolytes), good mechanical properties, relatively low expected glass transition temperature, facile synthesis, high ionic conductivity (over 10^{-3} S cm⁻¹ at 60°C), and reported stability in contact with Li metal in one recent publication^[11].

1.2 Motivation for New Separator Technology

Lithium-ion batteries (LIBs) are present in most portable device and their adoption in electric vehicles is rising at an exponential rate. LIBs, due to their high energy and power density, have been an attractive energy storage device. LIBs mainly consist of four different parts: (1) porous anode, (2) porous cathode, (3) porous, ionically conductive, and electrically insulative separator and (4) electrolyte infiltrating into both electrodes and the porous separator. Separators play a vital role in battery performance, and as our pursuit to improve energy and power density in LIBs is continuing through better cathodes and anodes, separators must be similarly improved. Separator physically separates the electrodes, and the porosity, the microstructure, surface chemistry, thermal and dimensional stabilities, and the strength of the separator all play important roles in battery life, safety and performance.

Conventional separators are made from thermoplastic polyolefins, such as polyethylene (PE) and polypropylene (PP). They can be produced large scale, but tend to suffer from low porosity, poor thermal stability (shrinking at elevated temperatures), and high tortuosity, which may reduce charging rate capabilities and cause premature failures of cells having high energy density. To illustrate, as LIBs are cycled for extended periods of time, heat-triggered exothermic “thermal runaway” reactions may occur due to large overpotentials present in the cells.^[12, 13] These reactions lead to an overall increase of temperature in the cell, which causes the separator to shrink, the SEI to break down, and eventually an internal short-circuit to form, resulting in explosion and fire in some cases, which is a relatively common shortcoming in PE and PP separators. A separator that minimizes the overpotentials in the first place through a facile conduction of Li^+ , and that is aided with tools (i.e., thermally stable, and able to prevent shrinkage at high temperatures) to dissipate heat in the case of a thermal runaway, is required to reduce the probability of short circuiting, improve cycle life, improve charging rate performance, and ensure safety. Furthermore, a thin, porous, and ionically conductive separator is required for the next-generation LIBs to garner the benefits of high-energy dense electrodes.

Polymer-nanoparticle composites have been of interest for the past two decades as candidates for separators in LIBs. Nanoparticles, inorganic or organic, when embedded in the polymer matrix may improve mechanical, thermal and structural properties of the composite. With widespread availability of nanoparticles such as carbon nanotubes, inorganic nanowires, dendrimers, graphene with tunable size and surface functionalization, there have been significant efforts to improve appropriate properties of the composite for their use as separators in high-energy-density LIBs and lithium metal batteries (LMBs).

Yet, shortcomings such as poor cycle life, large hysteresis, and complicated processing methods, still remain, which calls for further innovation in their chemistry and engineering aspects. Nanodiamonds (NDs) are a relatively unexplored class of carbon nanoparticles featuring high surface-to-volume ratio, tunable size and surface functionalization, high elasticity moduli, and exceptional thermal conductivity. We are interested to study the effects of ND as a filler substance in poly(vinylidene fluoride-co-hexafluoropropylene) (PVDF-HFP) polymer separators in high energy density LIBs and LMBs.

1.3 Dissertation Overview

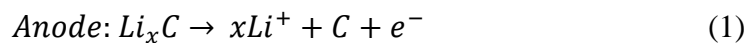
The dissertation overview is mentioned to give an overall structure of the dissertation and detailed background of each project in detail. Chapter 2 provides the review of LIBs and their major components, various characterization methods to understand material properties of LIBs. The background of borohydride based solid electrolytes, their synthesis, their crystal structure, and various performance metrics are discussed in Chapter 3. Chapter 4 consists of the background for separators, introduction to nanodiamonds (NDs), development and synthesis of ND based separators, characterization of ND separators and studying various performance metrics. Finally, Chapter 5 is on the conclusion and future work for the various projects described.

CHAPTER 2. BACKGROUND

2.1 Introduction to Lithium-Ion Batteries (LIBs)

2.1.1 Introduction and Overview

LIBs that are being widely used today, contain four critical parts: (1) anode electrode, (2) cathode electrode, (3) separator and (4) electrolyte infiltrated into both the electrodes and the separator. Anode, cathodes and electrolytes are typically considered to be active components of the LIB, while separators are inactive components of the LIB. Anodes and cathodes are host materials which can store guest ions, through either intercalation or through a redox reaction (conversion materials) between the guest ions.^[14] These guest ions can be stored and removed reversibly.^[14] In a LIB, Li^+ ions are the guest atoms/ions and as we discharge our LIB, Li^+ ions move from the anode to the cathode and during charging, Li^+ ions move from the cathode side to the anode side. To be more specific, during discharge an oxidation reaction occurs at the anode and Li^+ ions are de-intercalated/delithiated from the anode and migrate towards the cathode through the electrolyte and separator. This reaction on the anode occurs at a relatively low electrochemical potential. During charging, an oxidation reaction occurs at the cathode at relatively high electrochemical potentials, where Li^+ ions are de-intercalated/lithiated from the cathode and moves towards the anode. For a lithium cobalt oxide (LCO) cathode and graphite anode-based LIB, these are the following are the reactions at the respective electrodes:



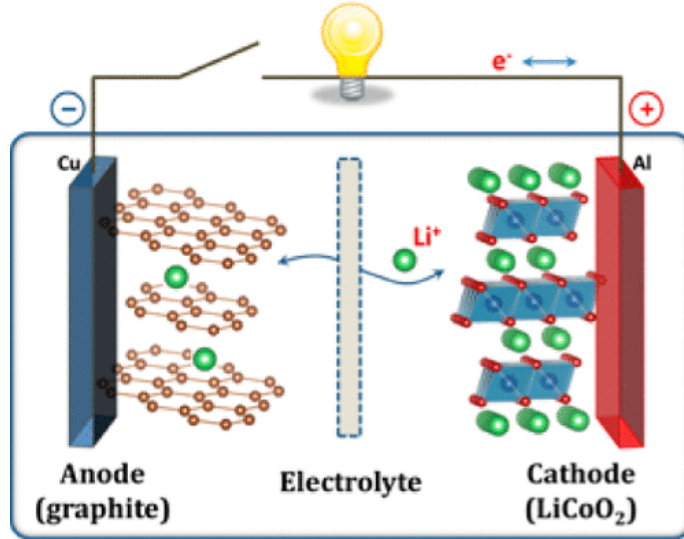
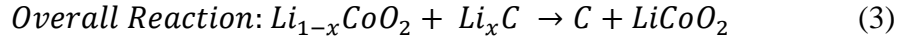
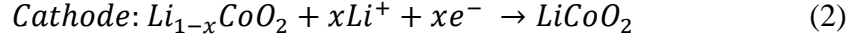


Figure 2. Graphic representation of a LIB using a graphite anode and LCO cathode.^[15]

The number of reactive electrons present/consumed during the reactions is fundamental to deriving the key metrics or characteristics of a LIB. It is important to define some key metrics which demonstrate the efficiency and performance of the active materials such as theoretical capacity, voltage, energy and power density and coulombic efficiency. The voltage, such as an Open Circuit Voltage (OCV), of a LIB is determined by the difference of the chemical potentials of the electrode materials (anode and cathode) which is determined by the redox reaction during lithiation and delithiation (shown in equation 4):^[16]

$$(OCV)V_{oc} = \frac{\mu_A - \mu_C}{e} \quad (4)$$

Where μ_A and μ_C are the chemical potentials of the anode and cathode, respectively, and e is the magnitude of electronic charge. The OCV can be defined as the voltage developed to equalize the chemical potentials of the anode and cathode due to an electric field created when cations move from the anode to cathode (cathode has a positive and anode has negative charge) if electrons are prevented from flowing.^[17] Although, the lithiation and delithiation occur at specific potentials for anodes and cathodes, the maximum working voltage is also dependent on the electrolyte used. The theoretical voltage window of the electrolyte is dependent on the highest occupied molecular orbital (HOMO) and lowest unoccupied molecular orbital (LUMO).^[15] If there is a desire to avoid electrolyte decomposition and if there is no significant electrode/electrolyte interactions, the cathode and anode should be selected such that the chemical potential of cathode and anode should be above the HOMO and below the LUMO of the electrolyte respectively. In reality, however, electrolyte decomposition may induce formation of a passivating solid electrolyte interphase (SEI) on the anode surface and cathode electrolyte interphase (CEI) on the cathode surface, which prevent further decomposition of the electrolyte.^[18] It should also be noted that solvation of electrolyte ions by solvent molecules significantly impact electrolyte oxidation and reduction potentials.

Theoretical capacity (Q measured in mAh g⁻¹) of electrode materials which is a measure of charged stored (an intrinsic property) defines the energy density of an LIB. Theoretical capacity can be expressed with the following equation:^[17]

$$Capacity = C_{Th} = \frac{nF}{3.6 \times M} \quad (5)$$

where n is the number of reactive electrons (or reactive Li^+ ions) per specie (within a potential range an electrode is exposed to during cycling), F is the faraday constant, 3.6 the conversion factor (for the current applied for specific period of time) ($1\text{A.h} = 3600\text{C}$) and M is the molecular weight of the specie.^[19] The capacity of a LIB varies with varying current and the performance of the LIB at different current rates is known as Rate Performance. C/t is the theoretical current that fully charges or discharges the cell in t hour, and we decrease the time for charging and discharging, the current applied to the LIB during charging or discharging increases. As we build large batteries for everyday applications and require quick charging times, larger currents are required to charge faster. With increasing current applied to charge LIBs, resistances within the LIB also increase, causing overpotentials to be higher than more normal, which negatively affect the battery LIB performance. A detailed explanation of overpotentials is given below.

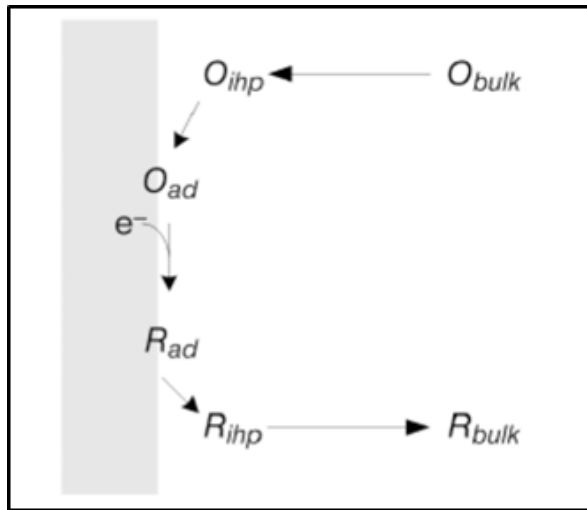


Figure 3. Transport of oxidants towards the electrode (in grey) which is subsequently adsorbed onto the surface. After the electrochemical reaction takes place, due to a concentration gradient, the reduced product is transported back to the bulk of electrolyte.

Like many liquid systems, electrolytes in batteries have concentration gradients which leads to flow of ions due to diffusion (seen in Fig. 3). Since there is constant movement of the electrolyte and an electric field is applied, there is also movement of ions (both cations and anions) due to both convection and migration, respectively.^[19, 20] These phenomena can be described in the form of equation formulated by Walther Nernst and Max-Planck, dubbed as Nernst-Planck:

$$N_i = -z_i u_i F c_i \nabla \phi + -D_i \nabla c_i + c_i \nabla v \quad (6)$$

Where N_i is the flux of a specie i

z_i is the charge of the specie i

F is the Faraday's constant

D_i is the diffusion coefficient of the specie i

c_i is the concentration of the specie i

u_i is the mobility of the specie i

where the first, second and third terms of the equation are the migration, diffusion and convection terms, respectively. As charged species are affected by electric fields, the force acting on these species due to the electric field is given by “ $-z_i F \nabla \phi$ ” ($\nabla \phi$ is the concentration gradient). As an example, $\text{LiC}_2\text{F}_6\text{NO}_4\text{S}_2$ (LiTFSi) a commonly used lithium salt, dissociates into Li^+ and $\text{C}_2\text{F}_6\text{NO}_4\text{S}_2^-$, hence the charge of the specie “ z ” can be either positive or negative. Finally, multiply the driving force (effect of electric field on the ions – anions and cations) with the mobility of the ion “ u_i ” and its concentration “ c_i ”, results in

the migration term. Since the LIBs are single salt electrolyte systems, the charges of the anion and cation are balanced and result in electroneutrality. By applying Faraday's law to the Nernst-Planck Equation and considering electroneutrality for lithium ion batteries, we simply the equation to a migration term and a diffusion term.^[19, 20]

The Faraday's equation is given by:

$$i = F \sum_i z_i N_i \quad (7)$$

The migration, after substituting the Faraday's law essential reduces to the Ohm's law:

$$-F^2 \nabla \phi \sum_i z_i^2 \mu_i c_i = -\kappa \nabla \phi \quad (8)$$

where κ is the conductivity and

ϕ is the potential gradient.

As we discuss about the effect of separators and solid electrolytes, we must better understand how the cell voltage changes for a uniform current density. To understand the voltage change, we must consider the various resistances that arise from migration, and diffusion. A separator is essentially an ionic resistor and an electronic insulator, and we must work towards reducing the ionic resistance due to migration and diffusion of ions. The resistance of a separator or solid electrolyte contributes to the so-called "overpotential" of the battery. The overpotential in electrochemistry terms, is the voltage difference between thermodynamically calculated reduction potential and the reduction potential which is observed experimentally. The overpotential of galvanic cell can be described as follows: ^[17, 19, 20]

$$V_{cell} = U_{cell} - |\eta_{ohmic}| - |\eta_{ct}| - |\eta_{conc}| \quad (9)$$

Where U_{cell} is the equilibrium cell potential

η_{ohmic} is the overpotential because of Ohmic participation

η_{act} is the overpotential due surface redox kinetics of the electrodes

η_{conc} is the overpotential due to concentration effects along the separator

Finally, how efficiently a LIB functions is denoted by its Coulombic efficiency (CE), which is the ratio of the discharge capacity by its charge capacity. A low CE leads to a low cycle life (how many times it can charge and discharge till the capacity of the LIB reaches below 80% of its actual capacity) and can be indicative of various unwanted phenomena such as lithium dendrite growth. A high CE of over 100% is also considered undesirable since it symptomatic of side reactions which could have adverse effects on LIB performance. An ideal CE should closely approach 100% after a few initial “formation” cycles.

2.1.2 Active Materials – Cathodes and Anodes

Cathodes and anodes are, as discussed earlier, host materials for Li-ions.^[14, 21] These Li-ions can be reversibly inserted and removed from the host matrix. Cathodes can be broadly classified into two major types based on their storage method: intercalation and conversion. In intercalation type cathodes, which are commonly layered, olivine or spinel transition metal oxides, Li-ions are stored between the layers of the host structure or in unoccupied octahedral or tetrahedral sites in the structure.^[17, 21, 22] Over the last few

decades, LCO has been one of the most widely used layered cathode material, especially in mobile electronic applications. LCO that was discovered by John B. Goodenough and was adopted in LIBs due to its high theoretical capacity (274 mAh g⁻¹), good cycling performance and high volumetric capacity.^[15, 23] Though LCO has been widely used for consumer electronics, the increase in Co prices, the limited amount of Co in the Earth's crust, the issues with Co supply chains and human rights issues associated with Co mining has motivated research into various cheaper layered transition metal cathodes. In addition to significant socioeconomic issues associated with LCO, scientifically LCO suffers from relatively poor thermal stability, reduced LIB calendar life, and high capacity fade at high rates, which similarly makes LCO less attractive for EV applications.^[24] Various similar transition metal oxide cathode materials have been explored with cobalt (Co) being substituted with other more abundant and less expensive transition metals, such as Ni. Higher Ni content in the layered structure has proven to prevent structural degradation of the layered structure and allows for higher Li⁺ extraction.^[25, 26] The addition of Mn, Al and other metals was explored to enhance their stability at higher voltages and higher Li⁺ de-intercalation capacities. Cathode materials, such as lithium nickel manganese cobalt oxide (NCM) and lithium nickel cobalt aluminum oxide (NCA) have become widely used in electric vehicle (EV) applications.^[27] NMC is a layered oxide cathode which is derived from lithium manganese oxide whereas NCA is a derivative of lithium nickel oxide. Both cathodes are intercalation-type and are being used for battery systems with specific energy >200 kWh kg⁻¹. Though NCA has high usable capacity and are cheaper than LCO, NCA suffers from poor thermal stability with electrolytes at around or slightly above 50°C, where

the cathode electrolyte interphase (CEI) tends to break down and leads to the capacity fade.^[28]

Though NCM and NCA drastically reduce the need of Co, NCM and NCA are still expensive cathode materials which increase the cost of the EV battery pack, and for this reason there is a growing interest for polyanion cathodes such as lithium iron phosphate LFP (which typically have an olivine structure). Phosphorous, lithium, iron (Fe) occupy the octahedral sites to form a robust 3D framework/structure that has negligible structural distortion during lithiation and delithiation.^[29] Although LFP have very high thermal stability and power density, they suffer from poor ionic and electronic conductivity and low energy density for high performance LIBs.^[30]

Other cathode materials that have grown a lot of interest are conversion-type electrodes which upon lithiation convert into a new product with a new chemical structure and new chemical bonds. As we are reaching capacity limits of layered oxide and polyanion cathodes, conversion cathodes have been interesting alternatives because of their high energy densities.^[31] Iron fluorides, copper fluoride and lithium sulfide are a few examples of widely researched conversion type electrodes.^[32, 33]

Anodes, just like cathodes, can also be classified into intercalation and conversion-type materials. Decades ago, anode materials were considered necessary since lithium dendrites grow while using a lithium metal as an anode. Though Li-metal anode technology has matured over past several decades, the Li-metal technology is still not feasible for ubiquitous use due to its safety issues and expensive cost. Initial commercial LIBs adopted the use of amorphous carbon anodes but the successful large-scale production of high-

quality and high-stability crystalline graphite from coke has helped LIB shift toward graphite anodes. Due to relatively high theoretical and usable capacities, excellent stability, low cost and low de-/lithiation potential, graphite anodes have been the “to go” intercalation-based anodes over the past 30 years. ^[14, 31, 34] Essentially, Li ions are reversibly inserted between graphene layers where 6 carbon atoms are required to store 1 Li ion (as in LiC_6). Though graphite anodes are a great anode choice, we are slowly reaching the capacity limits of graphite anodes in the pursuit for high energy density batteries for EVs and electric vertical take-off and landing aircrafts (eVTOLs). As a result, conversion type electrodes, especially silicon have garnered lots of interest over the past few years. Silicon is conversion type anode that stores lithium ions through “alloying”, and as result, expand exponential (~300% of actual size).^[14, 35, 36] This expansion of the anode material causes a variety of issues such as SEI cracking, lithium inventory loss, and anode particle cracking leading to poor cycle life.^[35-37] As a result, porous silicon-carbon and other silicon-based composites, especially nanocomposites, are commonly made to minimize volume changes to hinder battery performance issues that entail with particle expansion^[11, 38]. As extreme fast charging for EVs has become an aspect for economic reasons, developing anode materials capable for fast charging has also become important. Silicon-carbon nanocomposites and graphite SEI’s have been modified with electrolyte additives to reduce charge transfer resistance on the anode surface and enable fast charging.^[39, 40]

2.1.3 *Electrolytes*

Electrolyte is a medium between the anode and cathode which enable Li^+ ion transport. Electrolytes can be (1) solid, (2) liquid or (3) a combination of both. As

mentioned earlier, electrolytes should have either a wide electrochemical stability window or be able to form highly passivating SEI and CEI to ensure safe and long life of LIBs. Presently, most LIBs adopt the use of organic solvents in the electrolyte. Ideally a solvent for an electrolyte should meet the following requirements: (1) good solvation with lithium ions, (2) wide electrochemical stability window, (3) low viscosity and high mobility to allow fast ion movement and thus high power/ high rate performance, (4) chemical inertness to various battery components, (5) ability to form highly ionically conductive SEIs and CEIs, (6) relatively low cost, (7) relatively low density (low weight), and (8) ability to accommodate (rather significant) volume changes in active materials during battery operation.^[41-43] Presently, most LIBs use a combination organic solvents (mostly carbonates, such as ethylene carbonate (EC), propylene carbonate (PC), vinylene carbonate (VC), dimethyl carbonate (DMC), ethyl methyl carbonate (EMC), diethyl carbonate (DEC), fluoroethylene carbonate (FEC), etc.) to meet the desired requirements for electrolytes. Cyclic carbonates, such EC, VC, FEC and PC ensure solvation with lithium ions and formation of stable SEI, whereas linear carbonates such as DMC, EMC or DEC ensure lower viscosity. Lithium salts are essential for the electrolytes to conduct ions, and just like solvents, lithium salts have to meet the following requirements: (1) chemical inertness with various solvents under various potentials, (2) ability to easily dissociate into anionic and cationic form, (3) ability to form highly inorganic conductive SEI and CEI, (4) sufficiently high thermal stability and safety, and (5) reasonably low cost.^[41-43] The salt and solvents play a quintessential role in SEI formation and ideally, we expect the SEI to be robust, high conductive and stable for long cycle lives. As the requirement for batteries to charge quicker has increased over the past few years and with the introduction of the new

anode materials, more electrolyte additives have become necessary to build a robust SEI for fast charge and high-capacity anodes. FEC and VC have proven to be particularly effective “additive” solvents that decompose at lower potentials to form a robust SEI, that has improved graphite and Si anode cycling lives.^[44]

2.2 Inactive LIB Components

2.2.1 Separators

Conventional separators are made from thermoplastic polyolefins such as polyethylene (PE) and polypropylene (PP), and they can be produced large scale, but tend to suffer from low porosity, poor thermal stability (shrinking at elevated temperatures), and high tortuosity, which may cause premature failures of cells having high energy density. As discussed earlier, there is a desire to have a separator that minimizes the overpotentials in the first place through a facile conduction of Li^+ , and that is aided with additional capabilities (i.e., being thermally stable, and able to prevent shrinkage at high temperatures, etc.) to improve safety.

Furthermore, a thin, porous, and ionically conductive separator is required for the next-generation LIBs to garner the benefits of high-energy dense electrodes. Polymer-nanoparticle composites have been of interest for the past two decades to offer improved mechanical, thermal and structural properties of the separators.^[45, 46] Yet, shortcomings, such as poor cycle life, large hysteresis, and complicated processing methods, still remain, which call for further innovation in their chemistry and engineering aspects.

2.2.2 Binders

Binders are polymeric materials which form matrices with active material and conductive materials. Preferably, binders should be electrochemically stable, maintain electrode integrity, suppress large volume changes, improve energy density, allow for low tortuosity, and low resistance contributions and additionally should swell minimally when soaked in the electrolyte.^[47, 48] Binders should have good adhesion between the current collector, the active materials and the carbon additives. Although binders play a vital role in maintaining structural integrity of the electrodes, they are still inactive components of the electrode and hence, the mass fraction of binders in the electrode should be minimized to achieve maximum energy density. Polyvinylidene fluoride (PVDF) is the most commonly used binder for cathodes, since it has high thermal stability and is stable between a wide electrochemical potential window.^[36, 49] In addition to its favorable properties for LIB performance, PVDF is soluble in N-Methylpyrrolidone (NMP), which is solvent used to cast cathodes on aluminum current collectors. Though NMP is a very toxic chemical, it is used to make cathode slurries since water/other solvents oxidize the cathode surface hinder optimal performance.

Whereas anodes commonly use Styrene-Butadiene Rubber (SBR) as binder with Carboxymethyl Cellulose (CMC) as thickening agent when slurries are made using water as solvent. But with the introduction of silicon anodes, current SBR based binders are often insufficient to prevent/hinder particle expansion and as result, new binders have researched such as lithiated or sodiated polyacrylic acid (PAA) and PAA-based or PAA-comprising copolymers, which have shown promising performance.^[50, 51]

2.2.3 *Current Collectors*

Current collectors are the support/substrate for the composite matrix of active materials, conductive materials, and polymer binders. They also provide an electric contact between the battery's external circuits with the internal active/in-active materials undergoing through redox reactions. The most commonly used current collectors are aluminum (Al) foils and copper (Cu) foils for the cathode and anode respectively.^[52, 53] Since cathode are de-lithiated at voltage greater than 3.5V (typically 4.2-4.5V), Al current collectors can be passivated and remain stable (not oxidize and dissolve) in these high operating voltages.^[54] Though nickel (Ni) or titanium (Ti) are another candidates for cathode current collectors, AL is cheaper, lighter electrically more conductive and easily processable.

Copper is the most commonly used anode current collector because of its stability at lower voltage ($\sim 0V$ vs. Li/Li^+). Cu generally forms an oxidized layer, copper oxide, in the presence of air and moisture and copper oxide acts as a passivating layer to prevent further oxidation.^[52, 54] Just like, Al, Cu is easily processable, highly electrically conductive and cheaper than most current collector alternatives. Though both Cu and Al form passivating oxidized layers, they are generally welded to nickel tabs to ensure long term performance of the tabs isn't compromised.^[52-54]

2.2.4 *Carbon Additives*

Generally, the binder and the cathode materials intrinsically have low electrical conductivities. As result, to move electrons towards the current collector during the redox reactions (during intercalation and de-intercalation), carbon additives are added to the

composite electrode matrix to build a network for electrons to move towards the current collector. Some of the most commonly used carbon additives are: carbon black, carbon nanotubes, or carbon nanorods.^[55, 56] Carbon additives play a crucial role in the electrochemical process, since the efficiency of the carbon additive and how well they are dispersed play a crucial role in charging rate, cycle life and energy density. Since carbon additives are inactive materials, their weight ratio in the electrode must be minimized to ensure the energy density of the LIB isn't compromised. Carbon black is the most commonly used carbon additive because of its low cost, facile synthesis and high surface area.^[55, 56]

2.3 Solid Electrolytes for LIBs

From the 1980s, inorganic solid-state electrolytes have garnered attention because of their wide variety of applications in capacitors, fuel cells, sensors, and batteries. Inorganic solid-state batteries offer high mechanical strength and ionic conductivities making it useful for a wide variety of applications.^[57] For the past two decades, most of the research in solid-state electrolytes has been on improving ionic conductivities of electrolytes by doping, electrode wetting or surface contact, flexibility and deposition of solid-state electrolytes onto electrodes.^[58] The Li-ion transfer of a solid electrolyte is influenced by carrier type, diffusion type and diffusion pathway.^[59] The carrier types will be determined by the point defects such as vacancy or interstitial defects. As with any ceramic materials, the inorganic solid electrolytes are composed of grain boundaries and Li⁺ ion conduction along grain boundaries is relative low since the composition and the interface along the grains is different to that of the bulk.^[57] The figure below shows the various Li⁺ ion

conduction mechanism along the grain. Transfer of ions through the lattice structure of the solid-state electrolyte is very important and determines the efficiency of any electrolyte.^[60]

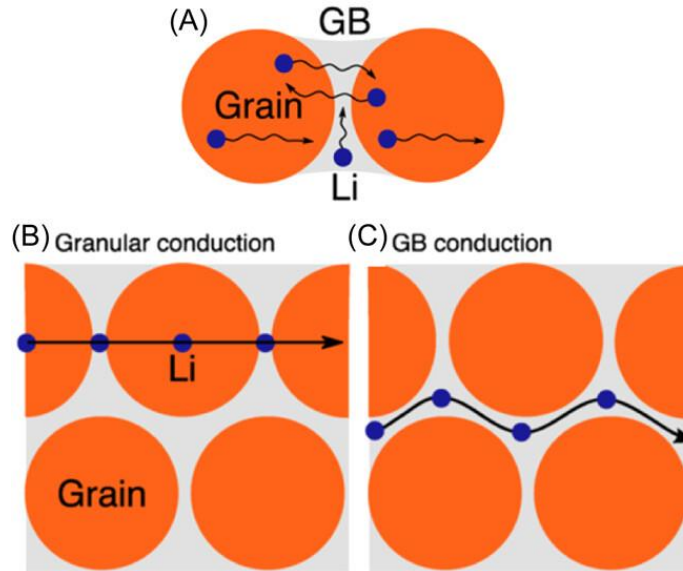


Figure 4. Movement of Li-ions along, across and through the grain boundaries. Generally, Li-ion conduction through the grains is very low.^[60]

The most widely used and focused on inorganic solid electrolytes are Lithium Argodyte, Perovskite type, Anti-perovskite type, Garnet type and LISCON type.^[1, 7, 57, 58] In general, inorganic solid electrolytes provide high chemical and electrochemical stability, high mechanical strength and high oxidation voltage, but are not very flexible or deformable to accommodate volume changes, commonly heavy (suffer from high density) and cannot be made economically at large scale with sufficient quality control.^[61, 62]

Perovskite solid electrolytes have a structure similar to that of CaTiO_3 (ABX_3), where A atoms are at the corner of the unit cell, B atoms at the center of the crystal lattice and X atoms are located at the face centers.^[63] SSE with this structure are generally in the form $\text{Li}_{3x}\text{La}_{2/3-x}\text{TiO}_3$ and offer an ionic conductivity of around $10^{-3} \text{ S cm}^{-1}$.^[64] Y. Li et al

show that conductivity in perovskite type solid state electrolytes is limited by Ti^{4+} but it has been seen that adding lithium to the basic lithium perovskite structure can improve ionic conductivities.^[65] Introduction of lithium modifies the concentration of both lithium and vacancies, and their interaction with vacancy concentration can significantly influence ionic conductivity. Li^+ ions can diffuse by jumping in the AB plane to an adjacent vacancy through a bottleneck made of oxygen forming the corners of the octahedra at room temperature.^[66] This bottleneck can be increased in size alkali metals at the A site. Anti-perovskite solid state electrolytes on the other hand, have a structure just opposite to that of perovskite electrolytes.^[67] The key difference is that the positions of the cation and anion constituents are reversed in the unit cell structure.

In contrast to perovskite, anti-perovskite compounds consist of two types of anions coordinated with one type of cation. Li_3OCl , Li_3OBR , Na_3OCl and Li_2OHCl are few examples of anti-perovskite solid electrolytes.^[1, 59] These electrolytes tend to have low conductivities of around $10^{-6} \text{ S cm}^{-1}$ and very sensitive to moisture and air. Research is hence going on to improve usability of these types of solid-state electrolytes.

Over the past few years garnet type electrolytes have come to light because of their high conductivity comparable to those of aqueous electrolytes ranging around 10^{-3} to $10^{-4} \text{ S cm}^{-1}$. They have a wide electrochemical stability window, and have relatively low interfacial resistance based on the way electrode-electrolyte interfaces are modified. Lithium metal is relatively stable with garnet type's electrolytes. LLZO, LLCZN and LLTO are few examples of high conducting garnet electrolytes used commonly in research.^[68] Garnet electrolytes have a general formula of $\text{A}_3\text{B}_2\text{Si}_3\text{O}_{12}$ in which A and B cations have an eight-fold and six-fold rotations respectively.^[1] The garnet electrolytes

commonly used are $\text{Li}_6\text{ALaM}_2\text{O}_{12}$ where M is Nb or Ta and A is Ca, Sr or Ba, and cubic form of $\text{Li}_7\text{La}_3\text{Zr}_2\text{O}_{12}$.^[69] Garnet electrolytes are prepared through a solid state reaction, sol-gel process or even through ball milling. In both methods (solid-state and sol-gel), reactants or precursors are mixed together and dissolved in de-ionized water and 10% excess LiNO_3 to compensate for the volatile Li during high temperature treatment. The solution then heated to 120 °C for almost half a day to procedure a gel or powder. This product is then calcined at 400 °C and 800 °C for few hours each time. These powders are then pressed into a pellet and again sintered at around 1000 °C to produce a ceramic solid-state electrolyte.

Sodium super ionic CONductor (NASICON), is a solid state electrolyte with a general formula $\text{Na}_{1+x+4y}\text{Zr}_{2-y}\text{Si}_x\text{P}_{3-x}\text{O}_{12}$ (where x ranges between 0 and 3 and y lies between 0 and 1).^[70] They are known for their high conductivities comparable to those of liquid electrolytes. NASICON electrolytes have a rhombohedral or monoclinic structure, consisting of covalent chains of ZrO_2 octahedra and PO_4/SiO_4 tetrahedra at the corners.^[70] The sodium ions move through the interstitial 3 sites of the structure and hence through the bulk electrolyte. NASICON electrolytes are generally produced through solid state reactions, where all the reactants/precursors are stoichiometrically mixed together and then ball milled for several hours. The resultant powders are then calcinated at around 1000°C for several hours and is again powdered by ball milling.^[71] This powder, the solid electrolyte, is made into a pellet and sintered to produce a ceramic style solid electrolyte.^[71] NASICON electrolytes aren't most widely used solid electrolytes since they are mainly used with sodium-sulfur batteries, and are not compatible with lithium type electrodes.

Also, sodium-based batteries are very expensive to produce because of rigorous refinement processes for sodium.

Another class of high conductivity solid electrolytes are glassy-ceramic type of electrolytes which are also known as sulfide-based electrolytes. LISCON, $\text{Li}_2\text{S-SiS}_2$, $\text{Li}_{10}\text{GP}_2\text{S}_{12}$ and $\text{Li}_2\text{S-P}_2\text{S}_5$ are few examples of sulfide-based solid electrolytes however with high conductivity, they have poor interfacial properties and very sensitive to air and water.^[72] The addition of metal-oxides and the presence of oxygen atoms can help reduce the interfacial resistance between the cathode and electrolyte. For example, $\text{Li}_2\text{S} \cdot \text{P}_2\text{S}_5$ glassy powders were prepared by continuous mechanical milling (for around 20 h) for the mixture of reagent-grade Li_2S and P_2S_5 crystals using a planetary ball mill apparatus.^[73] In order to obtain glass-ceramics, the obtained glassy powders were heated up to 230 °C and kept at the temperature for 4 h, and slowly cooled down to room temperature in an argon atmosphere.^[73]

The organic polymer widely used by researchers are polymer type solid electrolytes. Their conductivities are based upon the phase - amorphous or crystalline. Amorphous or crystalline is based on the temperature of the polymer.^[74, 75] PolyEthyleneOxide (PEO) a widely used polymer electrolyte, has enhanced conductivities at amorphous state when the polymer is heated to around 60 °C.^[74, 75] As the polymer chains transform from crystalline to amorphous, the chain relaxes and allows the transfer of lithium ions along the chain. At the amorphous state, the conductivities range around $10^{-4} \text{ S cm}^{-1}$ but in the crystalline state the conductivity is drastically reduced at the order of $10^{-6} \text{ S cm}^{-1}$.^[76] PEO, or any other composite polymers, are generally heated to 60 °C, where they tend to melt and form a thin

film with an amorphous structure. But these thin film polymers aren't very stable at high temperature and have a low oxidation voltage.

2.4 Methods and Characterization

Experimental material science work requires material characterization methods and tools. Though it can be broadly explained, in this section we explain the material characterization, method development and electrochemical characterization corresponding/relating to the work in this thesis.

2.4.1 Coin Cell Preparation

Like most coin cell preparation present in literature, this work adopts a very similar method to CR2032 coin cell fabrication. As to coin cells in general, the major components are: bottom cap, spacer, spring and top cap.

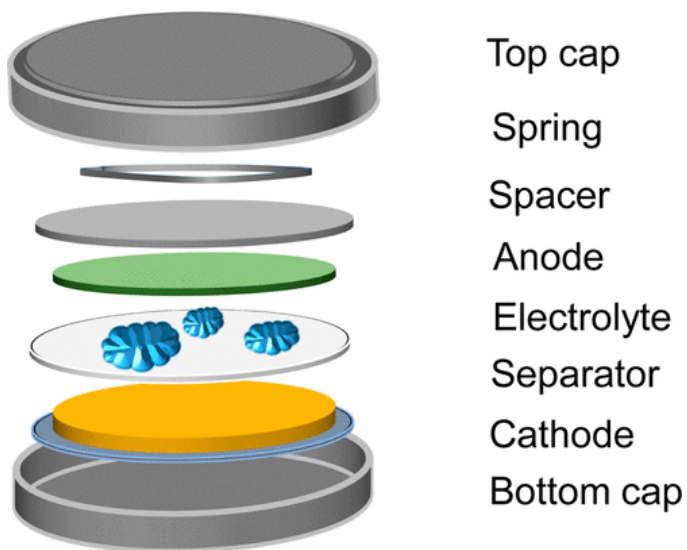


Figure 5. Coin cell fabrication schematic and systematic assembly.^[77]

As shown in the above figure, using the bottom cap as the base, a LE or SSE coin cell is assembled in the following manner: cathode, separator/SSE separator (for liquid coin cell cells, 75ul of electrolyte is added when the separator is added), anode, spacer, spring and finally, the top cap. This stack is cold-pressed using a coin cell crimper (die set for crimping coin cells) at 0.7 ton. All parts are ultrasonicated in an acetone bath to ensure there is contaminants during the assembly process in the glovebox. The coin cell is the commonly used format for both LE and SSE cells in this work.

2.4.2 *Scanning Electron Microscopy (SEM)*

SEMs are a powerful tool which is used in most experimental sciences. They are powerful tools since they can image particles, molecules or specimens up to 1-20 nm. SEMs fundamentally work on the electron interactions with the target particle/specimen surface. These microscopes use an electron source to produce a beam of highly energetic electrons which is directed towards specimen surface using a set of condenser lenses. When a sample/specimen surface is exposed to a highly energetic electron beam, there are multiple electron interactions/signals that arise: secondary electrons, backscattered electrons, and cathodoluminescence. Secondary electrons are low energy electrons which escape from the few nanometers depth of the specimen surface, and hence secondary electrons are used to study the topography of the specimen. Backscattered electrons are signal/electrons which are reflected back to the SEM detector and back scattered electron images generally show the distribution of various materials of varying atomic numbers. SEM was employed in this work to study the microstructure of the solid electrolyte, study the infiltration process of electrolyte into electrodes, and study the ND polymer composite.

2.4.3 *Transmission Electron Microscope (TEM)*

TEMs are microscopes where intense electron beams are transmitted through a thin material/sample. TEMs are powerful analytical tools to investigate (not limited to) the material crystal structure, defects in crystal structures, and/or thin coatings applied to nanomaterials. The materials have to be made thin or should be small enough to be placed in a TEM grid, as to transmit electrons through the samples. Large and bulky prevent electron transmission and hinders the detectors from developing an image. We use TEM in this work to study NDs dispersion in polymer fibers and to study electrolyte wetting/coating on active materials.

2.4.4 *X-Ray Diffraction (XRD)*

XRD is a bulk material characterization tool that is frequently used to study crystalline materials that have a specific crystal structure. XRDs produce high energy intensity electron which is subsequently diffracted or scatter by the atoms/molecules present in the material. The scattering of x-rays could be either destructive (x-rays cancel off each other) or constructive (in specific directions x-ray they add to each other) in nature, and the constructive x-rays are determined by Bragg's law (mentioned in the below equation):

$$n\lambda = 2d\sin\theta \quad (10)$$

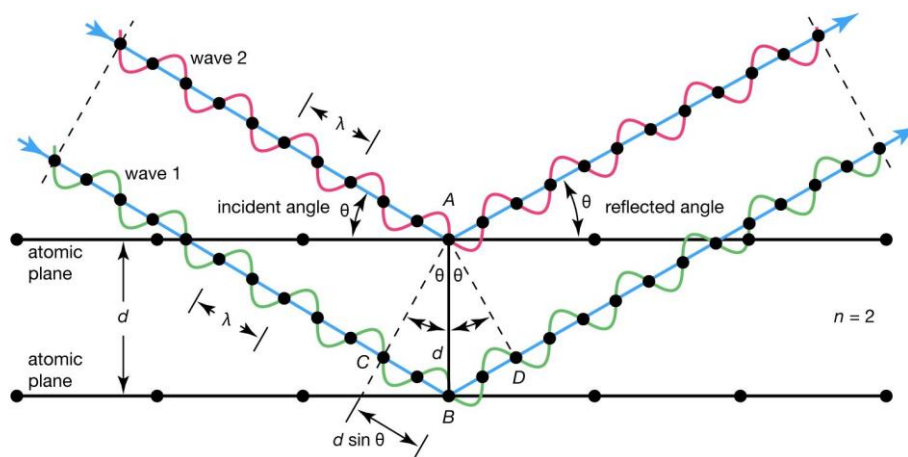


Figure 6. Constructive interferences of x-rays demonstrated through Bragg's law.^[78]

The above figure is an illustration of how we could relate the scattered x-ray angle with the interplanar distance within the crystal structure. XRD was in this work to study and identify the crystal structure of the SSE fabricated, and study how the crystal structure changes with respect to size and morphology with halide anion doping.

2.4.5 X-Ray Photoelectron Spectroscopy (XPS)

XPS is a surface sensitive tool which belongs to the photoemission spectroscopy family. The surface of a sample is irradiated due to photoelectric effect when bombarded with high energy electron beams and the kinetic energy of the electrons are measured. A minimum amount of energy has to be spent to remove an electron from its shell which is called its binding energy. Electrons from specific shells of each element will have unique binding energies, and this could be used to study the chemical composition of the material, chemical state and state of bonding of each material. The binding energy ($E_{binding}$) and the kinetic energy ($E_{kinetic}$) can be related by the following equation:

$$E_{binding\ energy} = E_{photon} - (E_{kinetic} + \Phi) \quad (11)$$

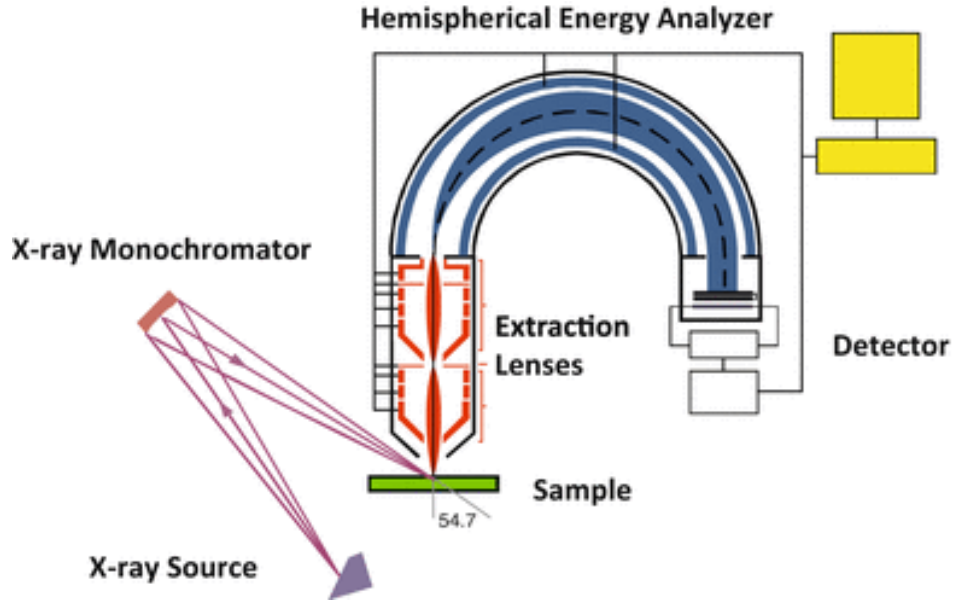


Figure 7. Schematic diagram of an XPS. A hemispherical analyzer is used to detect the irradiated electrons.^[79]

XPS is used in this work to study the chemical composition of the various precursors in the SSE and confirm the chemical composition of these precursors. In addition to fundamentally analyzing the precursors, we study how the chemical structure/bonding of the SSE vary after electrochemical testing.

2.4.6 Differential Scanning Calorimetry (DSC)

DSC is a characterization tool that measures the heat capacity of a material with varying temperature. A known amount of material (in mass) is heated or cooled and the change in heat capacity is measure in the form of heat flow (W/kg). DSC can be done at either constant volume or constant pressure and is insulated from the outside environment

to ensure that outside heat flow or temperature changes doesn't affect measurements of the instrument.

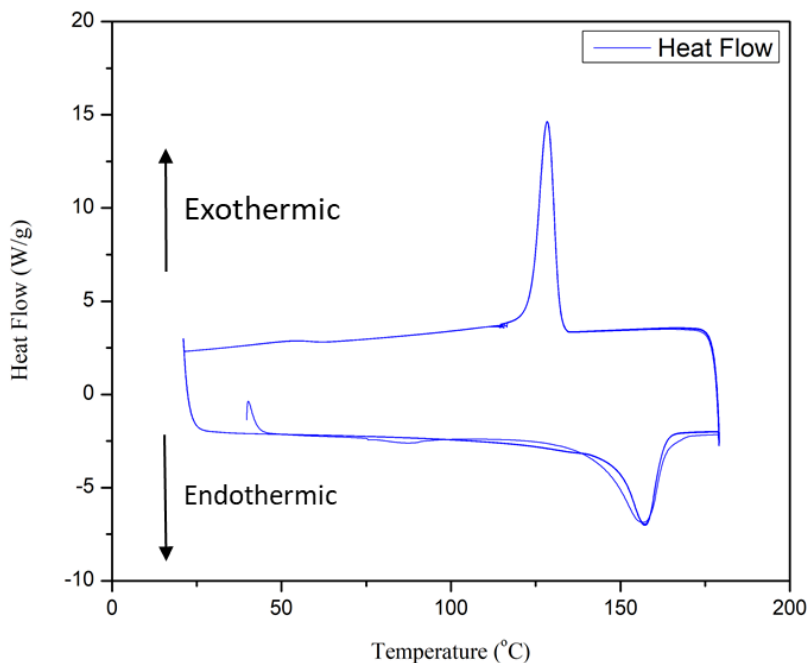


Figure 8. Example heat flow of a polymer during DSC measurements.

As seen in the above figure, all the heat flows in the positive y-direction are exothermic in nature such as chemical reactions (although there are chemical reactions which are endothermic) and all negative heat flows are endothermic in nature such as phase transformations. DSC is used in this work to study the phase transition of the electrolyte, reactions with various active materials, and melting point of the solid electrolyte. DSC is also used to study the percentage of crystallinity of the polymer when embedded with NDs.

2.4.7 Electrochemical Characterization

This work uses electrochemical characterization/tools to study and evaluate the performance of SSE and separators to varying electrochemical inputs. Electrochemical

characterizations use measurement of current, voltage or charge to study concentration of charged species. There are various techniques which fall under the umbrella of electrochemical characterization such as cyclic voltammetry or electrochemical impedance spectroscopy.

2.4.7.1 Electrochemical Impedance Spectroscopy (EIS)

EIS is widely used electrochemical characterization methodology employed to systematically study the kinetic and mechanistic properties of electrochemical systems, materials and reactions. EIS is usually measured by applying an AC potential to an electrochemical cell and then measuring the current through the cell. Electrochemical systems are a lot more complex than ideal circuits, hence EIS is done at a very small excitation signal, so we can receive a pseudo-linear response from the cell, material or electrode under investigation to make interpretation easier.^[80] In a pseudo-linear system, the current response to a sinusoidal potential, will be a sinusoidal with a phase shift. Let's consider a voltage has been applied to an electrochemical, the sinusoidal potential applied can be expressed by the following equation:

$$V_t = V_o \sin(\omega t) \quad (12)$$

The following current response with a phase shift (Φ) can be represented by the following equation:

$$I_t = I_o \sin(\omega t + \Phi) \quad (13)$$

Now corresponding to Ohm's law, the impedance can be expressed by the following equation:

$$Z = \frac{V_t}{I_t} = \frac{V_o \sin(\omega t)}{I_o \sin(\omega t + \Phi)} = Z_o \frac{\sin(\omega t)}{\sin(\omega t + \Phi)} \quad (14)$$

Applying Euler's law/formula to equation 14, the impedance can be expressed in much mundane form:

$$Z = Z_o(\cos(\Phi) + i\sin(\Phi)) \quad (15)$$

When Zreal ($Z_o \cos(\Phi)$) is plotted against Zimag ($Z_i \sin(\Phi)$), we plot a semicircle also called a Nyquist plot. ^[80] This Nyquist plot can be represented in the form of an equivalent circuit which is very complex for lithium ion batteries. The equivalent circuits for different cell chemistries, or cell formats could vary due to varying interfaces, reactions and resistances. Randles circuit is a well-known circuit used to model a simple two electrode (non-coated) system in an electrolyte bath. The Randles circuit models, the electrolyte resistance, and the capacitance of the double layer and the polarization of the electrode.

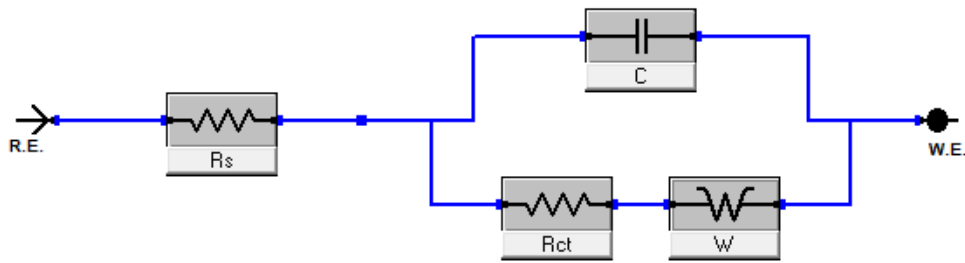


Figure 9. Randles equivalent circuit representation.

The corresponding Nyquist plot for Randles equivalent circuit would be represented by the following graph:

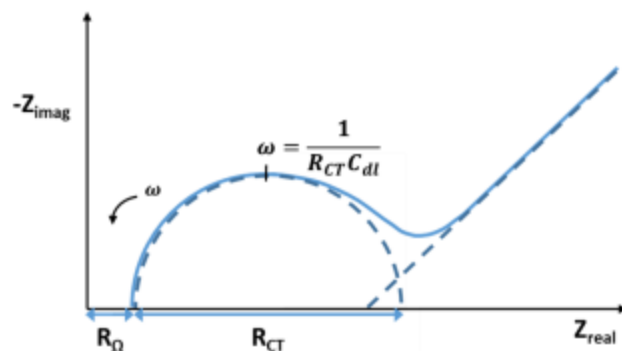


Figure 10. Nyquist plot of a Randles equivalent circuit with a diffusion element.

EIS is used in this work to study the resistance of SSEs, separators, analyze the SEI resistances formed by the electrolyte with various active materials, study resistance changes during cycling.

2.4.7.2 Cyclic Voltammetry (CV)

CV is electroanalytical tool to systematically investigate the redox reactions occurring at various voltages. Commonly, the potential of the electrochemical system is below its equilibrium potential, as a result in CV, the potential is ramped up to a target value and the current response is measured. Redox phenomena occurring in the electrochemical system is expressed by an increase the current as the potential is ramped up. CV is used this work to study the electrochemical stability window of the SSEs in order to understand the compatibility with various active materials.

CHAPTER 3. ANION SUBSTITUTED BOROHYDRIDE-BASED SOLID ELECTROLYTES FOR HIGH ENERGY LITHIUM ION BATTERIES.

3.1 Introduction and Background

Metal borohydrides have the general formula of $M_xB_yH_z$, where M are alkali metals such as Li, Na, Mg and K and the B_yH_z is the borohydride anions^{[81],[82]}. The Li-ions are generally held together in a network of anions, which include BH_4^- , $B_6H_6^{2-}$, $B_{10}H_{10}^{2-}$, and $B_{12}H_{12}^{2-}$ ^{[81],[83]}. $LiBH_4$ has orthorhombic structure with a point group of $Pnma$ but transforms to the hexagonal phase with a point group $P6_3mc$ at 383K^{[83],[84]}. At room temperature, $LiBH_4$ crystalizes to form a orthorhombic structure where the BH_4^- is surrounded by four Li atoms and each Li atom is surrounded by BH_4^- atoms in a tetrahedral configuration^[85] (as seen in Figure 10 [86]). This arrangement corresponds to an orthorhombic distorted wurtzite type metal substructure in which the tetrahedral BH_4^- anions point along two orthogonal directions in an ordered fashion^{[85],[87]}. In this distorted orthorhombic wurtzite structure, the anions are buckled into a layered and orderly packed slightly distorted tetrahedral position^[87]. The BH_4^- anions have a point symmetry m , a mirror plane symmetry perpendicular to the rotation axis n , and are strongly deformed with respect to bond lengths $B-H = 1.04-1.28$ Å, and bond angles $H-B-H^\circ = 85-120^\circ$ ^[85] (as seen in figure 3^[86]). This distorted wurtzite structure is transformed into a hexagonal wurtzite structure at high temperatures ($\sim 383K$) where structure contracts along the orthorhombic a-axis and expands in the orthorhombic b-c plane (hexagonal basal plane) such that a density increase occurs at the transition temperature^[85]. However in $LiBH_4$, in

the hexagonal phase (high temperature phase), the BH_4^- ions are all orientated in the C plane and as result, one of the four BH_4^- ions moves away from lithium while the other three moves towards $\text{Li}^{[85]}$.

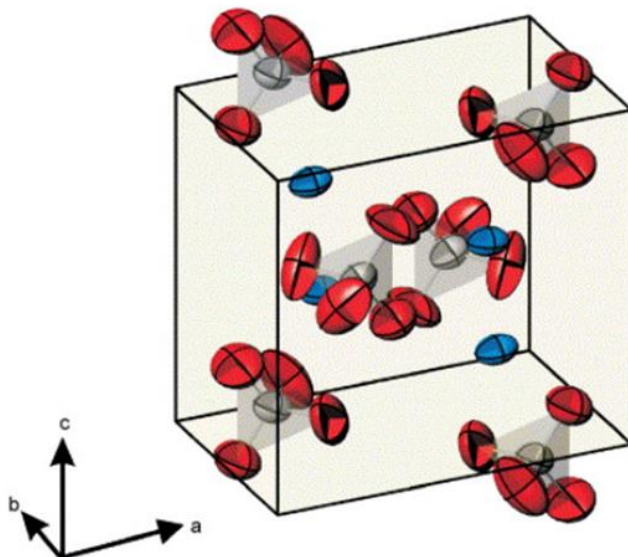


Figure 11. Low temperature phase polymorph of LiBH_4 , with lithium ions present in the tetrahedral positions with the BH_4^- anions layered to form an orthorhombic structure.^[86]

The structural change in LiBH_4 with temperature plays an essential role in Li^+ conductivity, which in turn plays a major role in ASLB performance. In the low temperature phase, the SSE shows poor Li^+ (in the order of $\sim 10^{-7}$ S/cm to 10^{-8} S/cm^{[88],[89]}) conductivity because of tightly coordinated Li^+ , but in the high temperature phase, the Li^+ tend to be loosely coordinated and the Li^+ conductivity improves by almost 3 orders of magnitude ($\sim 10^{-4}$ S/cm^{[88],[89]}). As mentioned earlier, as the BH_4^- are all orientated in the c axis direction, the Li^+ have a more direct path more movement^[89]. This high-temperature phase of LiBH_4 is essentially for high energy density solid state LIBs because of high Li^+ conductivity but isn't perfect for real world applications due to undesirably too high

operating temperatures. Fortunately, this high temperature is phase stabilized at lower temperatures by halide doping^{[87],[90],[91],[92]} and confining LiBH_4 ^{[88],[90]} crystals in nanostructures.

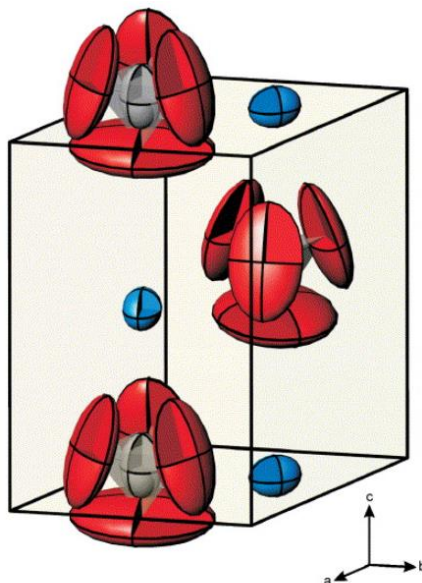


Figure 12. High temperature phase polymorph of LiBH_4 , with lithium ions distributed along the tetrahedra.

Although there is a lot of literature on halide doping of LiBH_4 , exactly how LiBH_4 's high temperature phase is stabilized at lower temperatures by dopants remains insufficiently researched. Experimentally, by doping LiBH_4 with LiCl , LiBr , and LiI , and expansion of the LiBH_4 occurs since the ionic radius of halide ions are larger than that of BH_4^- ions^[92]. Studies suggest that, with larger halide ions, the local coordination of Li^+ is altered, which results in a ionic conduction path that isn't fully 3 dimensional which is similar to that of hexagonal phase of LiBH_4 ^[92]. On the other hand, nano-confinement of LiBH_4 in mesoporous structures such MCM-41 (mesoporous silica) and meso-porous alumina have shown to confine grains to nanosizes^{[88],[93],[94]}. As a result of smaller grains, more grain

boundaries are formed and studies have shown that hopping across smaller grain boundaries lowers the activation energy for Li⁺ hopping therefor improving the Li⁺ conductivity^{[88],[93]}^[95]. Halide doped LiBH₄ is traditionally made through ball-milling^[93, 96], which is an energy-intensive process and isn't necessarily scalable for large scale production of all solid-state batteries. In addition to using ball-milling as method of synthesis of halide doped powders, very few studies have actually shed light on using this solid electrolyte for all-solid-state batteries. Table 1 summarizes studies using halide-based LiBH₄ solid electrolytes in different types of solid-state cells but mainly limited to symmetric lithium cells and lithium titanate (LTO) half cells.

Table 1. Summary of studies on halide-based and pure LiBH₄ in various cell architectures

Literature	Type of LiBH ₄ Solid Electrolyte	Cell Structure/Composition
Das, S., et al. ^[93] Unemoto, A., et al. ^[96] Lefevr, J., et al. ^[97] Choi, Y.S., et al. ^[94]	Nanoconfined LiBH ₄ mixed with silica particles to improve conductivity. These solid electrolytes were made through ball milling.	Li ₂ S//LiBH ₄ //Li* *Lithium sulphide (Li ₂ S) half cells, where lithium sulphide was mixed with solid electrolyte to make composite electrode pellet

<p>Lu, F., et al.^[95]</p>	<p>LiBH₄-LiI solid electrolyte that was subsequently into SBA-15 (mesoporous silica with interconnected pores) by melting.</p>	<p>Li₂S//LiBH₄-LiI@SBA-15//Li* *LTO//LiBH₄-LiI@SBA//Li LCO@LiNBO₃-80Li₂S-20P₂S₅//LiBH₄-LiI@SBA-15//Li *Li₂S and LTO were both mixed with solid electrolyte powder to make a composite electrode pellet</p>
<p>Sveinbjörnsson, D., et al.^[97]</p>	<p>LiBH₄-LiI solid electrolyte which was prepared by ball milling</p>	<p>LTO//LiBH₄-LiI// Li* LTO powders were mixed with solid electrolyte powder to form a composite electrode pellet.</p>
<p>Choi, Y.S., et al.^[94]</p>	<p>LiBH₄-LiCl prepared through ball milling</p>	<p>S-KB-Maxsorb@LiBH₄-LiCl//LiBH₄-LiCl//Li* *Sulfur with carbon were added to the solid electrolyte to make a composite electrode pellet</p>

Hu, L., et al. ^[98]	LiBH ₄ -LiI with g-C ₃ N ₄ which was prepared through ball milling	LTO//LiBH ₄ -LiI@g-C ₃ N ₄ // Li* S-C//LiBH ₄ -LiI@g-C ₃ N ₄ // Li* FeF ₃ // LiBH ₄ -LiI@g-C ₃ N ₄ // Li* *LTO, S-C and FeF ₃ were mixed with solid electrolyte powder to make composite electrode pellets
Unemoto, A., et al. ^[99]	LiBH ₄ was used as the solid electrolyte.	TiS ₂ //LiBH ₄ //Li* TiS ₂ was ball milled with the solid electrolyte to make composite electrode pellets.

Although there is research on using LiBH₄, including doped and nano-confined versions, in ASLBs with various intercalation and conversion type cathodes, there is a lack of proper understanding on key degradation mechanism in such cells and how active material surface and properties affect cell stability and overall performance. Also, no work has shown LiBH₄'s compatibility with graphite or silicon anodes, and Li(Ni_xCo_yMn)O₂ (NMC) cathodes, which are active materials used in mass manufacturing of LIBs for electric vehicle (EV) applications. The study of LiBH₄ with these mass manufactured electrodes is an interesting avenue of research. As Table 1 shows that most work uses ball milling to prepare halide-doped LiBH₄, it may be interesting to explore easier and more scalable fabrication techniques such as melt-infiltration to prepare halide-doped LiBH₄ and

their nano-confined versions. We would also like to understand how melt-produced electrolytes perform and eventually test them in ASLBs. Since Li dendrite growth is an important issue in Li metal batteries ^[100-102], we would like to explore the mechanical properties of halide-doped LiBH₄ electrolyte to understand their potential for Li dendrite suppression.

Metal borohydrides with larger anions have garnered more interest over the past few years. Larger anions cause poor Li coordination to improve Li⁺ conductivity^[103]. Dodecahydro-*closo*-dodecaborate Li₂B₁₂H₁₂^[104] as an example, is a borohydride solid electrolyte that has a Li⁺ conductivity of 30 mS/cm at room temperature. These *closo*-borates have been further modified through substitution to form Li₂B₁₀H₁₀, LiCB₁₁H₁₂, and LiCB₉H₁₀ with similarly high conductivity of around 150-30 mS/cm^[103]. These *closo*-borate SEs are still not well researched and a lot of the research focuses on understanding phase transition temperatures at high-temperatures just like LiBH₄ show enhanced Li-ion conductivity^{[103],[104],[81],[105]}. The synthesis of Dodecahydro-*closo*-dodecaborate Li₂B₁₂H₁₂ is done through a one-step synthesis of decaborane and trimethylamine-borane. The precursors are heated in an evacuated vessel in a nitrogen atmosphere to form trimethylamine-borane, which is used as a precursor of *closo*-borate based SEs. The trimethylamine-borane is then lithiated by mixing with LiOH in water.^[106] The resulting solution was evaporated to dryness under a stream of nitrogen to remove trimethylamine.^[106] Li₂B₁₀H₁₀, just like LiBH₄, has both a low temperature and a high temperature phase. The phase transition occurs at around ~615K, where Li₂B₁₀H₁₀ is a cubic phase at room temperature and then transforms to a distorted cubic phase upon heating.^[107] The observed

H-Li-H angles are $66.7(6)^\circ$, $91.9(7)^\circ$, $93.8(4)^\circ$, and $106.6(2)^\circ$.^[108] This arrangement seems to optimally satisfy Li^+ 's small ionic radius and short bond length to the H of $\text{B}_{12}\text{H}_{12}^{2-}$.^[108]

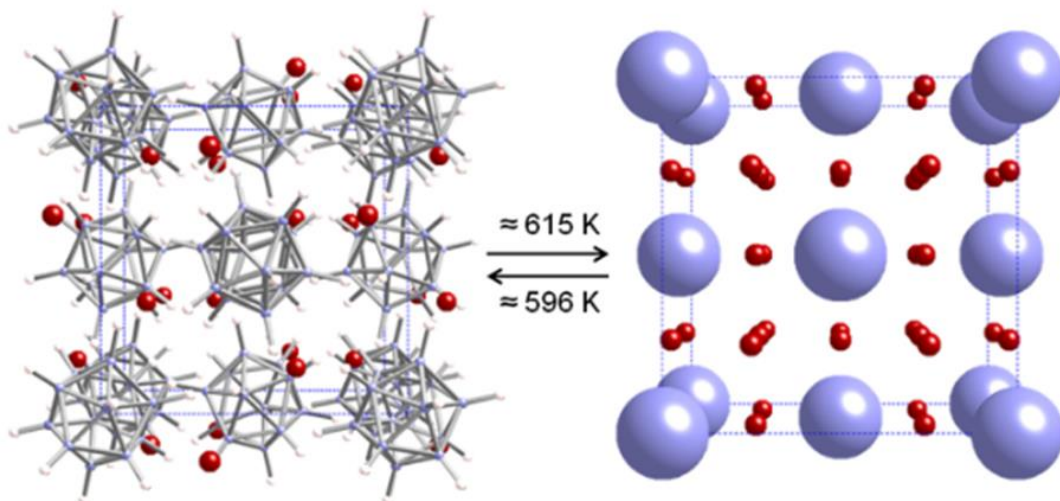


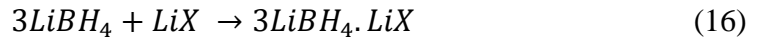
Figure 13. The left crystal structure is a representation of the low temperature phase of $\text{Li}_2\text{B}_{10}\text{H}_{10}$ which is cubic^[107]. The structure on the right is a distorted cubic structure, which suggests the Li-ions are constantly in motion on this disordered Li sublattice, implying that the high temperature $\text{Li}_2\text{B}_{12}\text{H}_{12}$ polymorph is a potential Li^+ superionic conductor^[104].

As seen, there is a lot of work done on understanding the crystal structure of $\text{Li}_2\text{B}_{12}\text{H}_{12}$ at very high temperatures and understand phase transitions. The high temperature polymorph of $\text{Li}_2\text{B}_{12}\text{H}_{12}$ is a very interesting solid electrolyte for high-energy dense all solid-state batteries, but little-to-no work has been done on trying to stabilize the high temperature polymorph at room temperature. Also, there isn't much work done understanding the electrochemical properties of these closo-borate electrolytes such electrochemical stability window, Li-diffusion/transport number and its performance with intercalation and conversion type electrodes.

3.2 Experimental Methods of Anion Substituted Borohydride Based Solid Electrolytes

3.2.1 Synthesis of Anion Substituted Borohydride SSEs

All SSEs were synthesized in an argon filled glovebox ($H_2O < 1\text{ppm}$) and all precursor powders were dried in a muffle furnace for 24 hours before synthesis. $LiBH_4$ (obtained from Alfa Aesar 95% purity), LiF , $LiCl$, $LiBr$ and LiI (all obtained from Alfa Aesar 99% purity) were dried to ensure all moisture is evaporated. For anion substituted SSEs, which can also be referred to as halide doped SSEs, all SSEs were synthesized using 3 moles of $LiBH_4$ and 1 mole of LiX salt.



The solid-state reaction between lithium borohydride and the lithium salt to synthesize the halide doped SSE was done at 340°C using a muffle furnace. 1 g of total precursor powder (following the mole ratio), was mixed using a mortar and pestle and the mixed powder was placed in an in-house made graphite crucible. The graphite crucible was covered with a graphite cap and placed in a room temperature muffle furnace. The muffle furnace is heated to 340°C at $10^\circ\text{C}/\text{min}$ and held at 340°C for 15 min to ensure the uniform eutectic mixture of $LiBH_4$ and the LiX salt. The molten SSE was then poured on to a graphite template which is made into a fine powder using a mortar pestle.

The ball-milled SSEs were synthesized by adding 2 g of precursor powder (following the mole ratio) to a 100 ml zirconia ball mill which uses 12 mm spherical zirconia milling media. A zirconia ball mill and milling media were used to ensure there

would be no reactions with the SSEs. The powder to ball weight ratio was 1/200 or 2g of powder to ten 12 mm (10 12 mm milling media is around 400g) spherical zirconia milling media. The ball-milled was placed in a vacuum to ensure the lid is tightly sealed to the ball-mill jar. The precursor powders were ball-milled for 24hrs at 600 rpm.

3.2.2 SSE Characterization

XRD (Rigaku Miniflex Powder XRD) was used to study the crystal structure and changes in size of crystals with halide doping. As the solid electrolytes are sensitive to air and moisture, an air-sensitive sample holder was used along with zero background holders. All samples were prepared and loaded into the XRD holders (air sensitive or zero-background) in an argon filled glovebox. For zero background holders, Kapton tape was placed over the zero-background holder to ensure that SSEs aren't exposed to air and moisture. XRD measurements were done between a 2θ (2theta) of 15° to 70° at a speed of $2^\circ/\text{min}$ using a Cu $K\alpha$ x-ray source with a voltage of 45 kV and current of 40 μA . For high-temperature in-situ measurements (with Malvern Panalytical Empyrean), a vacuum chamber with the heating function was used. Spectra were collected at 26, 40, 60, 80, and 110°C with a heating rate of 1°C min^{-1} and 2θ range $20^\circ - 70^\circ$.

The SSE powders were pressed into pellet at room temperature in an inert glovebox and placed onto a carbon tape SEM stub. An accelerating voltage of 5 kV was used to take SEM (Hitachi SU8230) images of the powders. Focused-ion beam SEM (Helios 5CX) were used to take cross-section image of the electrolyte pellet. All SEM samples were loaded into the SEM analysis chamber using a nitrogen glovebag to ensure that the samples are

protected from air and moisture. The glovebag was purged with nitrogen 3 times before loading the samples into the SEM transfer chamber.

XPS (Thermo NEXSA G2 XPS) was used to study the chemical states of the elements in LiBH_4 , LiCl and in SSEs. All powders were dried in a muffle furnace at 100°C for 12 hours before loading the powders onto a XPS air sensitive sample holder. DSC samples were prepared inside an argon filled glovebox (H_2O ppm < 1 ppm), and powders were loaded into an aluminium pan. The heating rate was $10^\circ\text{C}/\text{min}$ to ensure that measurements are sufficiently sensitive to detect phase transformations, such as melting and crystallization.

3.2.3 Electrochemical Characterization

Impedance spectroscopy data for ionic conductivity was collected using a Gamry Interface 1000b (Gamry Instruments) and the EIS was done on symmetric coin cells. Lithium (Li) and stainless steel (SS) discs were used as electrodes for the EIS conductivity tests. Li is a conducting and reactive electrode, whereas SS is considered a blocking a non-reactive electrode. To assemble these symmetric coin cells, the SSE powder was hot-pressed into pellets (Across International Hot-Press 25.4 mm diameter) at 1 ton, 1 MPa for 50 min. This was done to ensure the pellets are robust and also to recreate the same processing parameter while making half and full cells which will be discussed in the later chapters. The hot-press dies were cleaned in an ultrasonic bath for 30 min to ensure that the surface of the dies aren't contaminated. Once the SSE pellets were hot pressed, these were subsequently sandwiched between 11.1 mm diameter Li discs (0.6 mm thick, MSE Supplies). For SS symmetric cells, the pellet was sandwiched between SS discs (0.8 mm

thick). For all different coin cell formats, all cells were crimped using a CR2032 coin cell crimper at a pressure of 0.7 ton. To study ionic conductivity trends with respect to temperature, EIS was measured at room temperature, 40 °C, 60 °C, 80 °C, 100 °C, and 120 °C and the coin cells were held at these temperature for around 1 h to ensure the cell and SEI were stabilized at the testing condition.

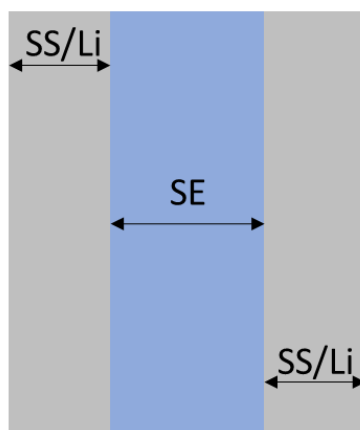


Figure 14. Symmetric CR2032 coin cells for EIS testing to measure ionic conductivity.

The electronic conductivity was measured by the Hebb-Wagner method with an asymmetrical CR2032 coin cell with SS foil (positive electrode), hot-pressed SSE pellet, and Li foil (negative electrode). At 100 °C, polarization voltages of 0.1, 1, 2, 3, 4, and 5 V were applied to the cell for 1 h using chronoamperometry with the potentiostat, and the current passing through the cell was measured. In each experiment, the cell was held at 0 V for 1 h before applying the voltages.

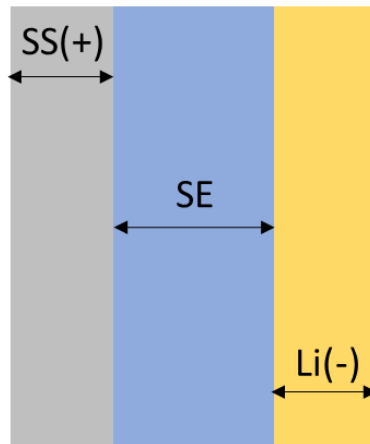


Figure 15. A symmetric CR2032 coin cell with SS (positive electrode) and Li (negative electrode) to measure electronic conductivity.

3.3 Results and Discussion

3.3.1 Synthesis of Melt-Synthesized Borohydride Based SSEs

Synthesis of the melt-synthesized solid electrolytes have never been studied before, since most work use ball milling as the method to synthesize the electrolyte. Ball milling is time and energy intensive process, whereas melt synthesis of the SSE is very quick and facile. As with all new synthesis methods, it is crucial to systematically investigate the crystal structure of the SSE in order to understand how the crystal structure and properties could change with the synthesis method.

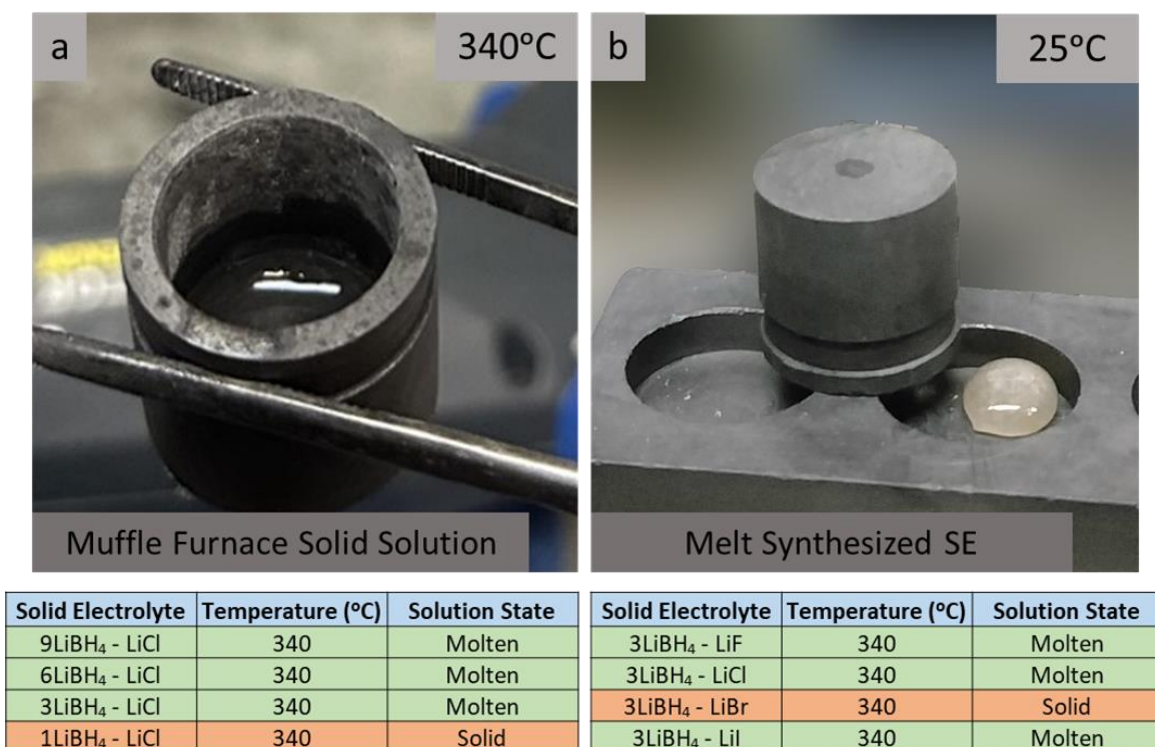


Figure 16. (a) is a picture of the solid solution in the molten form at 340 °C, where we notice a homogenous mixture and part (b) shows the solidification of the electrolyte at room temperature.

In the above figure, we have a solid solution of the 3LiBH₄-LiCl which was in the molten form at 340 °C and was solidified into a solid by quenching the SSE onto a graphite mold. We notice that the wetting with graphite mold is very poor (very high contact angle, low surface energy), and subsequently the solidified SSE can be easily grinded into a powder. Our systematic investigation on various lithium salt doping and various LiBH₄ and LiCl concentration (figure 16) has shown us that 3LiBH₄-LiBr and 1:1 LiBH₄-LiCl remain solid powders at 340 °C and thus could not be mixed uniformly. As a result, there isn't a homogenous mixture of the reactants/precursor, which may lead to inefficient doping, which is also reflected in the later results.

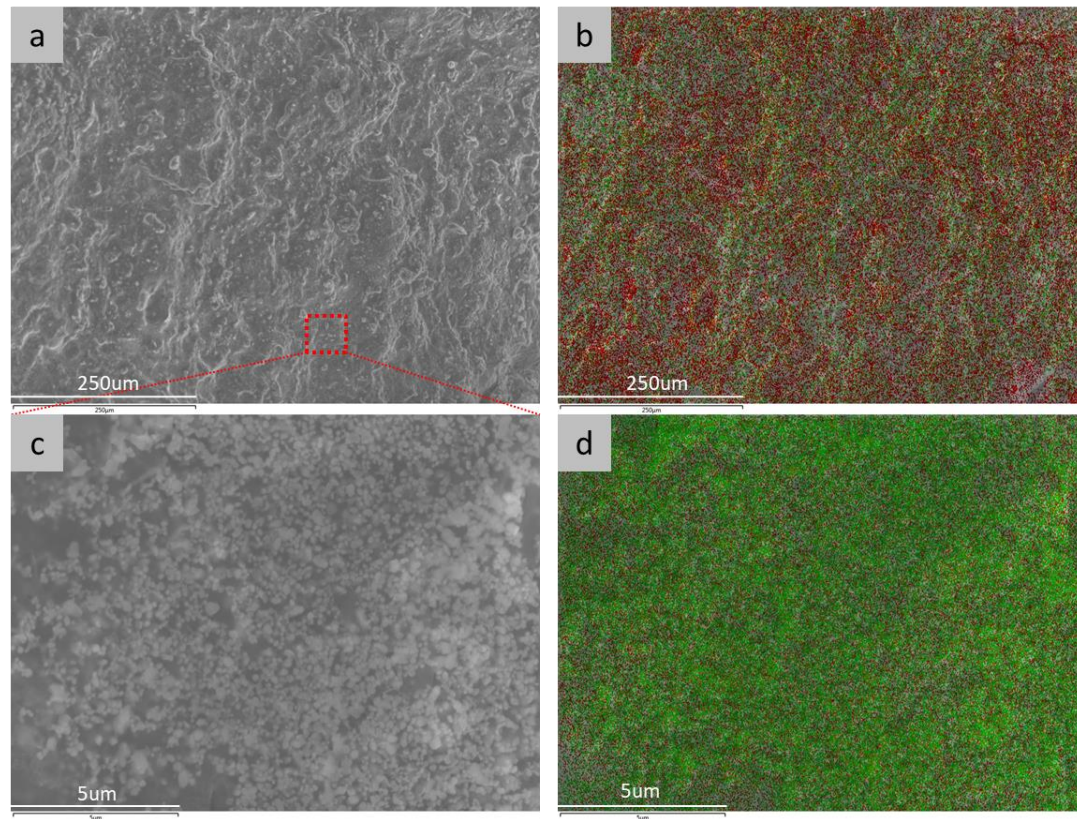


Figure 17. (a) SEM image of 3LiBH₄-LiCl and (b) EDS map of the pellet, where red and green color/shades represent boron and chlorine respectively; (c) a LiCl rich phase and (d) EDS map of the LiCl-rich phase, where red and green shades represent boron and chlorine, respectively.

SEM images (as seen in figure 17) show the interesting morphology of 3LiBH₄-LiCl, where LiCl rich regions are present in a sea of LiBH₄ rich phase (note that there are no SEM pictures of 3LiBH₄-LiCl reported in literature). Though these materials form a solid-solution at 340 °C, we hypothesize that LiCl rich regions are formed during fast cooling. These LiCl regions are uniformly dispersed all across the surface of the LiCl-doped LiBH₄ SSE.

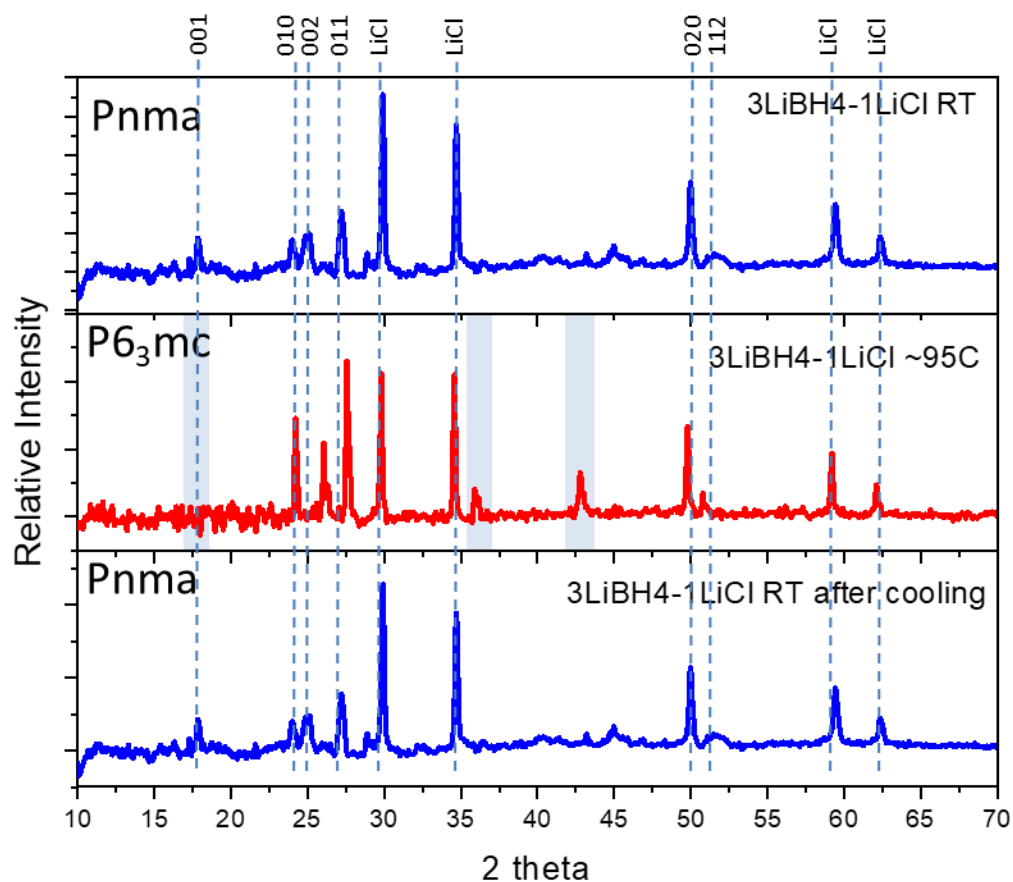


Figure 18. 3LiBH₄-LiCl SSE low temperature orthorhombic phase compared to the high temperature hexagonal phase.

In figure 18, we see that the melt-synthesized 3LiBH₄ – LiCl has an orthorhombic structure (Pnma) at room temperature with lattice parameters a , Å = 7.1480, b , Å = 4.4054 and c , Å = 6.8123 (unit volume V^3 Å³ = 214.516). We see a phase transition of 3LiBH₄ – LiCl at around ~95 °C, where it transitions from an orthorhombic structure to a hexagonal structure (P6₃mc). We can differentiate between the orthorhombic phase and the hexagonal phase by distinctive peaks disappearing at 17.5° 2θ, and 27° 2θ and peaks appearing at 36° 2θ and 52° 2θ. We notice that the unit volume size of the melt synthesized 3LiBH₄-LiCl is

lower than that of pure orthorhombic LiBH_4 (unit volume $V^3 \text{ \AA}^3 = 217.732$), which is anticipated due the smaller Cl^- anions than BH_4^- but what is interesting to note is that the unit volume size of melt-synthesized is also lower than ball-milled versions of $3\text{LiBH}_4\text{-LiCl}$ (unit volume $V^3 \text{ \AA}^3 = 215.8$).^[109] Assuming that the unit volume of size of LiBH_4 could be used to study the amount of doping/anion substitution, the smaller unit volume size of the crystals in melt-synthesized SSE is a sign that there is more anion substitution of Cl^- along the LiBH_4 matrix than the ball-milled versions.

As seen earlier, the anion doping/substitution of LiBH_4 should affect the crystal size (unit volume) of the LiBH_4 since fluorine and chlorine are smaller than the BH_4^- anion. Whereas bromine and iodine have a larger size than the BH_4^- and hence we notice that iodine doped and bromine doped versions of LiBH_4 are both hexagonal at room temperature. The orthorhombic peaks present at $17.5^\circ 2\theta$, and $27^\circ 2\theta$ for low temperature phase LiBH_4 disappear in bromine and iodine substituted LiBH_4 . This suggests that substitution with a larger anion leads to possible contraction of the “a” axis and expansion in the “b x c” plane. Though bromine substituted LiBH_4 remained solid during the melt synthesis process, we believe there is diffusion and substitution of the anions still occurring. In figure 19, we firstly notice that the $3\text{LiBH}_4\text{-LiCl}$ has a smaller unit volume than that of $3\text{LiBH}_4\text{-LiF}$ (unit volume $V^3 \text{ \AA}^3 = 215.350$), which could point towards poor diffusion of fluorine anions during the solid solution mixing process in the melt form. Poor substitution could lead to poor addition of defects, since past literature of analogous borohydride systems has shown that doping/substitution of anions may introduce additional defects^[110].

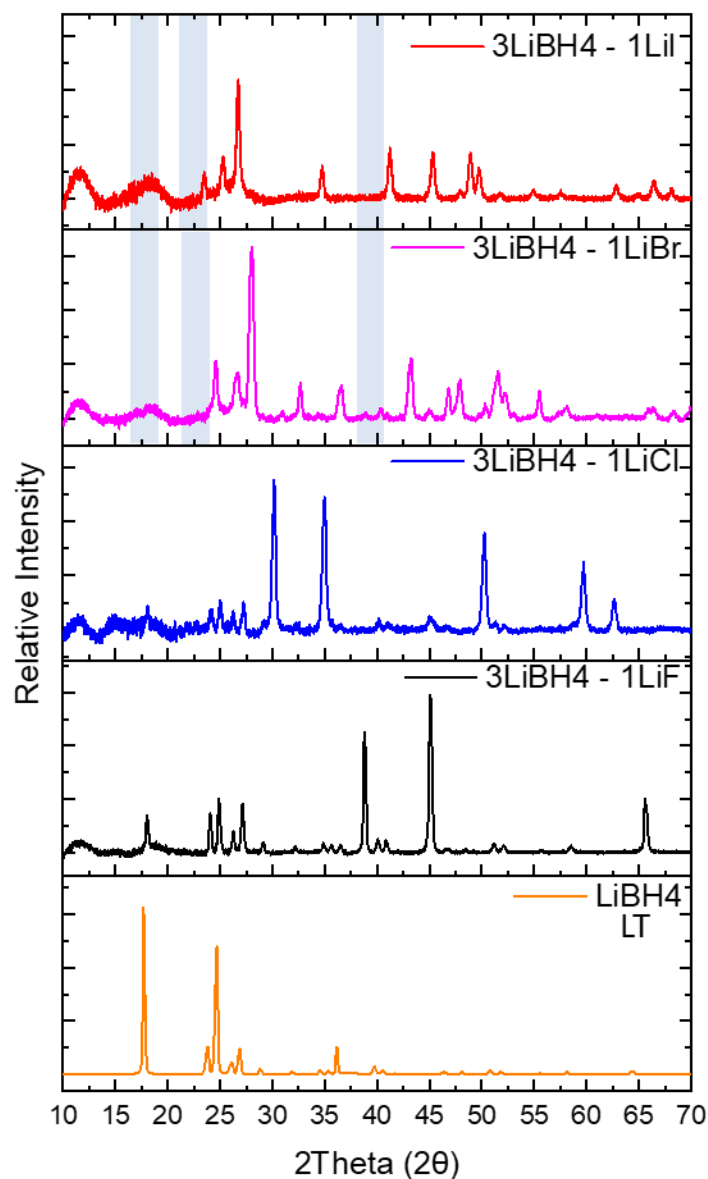


Figure 19. XRD plots of Fluorine, Chlorine, Bromine and Iodine substituted LiBH_4 SSE. Rietveld analysis of these different anion substitute/doped LiBH_4 show the increase in unit volume size with increasing halogen anion size.

Though XRD data has been effective in analyzing the unit volume size of the crystal, the extent of doping, and changes in the crystal structure with temperature, XRD was inefficient in verifying the composition and the true purity of the borohydride-based SSEs.

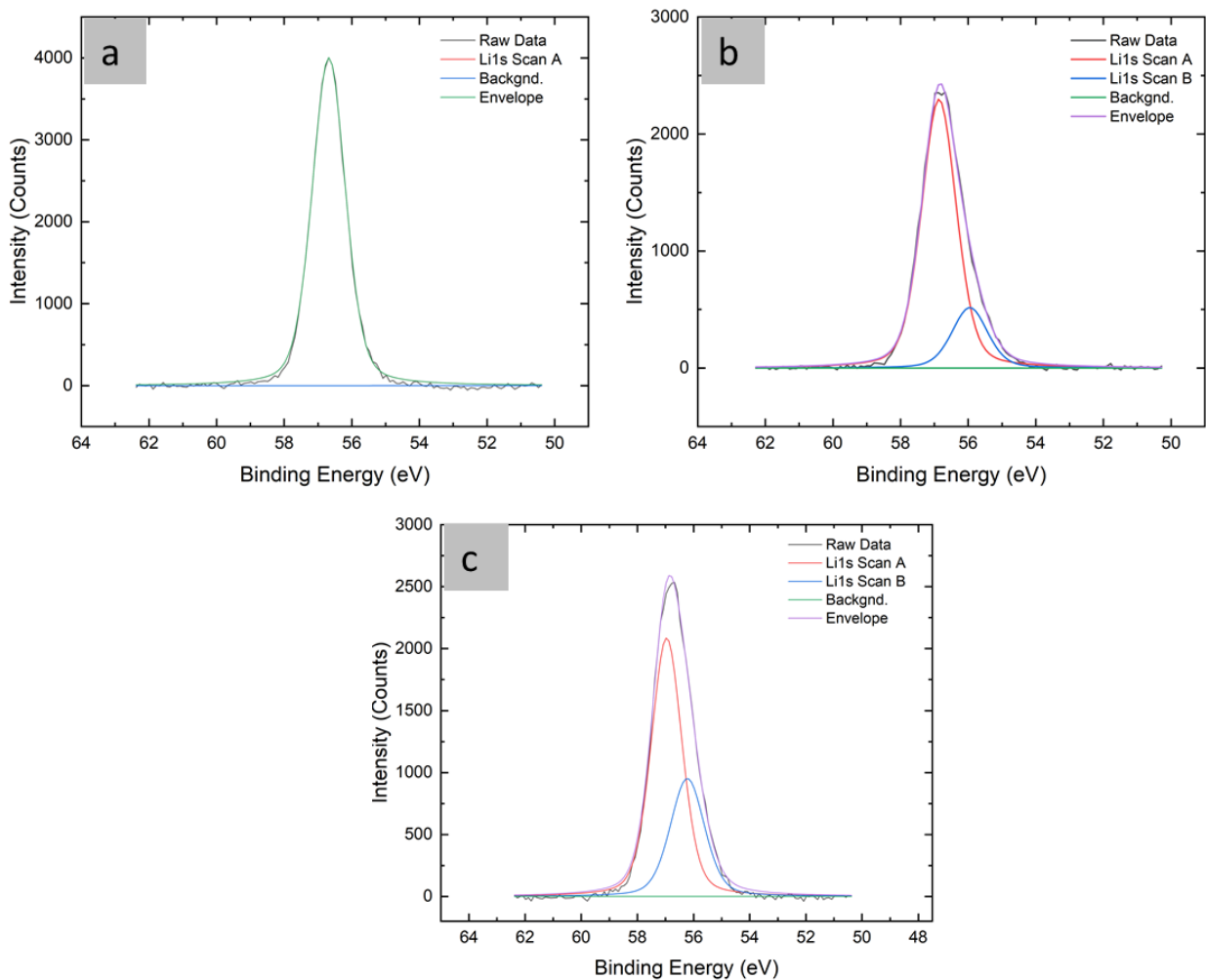


Figure 20. (a) Binding energy of LiCl; (b) Binding energy of LiBH₄ and (c) Binding energy of 3LiBH₄-LiCl.

XPS is a powerful tool which can help study the chemical composition of the SSE. Using XPS, we have systematically investigated the Li 1s peaks for our solid electrolyte system. The Li 1s binding energy peaks for the LiCl and LiBH₄ were seen at 56.68 eV and 56.86 eV respectively. We hypothesize that the additional peak for LiBH₄ is due to an impurity from the bulk sample itself or due to slight exposure to air and moisture. For 3LiBH₄-LiCl, we observe Li 1s peaks at 56.96 and 56.22 eV, which can be credited to LiBH₄ and LiCl respectively. There is no research work to confirm the LiBH₄ binding

energy for Li 1s but the binding energy for Li 1s for LiCl can be attested from past work. The composition of LiBH₄ and LiCl can be investigated by studying the area ratio of the Li 1s peaks from LiBH₄ and LiCl. We notice that based on the area ratio, the composition ratio of LiBH₄ to LiCl is 3 to 1, which is in agreement with our original precursor composition/ratio during melt-synthesis of the SSE. Based on XPS and XRD data, we can ensure that the SSE synthesized are indeed the SSE we want to produce (structurally) and have the same composition and ratio of the precursor powders used.

Various LiBH₄ and LiCl SSEs were synthesized with varying LiBH₄ concentrations to understand the extent of anion substitution. Figure 21 shows the XRD plots of SSEs with varying LiBH₄ concentrations and we notice that the anion substitution saturates at a 3:1 since 1:1 ratio doesn't show a significant improvement in chlorine substitution since the unit volume is almost the same (unit volume $V^3 \text{ \AA}^3 = 214.432$). We notice an increase in unit volume size with the reduction of LiCl concentration. During the process of melt-synthesis, we directly pour the molten SSE onto a graphite mold to solidify rapidly. As result of this process, we notice amorphous regions in the SSE with 9:1 LiBH₄: LiCl. Later sections with ionic conductivity show that these amorphous regions don't improve Li-ion conductivity. All SSEs with varying LiBH₄ are present in the orthorhombic phase and we notice no phase transitions to the hexagonal phase.

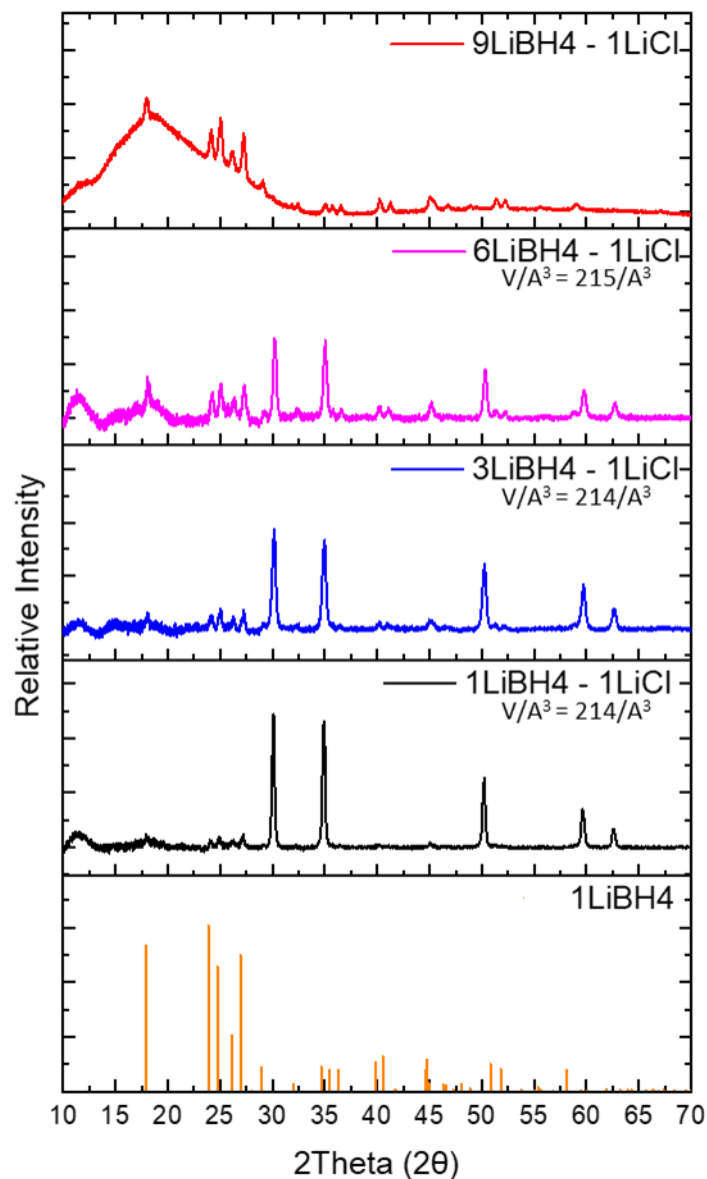


Figure 21. Varying LiCl concentration with LiBH₄ and Reitveld shows saturation of anion substitution at 1:1 ratio of LiBH₄ and LiCl.

As we substitute LiBH₄ with varying amounts of LiCl and with varying lithium halide salts, the phase transition temperature from orthorhombic to hexagonal is going to change (Pnma to P6₃mc). The DSC was used to study the phase transition temperatures of the various SSEs made. Since the anion size of the lithium salt vary in size, we assume that

the phase transition temperature should change, which has also been reported in various research work.

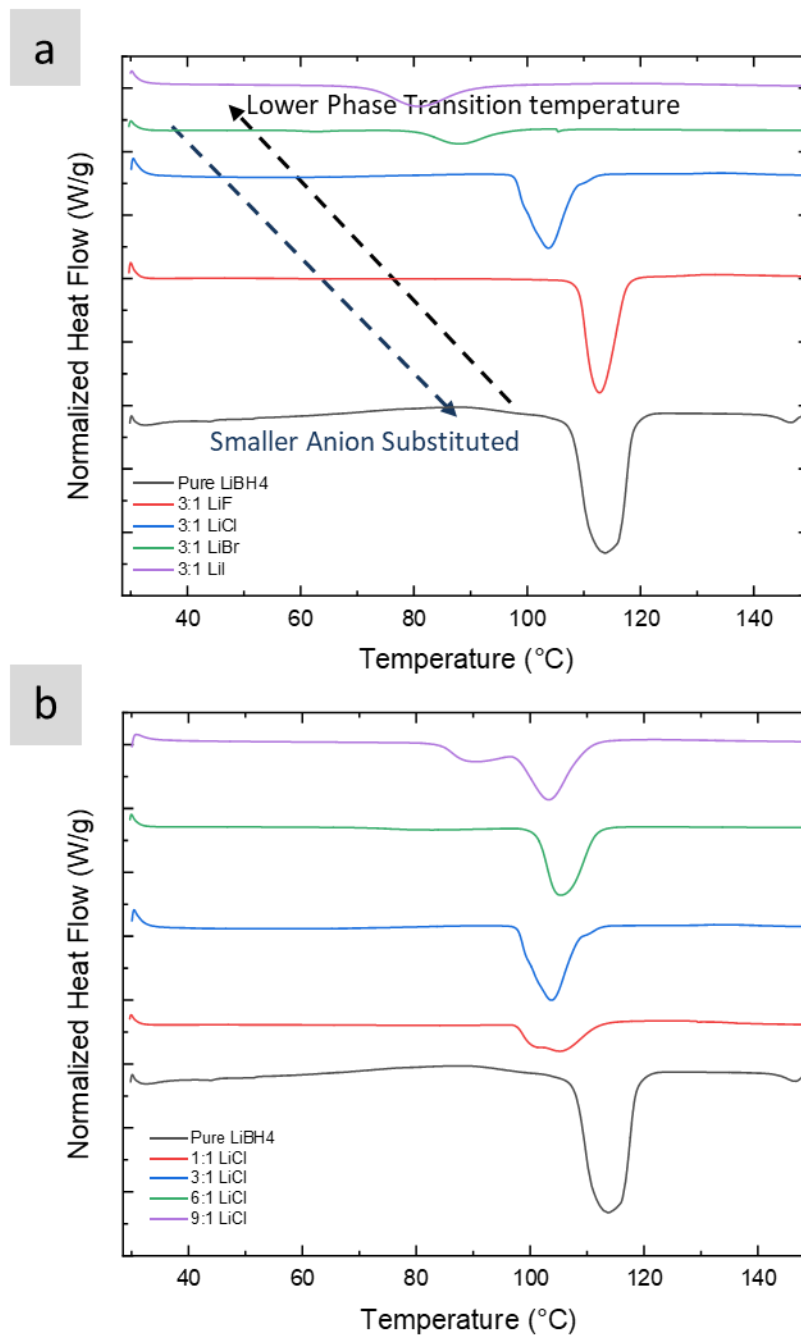


Figure 22. DSC isotherms of LiBH₄ substituted with various halide salts and varying LiCl.

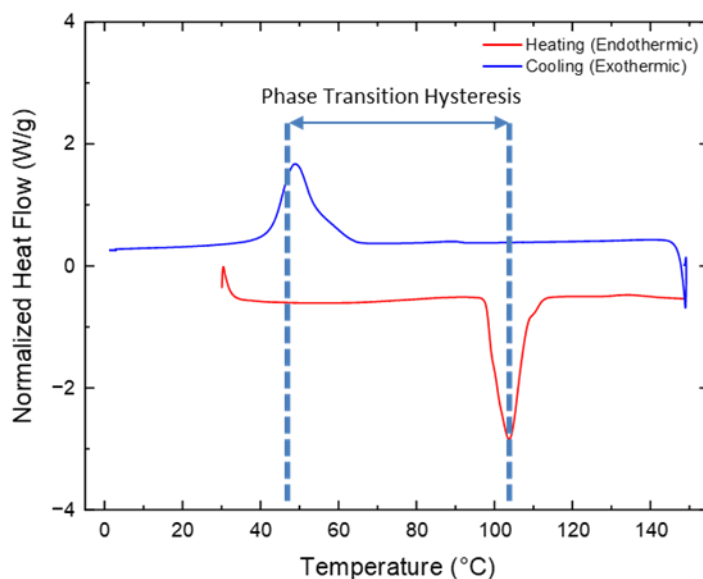


Figure 23. Heating and cooling curves of 3LiBH₄-LiCl, with phase transition hysteresis.

DSC isotherms of various halides salts substituted in the LiBH₄ SSE has been studied as seen in figure 22. We notice that bromine and iodine substituted electrolyte have some residual LiBH₄ phase transition though they are hexagonal at room temperature, and for chlorine and fluorine substituted SSEs; there is a decrease in the phase transition temperature. Interestingly, fluorine substitution in LiBH₄ doesn't significantly decrease the phase transition temperature. The mechanism of varying transition temperatures is still not well studied. Past studies suggest that the mechanism of the transition may be related to the degree of freedom of the re-orientational motion of BH₄⁻ anion, which could be affected by varying anion sizes.^[111] Studies suggest that BH₄⁻ are in a disordered orientation until the phase transition, but become more ordered after the transition temperature. In addition, Raman line widths were studied for different alkali borohydrides and it was suggested that this energy barrier decreased as a function of cation size.^[112] Thus it is plausible that the

correlation among BH_4^- is influenced by the geometric alteration such as inter BH_4^- distance, substituted anion size and unit cell volume, as a result the transition temperature is modified.^[111] When the LiBH_4 to LiCl concentration varied, we notice that 1:1 and 3:1 have very similar transition temperature, which can be hypothesized as having very similar LiCl substitution since unit volumes are very similar. Since 9:1 has amorphous regions, its phase transition could change due to a completely different structural dynamics. We also observe, due the reorientation motion of BH_4^- , a large hysteresis in the heating and cooling cycle phase transitions for all the SSEs mentioned except pure LiBH_4 (as shown in figure 23 specifically for $3\text{LiBH}_4\text{-LiCl}$). The cooling phase transition from hexagonal to orthorhombic is seen at 50°C .

We can conclude looking at XRD, XPS and DSC data that we have indeed synthesized the SSEs with the right chemical composition and have the same structure of that ball-milled versions that have been widely used in literature as mentioned before. We were then ready to study the electrochemical properties of these various SSEs using impedance spectroscopy, Li symmetric cell testing and Arbin charge and discharge cell testing.

3.3.2 Electrochemical testing for Ionic Conductivity and Cyclic Voltammetry.

EIS was used ubiquitously to study the ionic conductivity of solid electrolytes, where Nyquist plots obtained from EIS is fitted to an equivalent circuit to measure various phenomenon in the cell being tested. Ohms law is generally used to calculate the conductivity of the electrolyte since the thickness and the area of the electrolyte exposed to the electrodes is a known quantity (equation 17)

$$\sigma = \frac{RA}{L} \quad (17)$$

LIBs are complicated systems which do not follow ideal Ohms law. They can have complex circuits due complex chemical phenomenon such as double layers, constant phase elements and electrolyte diffusion. In the case of ionic conductivity of solid electrolytes, the solid electrolyte is sandwiched between stainless steel or lithium foils.

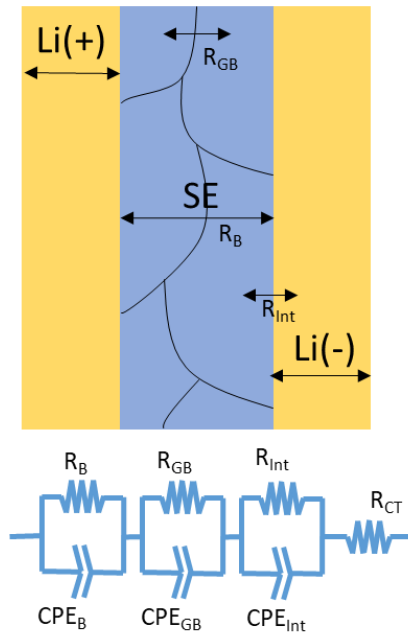


Figure 24. Lithium symmetric cell equivalent circuit to fit a Nyquist plot.

In figure 24, we have a schematic of a lithium symmetric cell with a solid electrolyte pellet. We assume that cold press pellets have grain boundaries since they aren't annealed to ensure grain boundary effects on resistance are minimized.^[113] For a cold pressed SSE lithium symmetric cell, the major contributors to resistances would be bulk resistance from the electrolyte, grain boundary resistance and a resistance from the interface formed with Li, since lithium is a very reactive metal. There is also a charge transfer resistance since it arises from the resistance of flow of electrons through lithium metal.

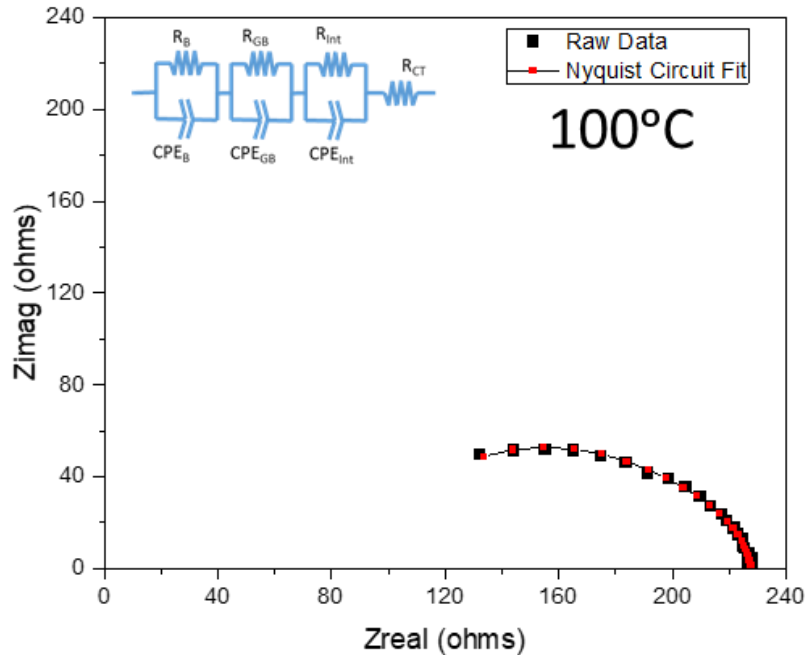


Figure 25. A lithium symmetric cell with SSE at 100°C fitted with the equivalent circuit mentioned above.

As we see in the above figure, the fitted data is very accurate, which implies that the circuit does indeed represent the different components of the cell. Though a lithium symmetric cell is a known method to study the ionic conductivity of our solid electrolytes, the ionic conductivity measure using this method doesn't directly correlate to the actual environment of the solid electrolyte in the full cell charge discharge testing. In addition to recreating actual testing environments (seen in the full cell fabrication part) and to reduce complex fabrication of making lithium symmetric cells (since lithium is a soft metal and can easily break the solid electrolyte pellet during the crimping process), we hot-pressed the solid electrolyte pellet to make sure we minimize the effects of grain boundary

resistance. Also, stainless steel foil/spacers were used to ensure that pellets don't crack and break during the cell crimping process. Though stainless steel is a blocking electrode, it is still used widely as inert electrode to measure ionic conductivity^[114]. Also, blocking electrodes are inert to solid electrolytes and generally, don't form complex interfaces.^[115] We fabricate SS/SSE/SS, with the solid electrolyte hot-pressed at 50°C and 78 MPa for 1 h.

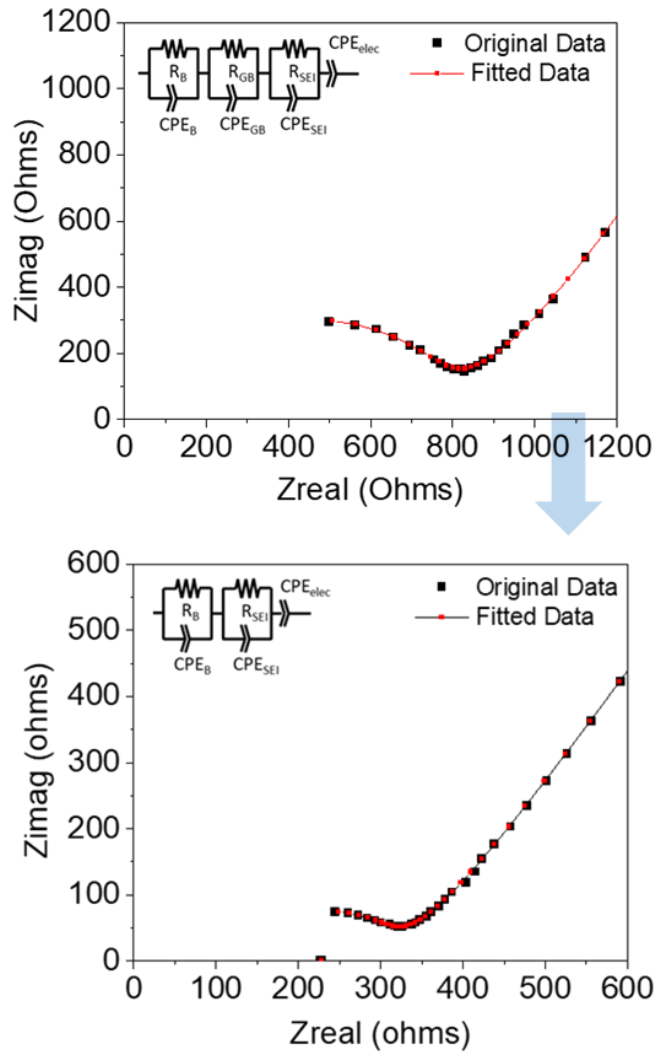


Figure 26. Nyquist plot of a SS symmetric cells with 3LiBH₄-LiCl, with a diffusive peak which is unique to a blocking electrode case.

As seen in figure 26, the SS symmetric cell produced a Nyquist plot with a straight line at low frequencies (marked by the tail), which can be modeled by a phase element since it isn't an exact diffusive process that occurs at the boundary of the SS electrode and SSE. For a SS symmetrical cell, SS is a blocking electrode that forms a double layer capacitance at the interface between electrode and electrolyte, which ideally creates a 90° straight line. Also, the SS symmetrical cells, the straight lines in Nyquist plots are not exactly 90° and 45° (which would be for diffusion of lithium ion through a certain space), respectively. The reason could be the irregularities in the electrode/electrolyte interface geometry. Hence a constant phase element was used to model the straight line produced at very low frequencies.

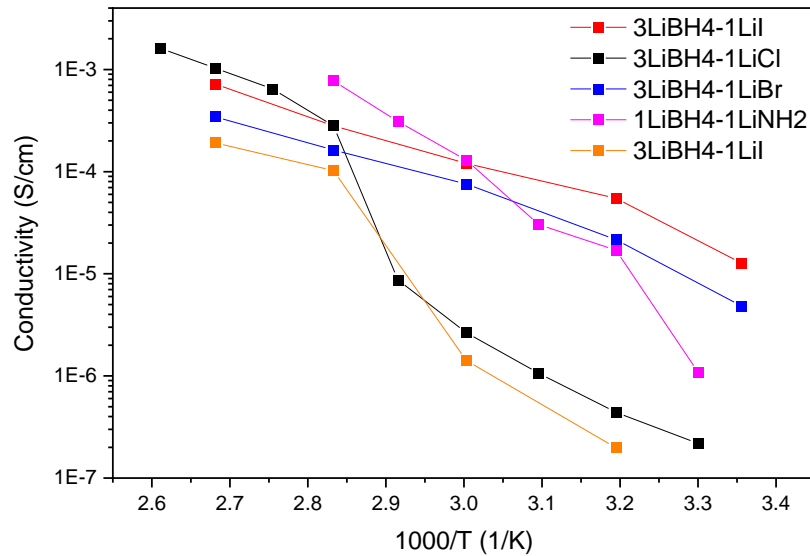


Figure 27. Li^+ ion conductivities of LiBH_4 based SSEs with different halide salts substituted.

We have discussed the structure and chemical composition of the SSEs in the previous sections, but it is important to study the Li^+ ion conductivity since it dictates how fast Li^+ ions can be shuttled. It plays a crucial role in deciding charge and discharge rates, since slow Li^+ ion conductivity can cause several issues including lithium dendrite growth at very high current charging rates. Out of the different salts synthesized, $3\text{LiBH}_4\text{-LiCl}$ shows the highest conductivity followed by the iodine anion substituted version. Lithium amide has a low melting point of $80\text{ }^\circ\text{C}$, so it will not be considered for experiments. Ideally, we would hypothesize that with a lower transition temperature, and with a larger anion substituted that the Li^+ ion conductivity should improve, but the correlation between ionic conductivity and salt substitution is much more complex. These salts form different types of interfaces with SS and have different grain size and these grains mechanistically differ for the same hot-pressing conditions. Contrary to popular belief that the ionic conductivity of the borohydride SSE is largely dependent on the phase transition temperature^[84, 87, 90, 94, 96, 97, 99, 116], we notice a complex correlation between the melt synthesized SSEs transition temperature and the ionic conductivity (when the ionic conductivity was measured during the cooling phase from $110\text{ }^\circ\text{C}$ to $20\text{ }^\circ\text{C}$). LiCl , LiBr and LiI anion substituted SSEs, have a cooling phase transition temperature at $65\text{ }^\circ\text{C}$ ($1000/T = 3.14$) or below (note $20\text{ }^\circ\text{C}$ corresponds to $1000/T = 3.41$), and we see from figure 27, that there is sharp decrease in the ionic conductivity during these temperatures. For $3\text{LiBH}_4\text{-LiCl}$ in specific, as in figure 28, we notice the transition from orthorhombic to hexagonal at $\sim 95^\circ\text{C}$ and we do notice a large increase in the ionic conductivity, but during the cooling cycle (the transition from hexagonal to orthorhombic to hexagonal occurs at $\sim 65^\circ\text{C}$) we realize a rapid decrease in conductivity $\sim 65\text{ }^\circ\text{C}$. We notice a hysteresis in the

cooling phase and heating phase conductivity at the orthorhombic structure. Hence, the ionic conductivity for these melt-synthesized electrolytes isn't purely dependent on the phase transition temperature, but also the defects that could be reduced during the fast cooling process of the molten electrolyte.

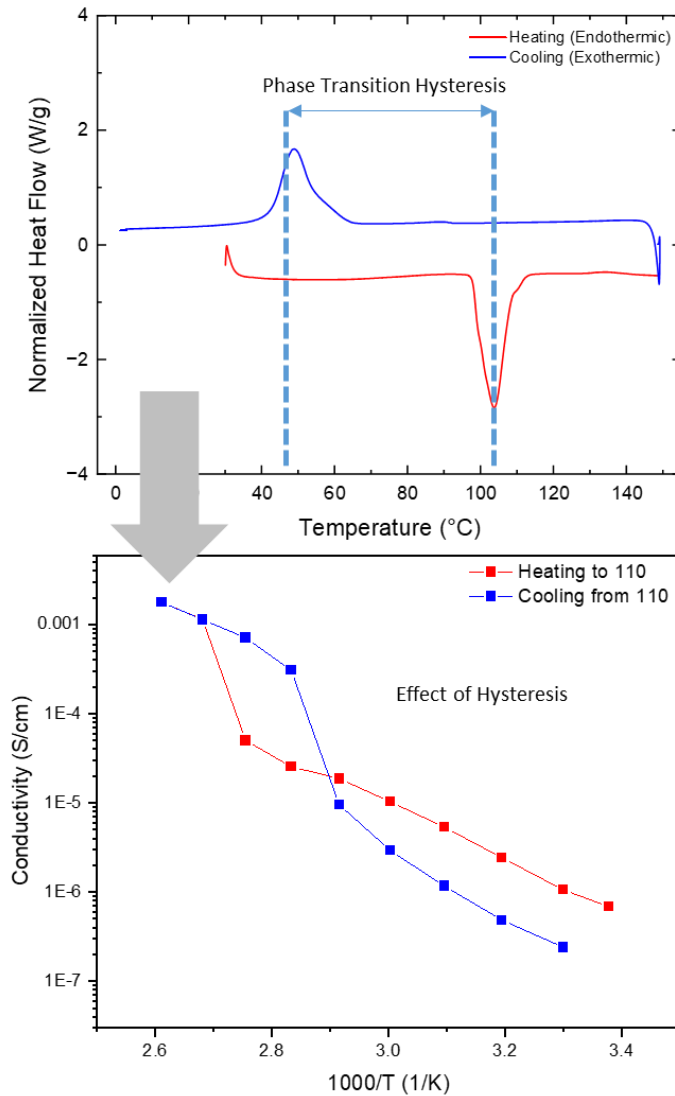


Figure 28. Effect of transition temperature hysteresis on ionic conductivity of 3LiBH₄-LiCl SSE.

As ionic conductivity is crucial for LIB performance, $3\text{LiBH}_4\text{-LiCl}$ is used as the electrolyte for further electrochemical testing because of its highest ionic conductivity compared to other electrolytes synthesized.

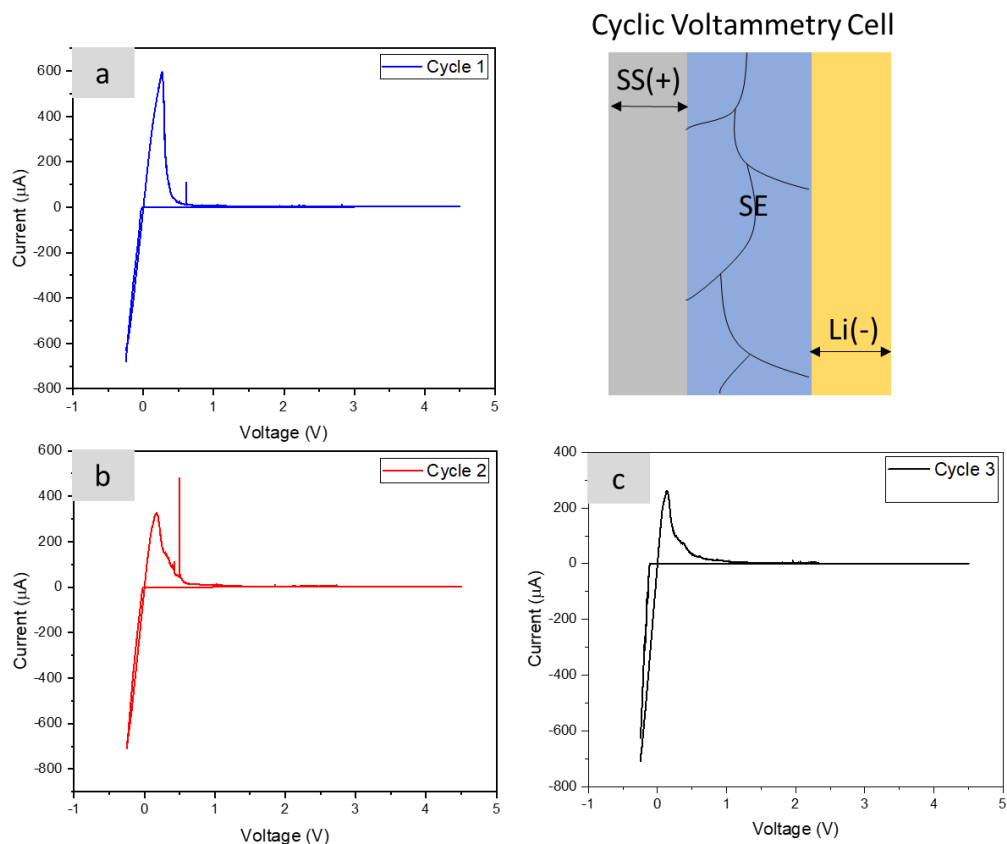


Figure 29. CV was performed on SSEs sandwiched between SS and Li foil. We have the CV plots for $3\text{LiBH}_4\text{-LiCl}$ in this figure.

A high ionic conductivity plays a crucial role in minimizing the ohmic resistance of a battery, but it is also important to study the electrochemical stability window of the solid electrolyte since it helps us understand what type of AMs are compatible with a certain electrolyte. In addition to studying the voltage window the SSE is stable in, it helps us also understand different side reactions that could possibly occur with various AMs. CV were studied by making SS foil and Li foil asymmetric cell with the SSE sandwiched

in between (SS/SSE/Li). The electrochemical stability window (ESW) of $\text{LiBH}_4\text{-LiCl}$ isn't well studied at high or low voltages.^[96] Asymmetric CV cells were made, and cycled between -0.5V to 4.5V (vs Li/Li^+) at a scan rate of 1mV s^{-1} . The upper limit was set to be 4.5 V because most high voltage cathode materials, such as LCO, NMC811, or NCA only work at voltages below 4.5 V vs. Li/Li^+ . CV was measured at 100 °C since electrolyte conductivity at room temperature is low and want to elucidate side reactions. Figure 29 (a) shows the first cycle of CV for $3\text{LiBH}_4\text{-LiCl}$ SSE and we notice two signature peaks at around 0V. This is significant of stripping and plating of lithium from the surface of lithium to the surface of SS respectively.^[117] No significant currents peaks have been noticed due to electrolyte decomposition were detected in the scanned voltage range.^[118] We do notice some current spikes in the CV data but they are considered noise due to their very narrow profile. CV is done for 3 cycles to ensure repeatability in the data and to ensure no subsequent side reactions occur after the first cycle. Also, during the first cycle, we do expect the formation of an SEI on the lithium foil side since lithium metal is very reductive. These decompositions can be of all sorts (like LiF , borohydride complexes, etc.) but it is hard to de-convolute due their sensitivity to air and moisture and being very fragile and thin.

In conclusion, $3\text{LiBH}_4\text{-LiCl}$ is stable across a large voltage window when a potential is applied and especially with lithium. A lot of SSEs are not stable with lithium since form side products such as H_2S , Li_2CO_3 or LiOH , so our melt-synthesized SSE is a good candidate for anode side SSEs.^[119]

Though CV is a powerful method to study the stability with various anodes and cathodes, however it is important to understand how stable SSEs are with lithium metal

since lithium metal has been become an attractive anode cathode candidate due to its high capacity. In addition to lithium metal being an interesting anode candidate for lithium metal batteries, it is also essential to study the plating stripping voltages of a SSE to understand their critical current density and it's resistance to dendrite growth. A critical current density is defined as the result of dendrite formation on plating and eventually, cell failure.^[101] When the stripping current density removes Li from the interface faster than it can be replenished (as seen in figure 30), voids form in the Li at the interface (with solid electrolyte) and accumulate on cycling, as a result increasing the local current density at the interface (due to the reduction of surface area exposed for plating), leading to dendrite formation on plating, and finally short circuits.^[101]

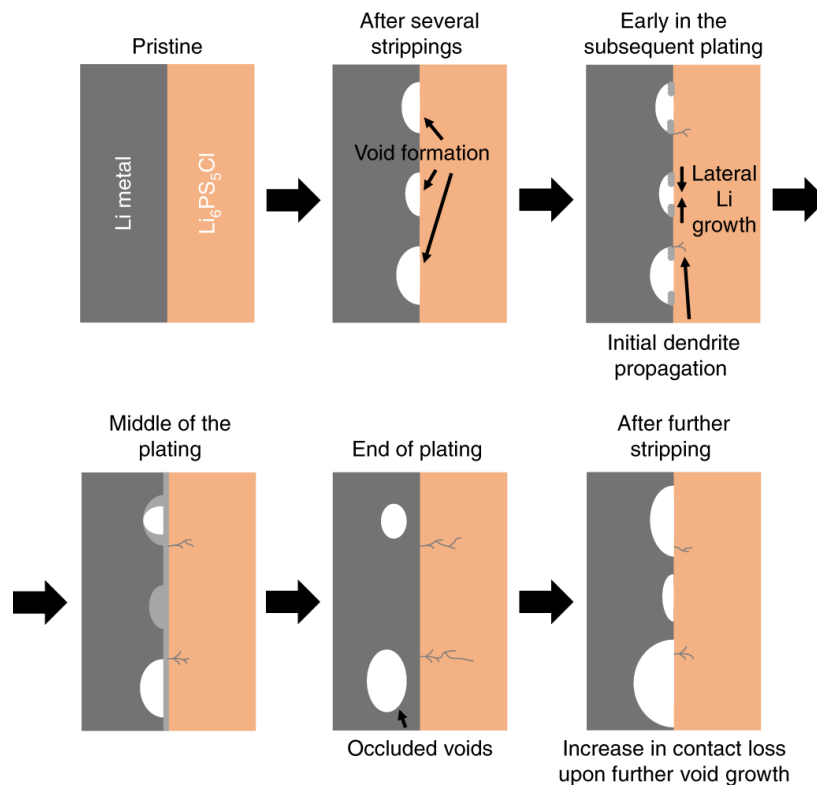


Figure 30. Formation of lithium dendrites from repeated stripping and plating. First voids are formed and form a 3 interphase point between the solid electrolyte, lithium and the void. These act as nucleation points for lithium dendrites to grow.

In order to study and understand the plating dynamics and critical current density of $3\text{LiBH}_4\text{-LiCl}$, we tested symmetric lithium metal cells with a hot-pressed pellet sandwiched in between. A DC galvanostatic cycling was done at various current densities to study the over potential and the critical current density. At $100\text{ }^\circ\text{C}$, constant DC currents of 0.01 , 0.05 , 0.1 , and 0.5 mA cm^{-2} with periodically (30 minutes) changed polarity were applied to the cells for 50 cycles at each current, during which Li metal was stripped and plated at each electrode. Additional cycles were done for 0.1 and 0.5 mA cm^{-2} since they are considered comparatively high rate.

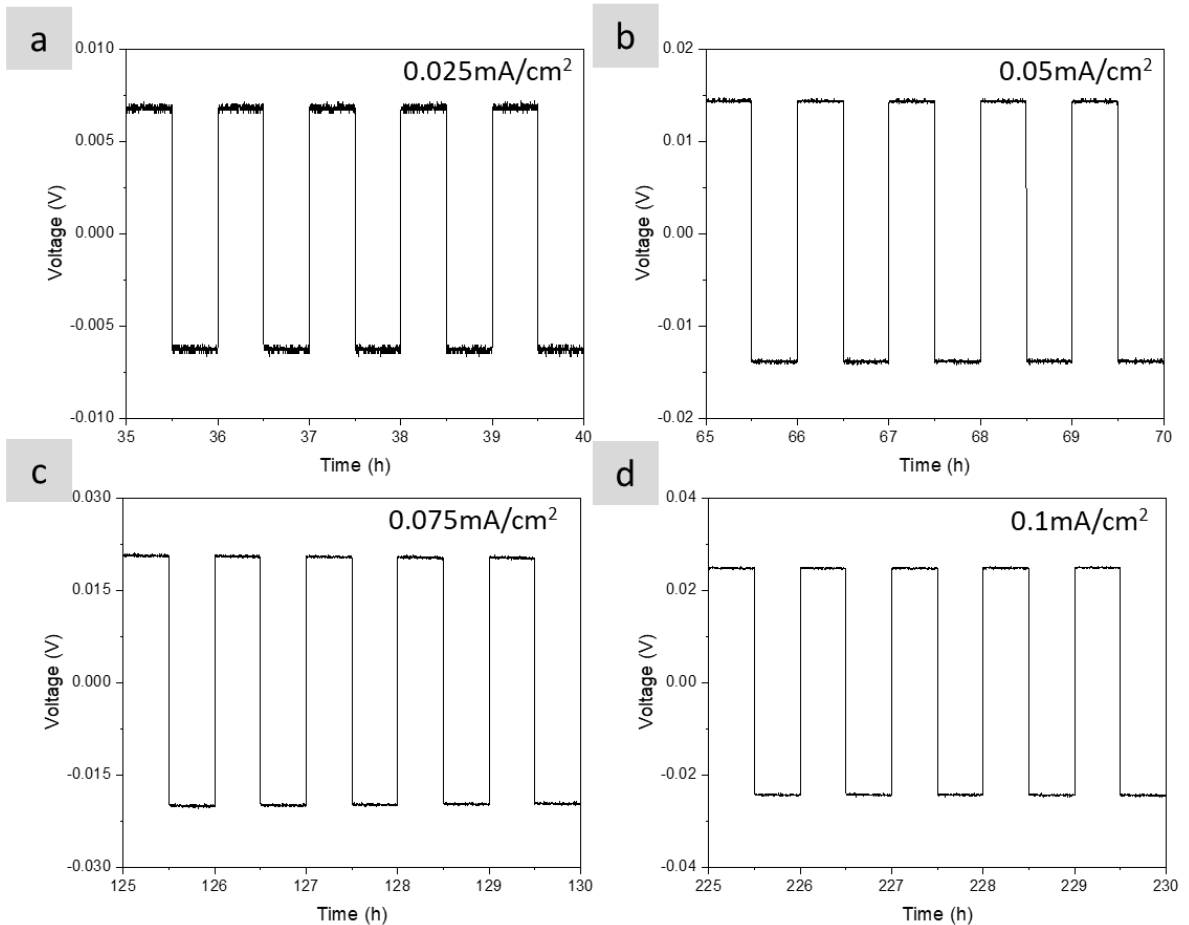


Figure 31. Voltage response to current pulses (DC cycling of Li//HPSE//Li) at different current densities.

We notice from figure 31 and 32 that the voltage remains constant along current densities of 0.025, 0.05, 0.075 and 0.1 mA cm⁻². There is no increase or decrease in the voltage during these cycling current densities. We also notice that the voltage profiles have a squared profile rather than an “arc” style profile, which entails that the movement of lithium ion is dominated by migration but not diffusion.^[120] The stable cycling over hours at various current densities represents a robust SEI that has been formed during the initial cycles of cycling. Since there no increase in the overpotential during cycling from current densities at 0.025 to 0.1 mA cm⁻² (except during the step change of current densities), there is no sign of increase in the resistance due to charge transfer, ohmic resistance or SEI resistance. But at higher current densities (0.5 mA cm⁻²), the overpotential increases.

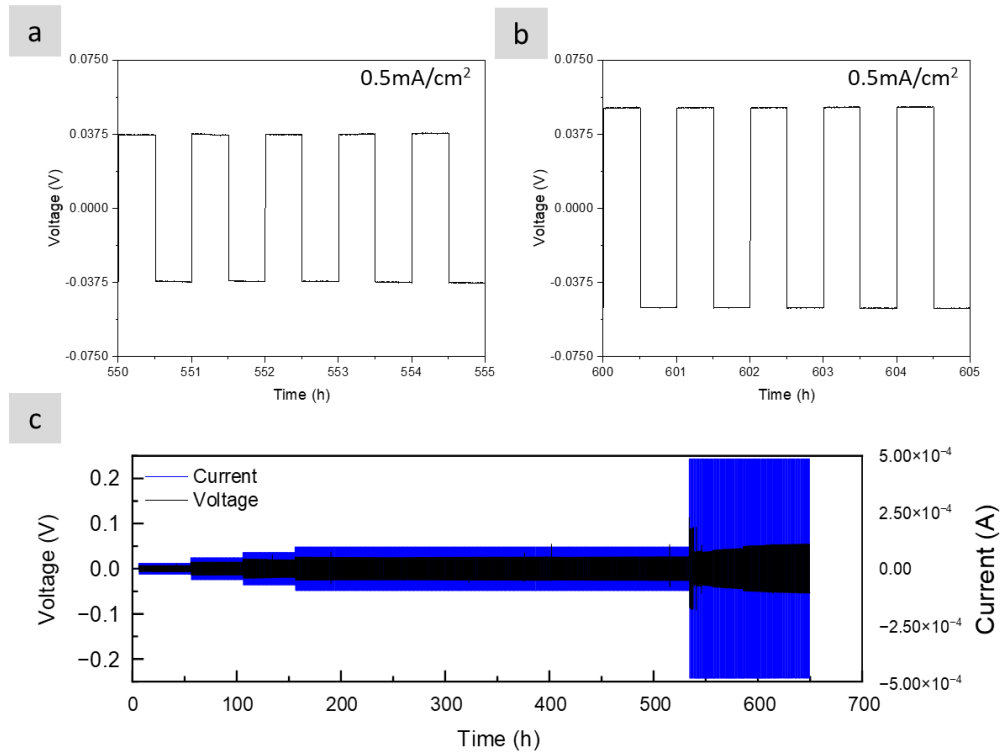


Figure 32. Voltage response to a current pulse at high current densities (0.5 mA cm⁻²) and (c) long-term cycling of symmetric cells of 3LiBH₄-LiCl.

Figure 32 (c) shows cycling for 650 h and we notice a gradual increase in the overpotential at 0.5 mA cm^{-2} , which is further magnified in figure 32 (a) and (b). Since there is no arc in the overpotential curves^[121], we could assume that the SEI or surface resistance is increasing with time due to the growth of dendrites or formation of voids. When the SEI layers are thick and the current density is large, the thick resistive SEI layers may not accommodate the fast Li-ion transport, and Li dendrites may grow at places with pre-existing cracks and voids or where the SEI layer is thinner because the localized current density at these points are a lot higher. The assumption of thick SEI layer is also enforced by studying the chemical composition of the SSE ($3\text{LiBH}_4\text{-LiCl}$) using XPS. A change in the chemical composition of the electrolyte, would affect the ohmic resistance of the electrolyte.

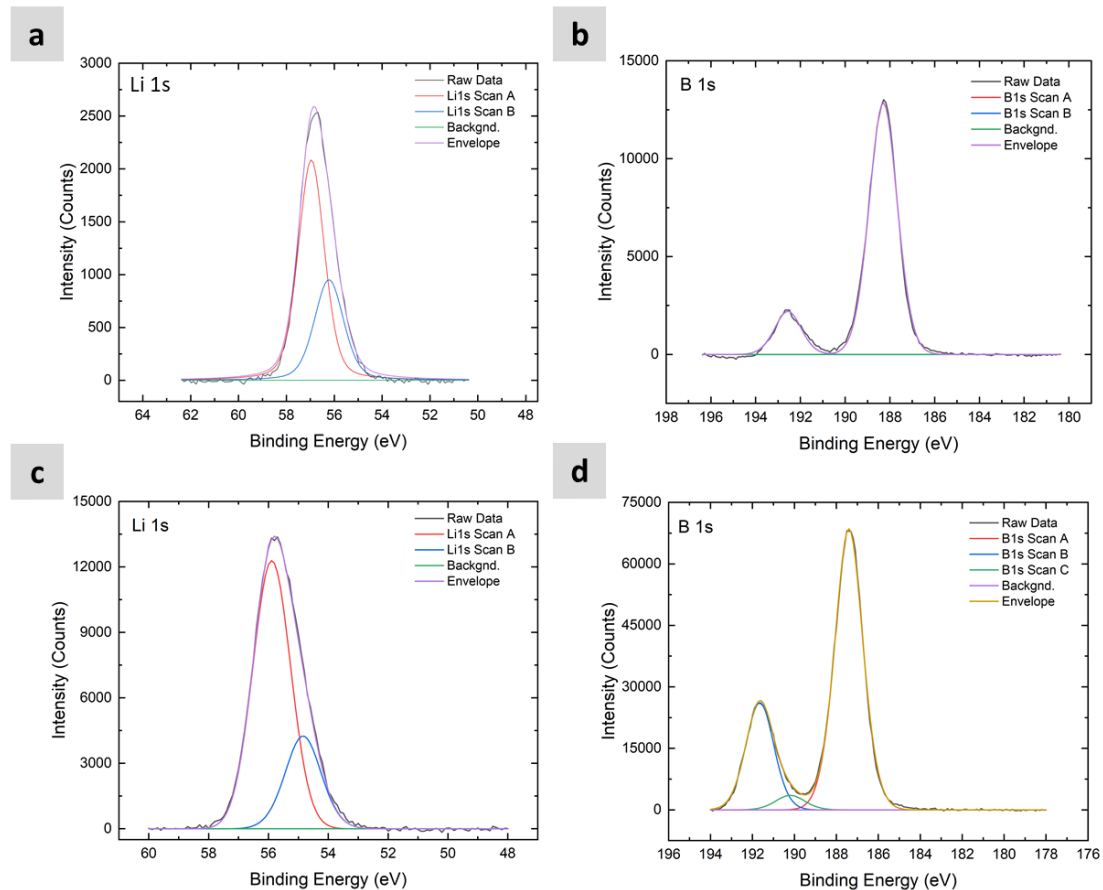


Figure 33. XPS analysis of pristine and cycled (Li//HPSE//Li) 3LiBH₄-LiCl.

As seen in the earlier section, Li 1s peaks for 3LiBH₄-LiCl were noticed at 56.96 eV and 56.22 eV which correspond to LiBH₄ and LiCl (as seen in figure 33(a)). These peaks remain the same even after cycling the cells for 900 hours as seen in figure 33(b), displaying no change in the lithium composition. But we notice a small peak arise in the cycled SE (~190.2 eV) when looking at the B 1s spectrum and increase in the intensity of the peak at ~ 193 eV. The peak at ~ 193 eV can be assigned to B₂O₃, which could be an impurity in the pristine sample. The increase in intensity of B₂O₃ could be possibly due to exposure to air and moisture from a leak in the cell casing since these coin cells are cycled at 100°C. Since there is no major chemical change in the structure of the SSE, we can

assume that the ohmic resistance of the electrolyte shouldn't be altered during long term cycling.

3.3.3 *Electrochemical performance of All-Solid-State Batteries with 3LiBH₄-LiCl*

As we have gone over the chemical and electrochemical properties of the various electrolytes and 3LiBH₄-LiCl in specific, in the next sections we study the use of 3LiBH₄-LiCl as the electrolyte with various active materials which is studied by DSC and half-cell performance. We used the “melt infiltration method” to make half-cells and full-cells, which has been published by our group in earlier studies.^[122] Since melt-infiltration of the SSE occurs at an elevated temperature (~ 290°C as seen in figure 34), it is important to understand the thermal stability of the SSE with various active materials.

In this study, we used graphite and a silicon-carbon composites as the anodes which are relatively stable at high temperatures (as seen in figure 31). Whereas, the selection of cathode materials are limited since there are only a few cathode materials that are thermal stable at high temperatures. NMC111, which has lower nickel content than NMC532, NMC811 or NCA is thermal stable up to 350 °C, whereas NMC811 and NMC532 are only thermally stable up to 220 °C due to Ni-O bonds being weak.^[123] Since higher Ni variants have lower stability, either new low melting electrolytes have to be used, or cathode materials with high thermal stability have to be used such as lithium sulfide, or lithium iron phosphate (LFP).

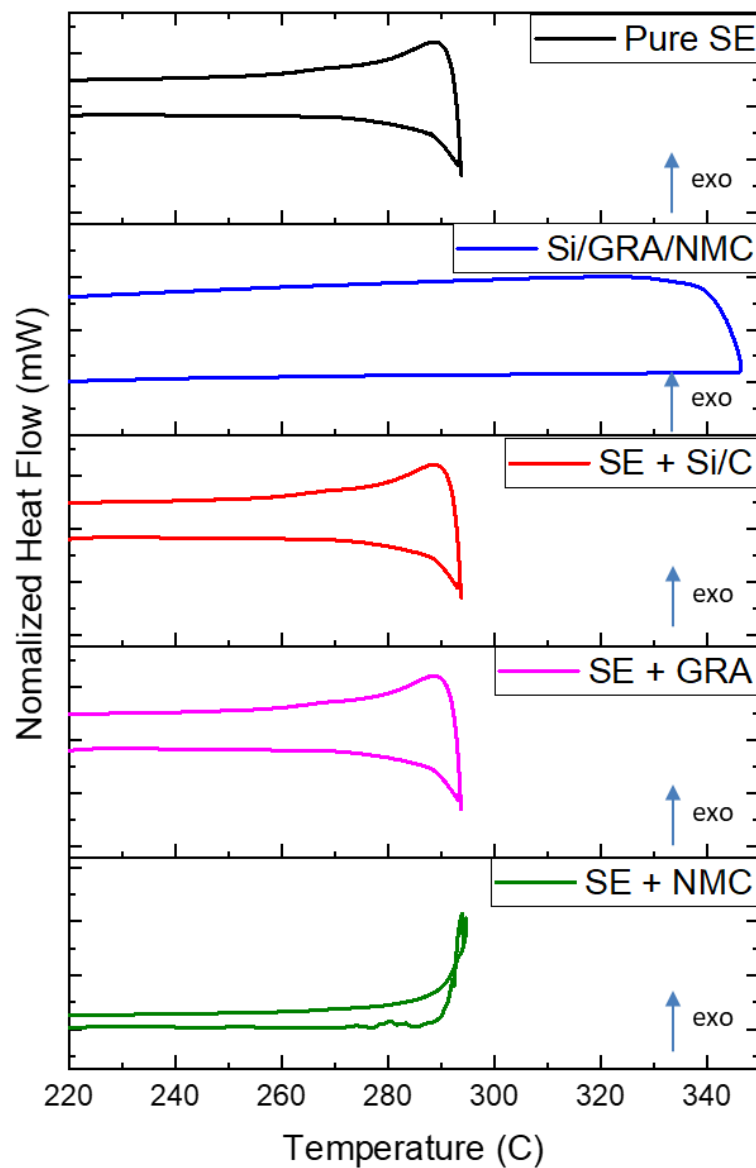


Figure 34. DSC isotherms of SSE, the electrodes alone and SSE mixed with various active materials.

One of the biggest advantages of borohydride-based SSE is their low melting points which potentially, allows their use in the proposed melt-infiltration technology (as seen in figure 34). The melting points of the materials can be determined by differential scanning

calorimetry (DSC). We see in figure 34 (through DSC isotherms), that when the solid electrolyte is mixed with various electrode materials, such as graphite and silicon-carbon composites (all powders with coated with Al_2O_3 to improve electrolyte wetting, $\sim 40 - 60$ nm coating), we notice no side reactions which would be noticed through an exothermic peak.^[122, 124] The endothermic peak which was observed at around 290°C corresponding to the electrolyte melting. Although the anodes selected are inert with the electrolyte at high temperatures, we notice that NMC111 reacts with electrolytes (which is observed by an exothermic peak at 280°C). We believe that since LiBH_4 is reducing in nature, and at high temperatures, LiBH_4 reduces NMC111 into various decomposition products.

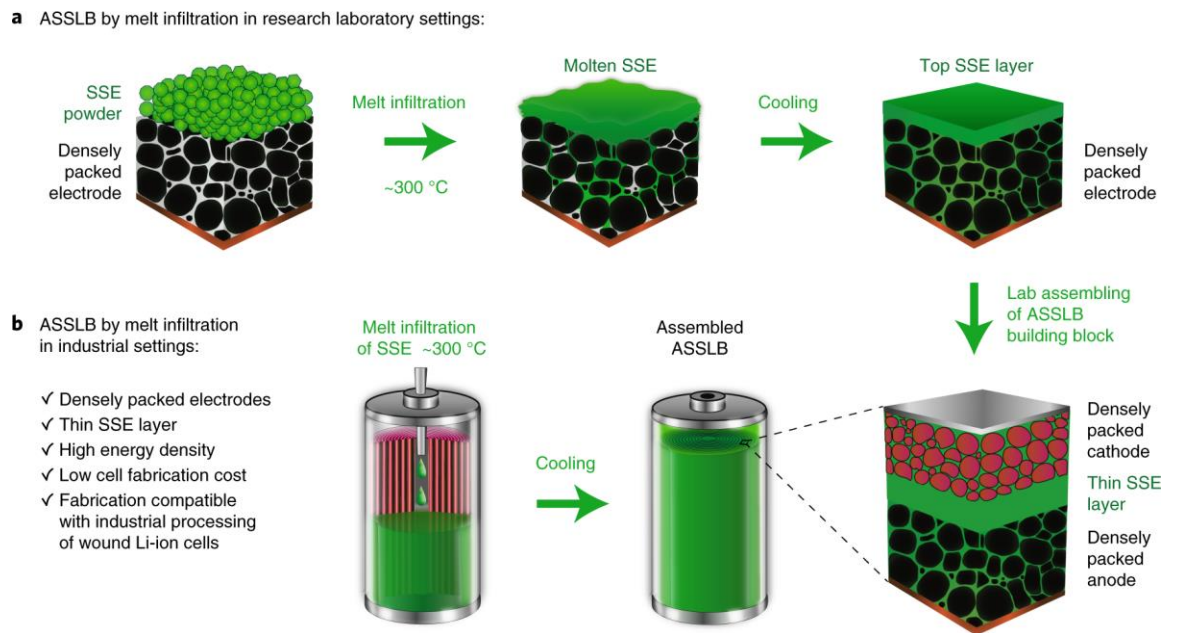


Figure 35. Melt-infiltration of solid electrolytes into electrodes which drastically reduces processing time and complexity of all solid electrolyte battery.^[122]

Graphite and silicon-carbon composite active materials were coated on copper foil using PVDF-Torlon® and carbon black as the binder and the electronic additives respectively. These electrodes are later coated with a thin layer of alumina (400 cycles of

alumina deposition using an ALD) to ensure good wetting between the electrolyte and the electrode. SEM and EDS were used to characterize the melt-infiltrated electrodes. EDS mapping of the cross-sections of the silicon-carbon electrodes (as in figure 36), and the electrodes showed complete infiltration of the SSE (green shade) within the porous structure of the electrodes down to the current collector (with a complete thickness of around 60 μm), proving the effectiveness of the melt-infiltration of the solid electrolyte. The amount of the SSE dry casted on the surface of the electrode was controlled so that the thickness of the SSE remaining on the top surface of the electrode after melt-infiltration could be tailored to a small (5-25 μm) thickness. SEM images and EDS mapping images also demonstrated a perfect wetting with a sharp interface between active materials and the SSE. Such a perfect wetting might enable minimal interfacial impedances at the interfaces between active materials and the SSE. We see that all the silicon-carbon composite particles are well coated with a layer of electrolyte with minimum amounts of pores (existing pores could be due to poor processing of the cross-section sample).

As we have shown that the wetting of the $3\text{LiBH}_4\text{-LiCl}$ is effective with graphite and silicon-carbon composite electrodes, they can be used to make half cells to test the realistic capacity of these electrodes. To make half-cells with lithium, a melt-infiltrated electrode (anode specific) is hot-pressed with a SSE pellet to ensure there is no shorting between the soft lithium and the melt-infiltrated electrode. Since the selected SSE is very stable with lithium metal, proven by CV and symmetric cell testing, there is no requirement for protective layers to protect the lithium from the SSE. An SSE pellet (~ 300 μm thickness) was first hot-pressed together with a melt-infiltrated anode, and a Li metal anode

was then attached to the other side of the SSE pellet. The condition for hot-pressing was 50 °C for 1 h at a pressure of 80 MPa.

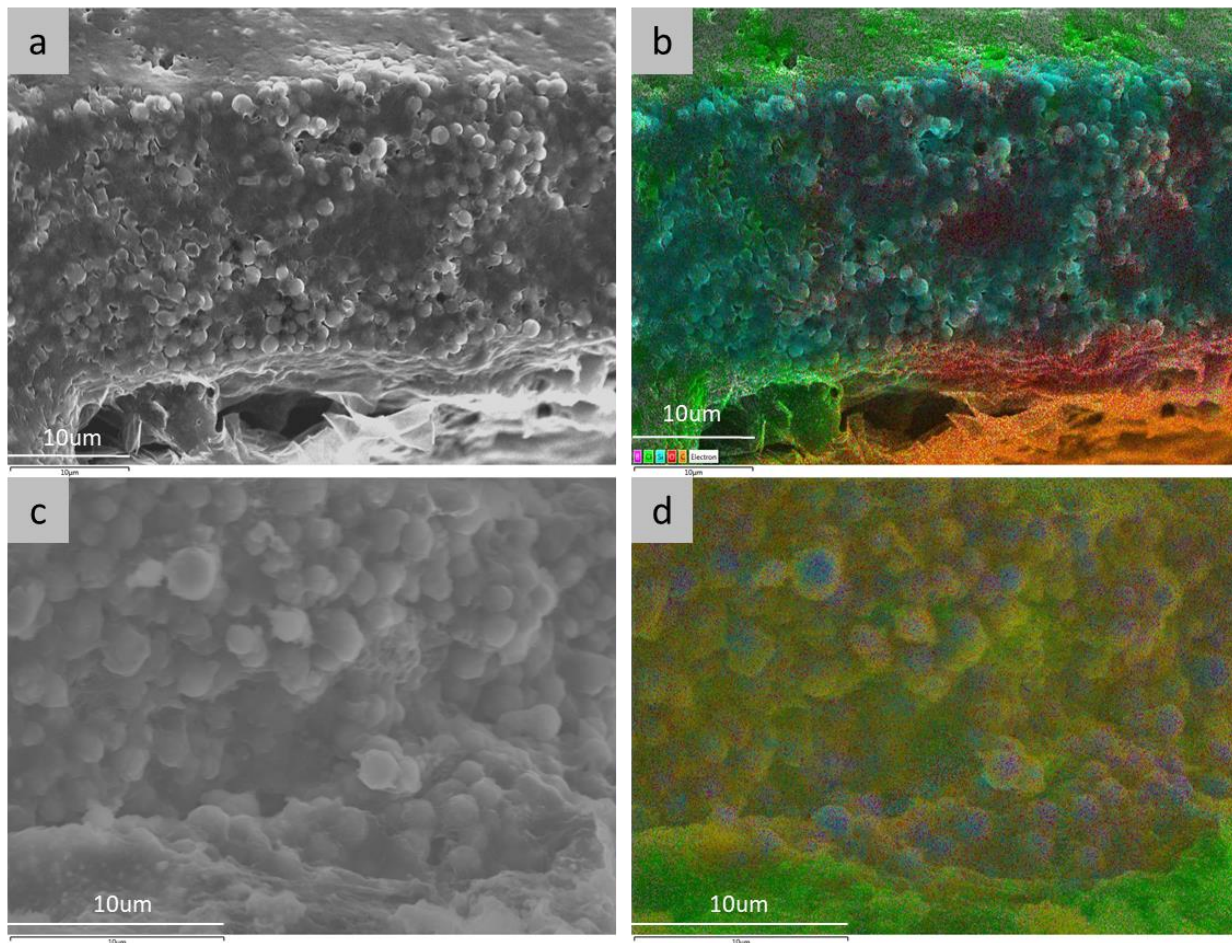


Figure 36. (a) melt-infiltrated silicon-carbon composite electrode with $3\text{LiBH}_4\text{-LiCl}$ electrolyte, (b) an EDS map of the cross section image of the infiltrated silicon-carbon anode. The green, blue, red and orange respectively represent chlorine, silicon, oxygen and carbon. (C) a magnified image of a melt-infiltrated silicon-carbon electrode, (d) a respective EDS map of the electrode using the same color scheme as (b).

Since NMC111 is reactive with $3\text{LiBH}_4\text{-LiCl}$, NMC111 electrodes are infiltrated with Li_2OHCl as down in our previous work.^[122] NMC111 half cells were assembled by hot-pressing a $3\text{LiBH}_4\text{-LiCl}$ SSE pellet a melt-infiltrated cathode, and a Li metal anode was then attached to the other side of the SE pellet. The condition for hot-pressing was 50

°C for 1 h at a pressure of 80 MPa. A schematic shows the assembly of the silicon-carbon composite anode half-cell.

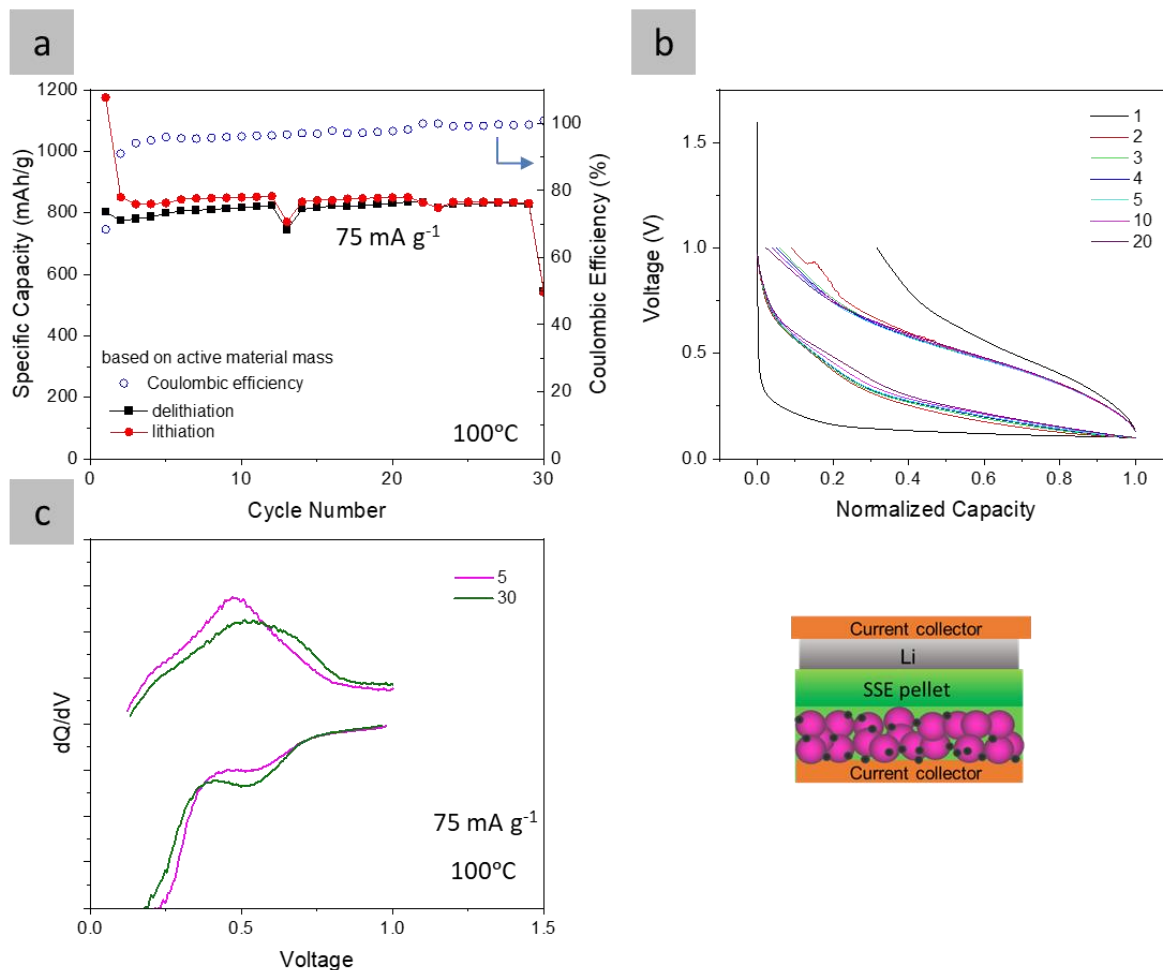


Figure 37. (a) the half-cell performance of the silicon-carbon anodes using the 3LiBH_4 - LiCl SSE which is cycled between 1 to 0.1V (vs Li^+/Li). The cell shows great capacity of around 800 mAh g^{-1} ; (b) the voltage profile of the silicon half-cell with respect to the normalized capacity (c) dQ/dV plot of the half-cell to show lithiation and delithiation of lithium into and out of the electrodes.

The silicon-carbon composite anodes (as shown in figure 37) are cycled between 1 to 0.1V (vs Li^+/Li) at a current rate of 75 mAh g^{-1} ($\sim C/5$). The first two cycles can be considered as formation steps, where the electrolyte is reduced at low voltage to form decomposition products. These decompositions also known as the SEI will prevent any

further reduction of the electrolyte at the surface of the electrodes. We notice the realized capacity for these half cells is around 800 mAh g^{-1} but the experimental capacity measured in liquid electrolyte was actually 1200 mAh g^{-1} .^[37] The capacity is relatively low compared to the liquid cells may be due to high hardness of the SSE, which cannot fully accommodate volume changes in Si-based composites. Since the ionic conductivity of the electrolyte is still not comparable of that of liquid electrolyte, the ohmic resistance of the SSE may also negatively impact the cycling capacity. Though a lot of research has suggest how high amounts of carbon in the electrode could negatively impact electrolyte performance, we notice stable cycling for 30 cycles without any capacity fade.^[61] We also notice that the first cycle CE is relatively low at 75%, which denotes that a lot of lithium is consumed during the formation process. This would negatively impact full cell performance since there would be a significant lithium inventory loss. The dQ/dV plots in figure 37, show the symbolic delithiation and lithiation peaks of the silicon-carbon composites anodes at 0.49V and 0.21V (0.49V), respectively. These plots also show no sign of side reactions since there additional peaks.

The NMC111 cathodes (as shown in figure 38) are cycled between 3 to 4V (vs Li^+/Li) at a current rate of 45 mAh g^{-1} ($\sim C/5$). The first two cycles can be considered as formation steps, where the electrolyte is oxidized at high voltages to form decomposition products. These decompositions also known as the cathode electrolyte interface will prevent any further oxidation of the electrolyte at the surface of the electrodes. We notice the realized capacity for these half cells is around 120 mAh g^{-1} but the experimental capacity noted is actually 160 mAh g^{-1} .^[125] The capacity is relatively low compared to the liquid cells since the polymer binders used in these cathodes are different and it is also

limited by the ionic conductivity of the electrolyte. Since the ionic conductivity of the electrolyte is still not comparable of that of liquid electrolyte, the ohmic resistance of the SSE negatively impacts the cycling capacity. The dQ/dV plots in figure 37, show the symbolic delithiation and lithiation peaks of the NMC111 at 3.8V and 3.7V respectively. These plots also show no sign of side reactions since there additional peaks.

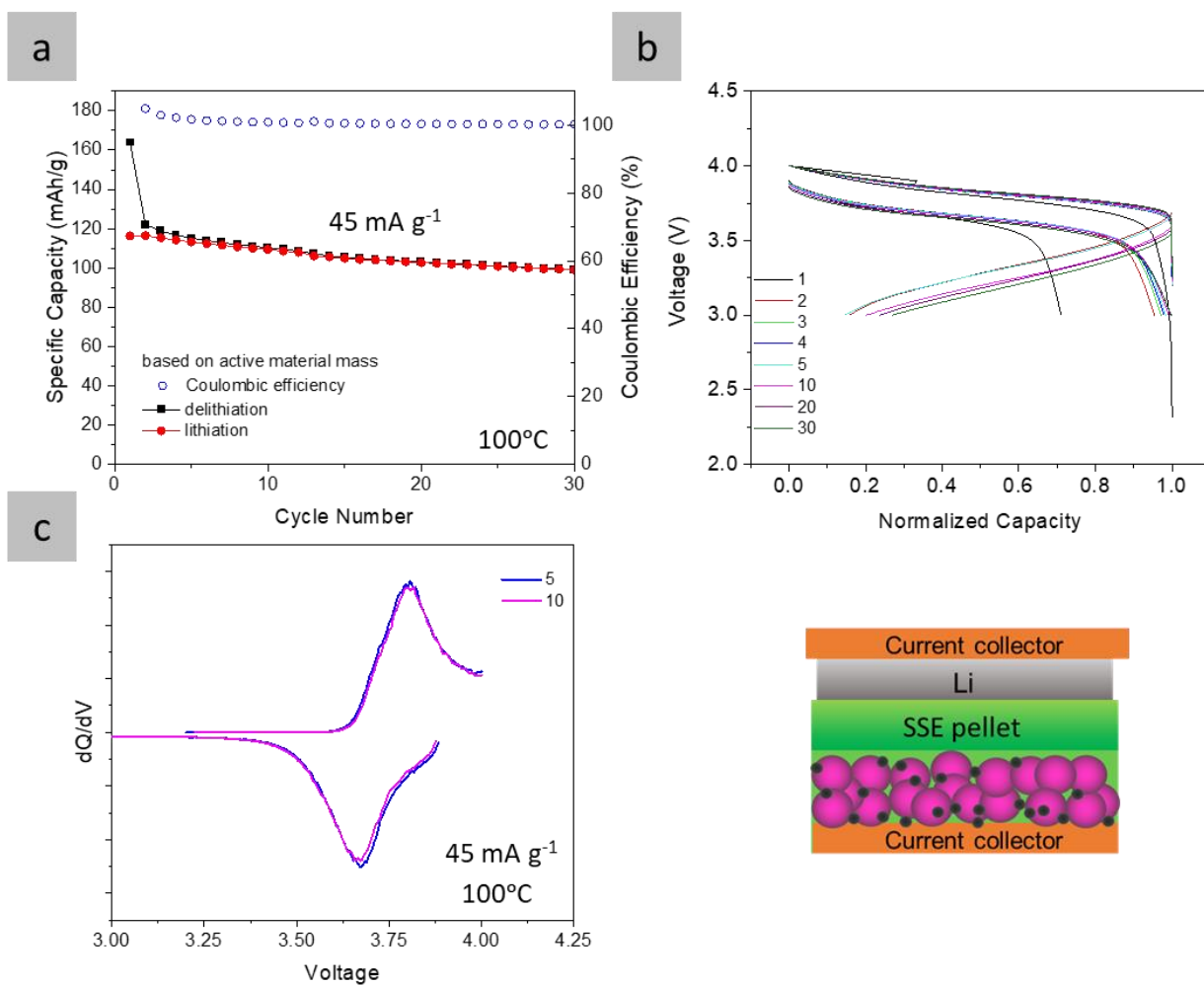


Figure 38. (a) the half-cell performance of the NCM11 cathode infiltrated with Li_2OHCl and using the $3\text{LiBH}_4 - \text{LiCl}$ SSE pellet which is cycled between 3 to 4V (vs Li^+/Li). The cell shows great capacity of around 100 mAh g^{-1} ; (b) the voltage profile of the NCM111 half-cell with respect to the normalized capacity; (c) is dQ/dV plot of the half-cell to show lithiation and delithiation of lithium into and out of the electrodes.

Even though the cathode particles are infiltrated with the Li_2OHCl SSE and a $3\text{LiBH}_4\text{-LiCl}$ separator pellet is used, we don't notice any sort of side reactions between the SSEs from the dQ/dV plots.

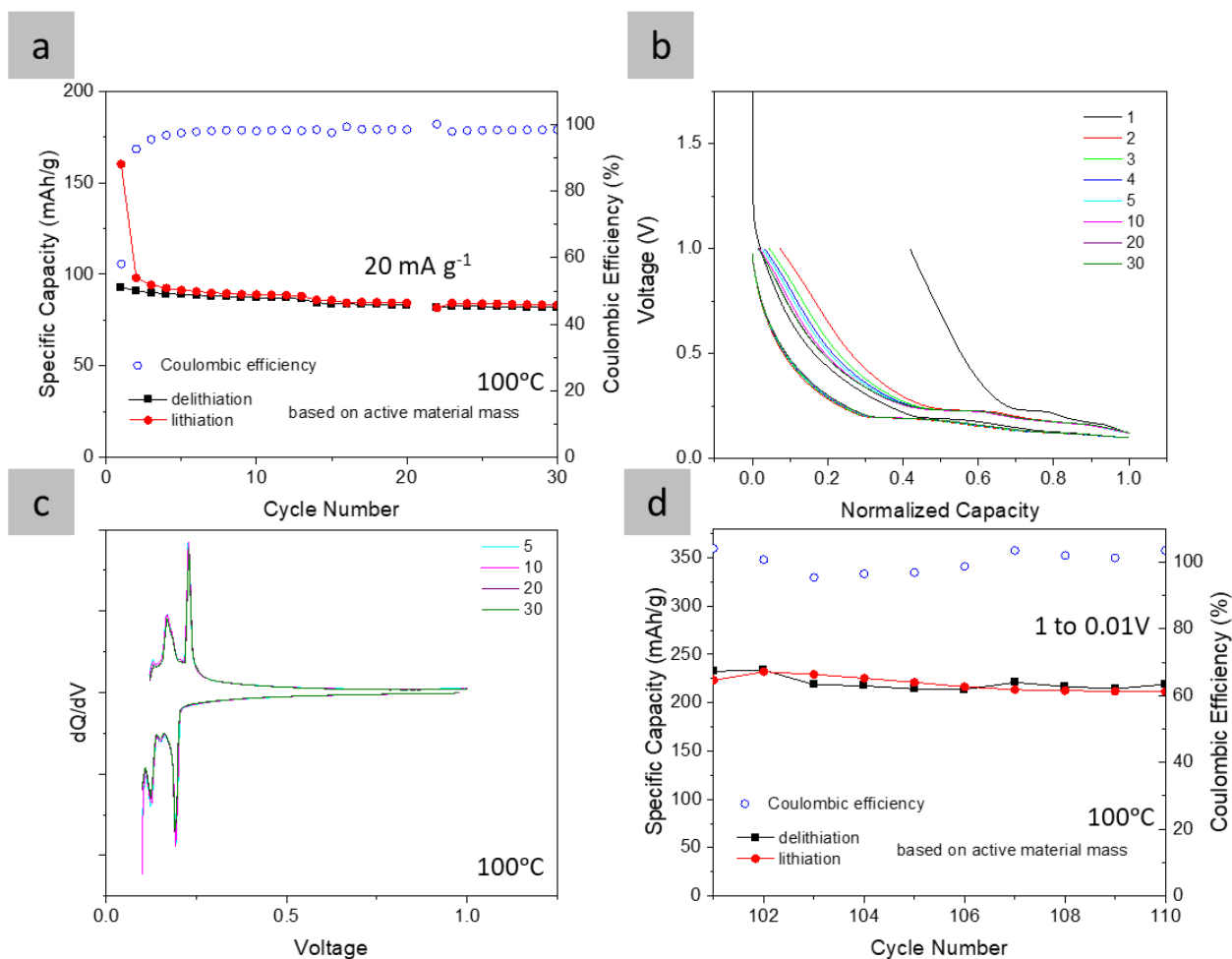


Figure 39. (a) the half-cell performance of the graphite anodes using the $3\text{LiBH}_4\text{-LiCl}$ SSE which is cycled between 1 to 0.1V (vs Li^+/Li). The cell shows great capacity of around 100 mAh g^{-1} ; (b) the voltage profile of the silicon half-cell with respect to the normalized capacity (c) dQ/dV plot of the half-cell to show lithiation and delithiation of lithium into and out of the electrodes and (d) the charge discharge plot for graphite cycled between 1 to 0.01V (vs Li^+/Li).

The graphite anodes (as shown in figure 37) are cycled between 1 to 0.1V (vs Li^+/Li) at a current rate of 20 mAh g^{-1} ($\sim C/10$). Graphite anodes can be cycled all the way

down to 0.01V and we notice that the capacity is then around 250 mAh g⁻¹. The first two cycles can be considered as formation steps, where the electrolyte is reduced at low voltage to form decomposition products. These decompositions also known as the SEI should ideally prevent any further reduction of the electrolyte at the surface of the electrodes. We notice the realized capacity for these half cells is around ~250 mAh g⁻¹ but the experimental capacity in liquid electrolytes may approach 372 mAh g⁻¹.^[126] The capacity is relatively low compared to the liquid cells since the polymer binders used in these anodes are different, it is also limited by the ionic conductivity of the electrolyte and the instability of the solid electrolyte to accommodate the volume changes in graphite upon lithiation. The dQ/dV plots in figure 39, show the symbolic delithiation and lithiation peaks of the silicon-carbon composites anodes at ~0.25V and ~0.21V respectively. These plots also show no sign of side reactions since there additional peaks.

As we have systematically investigated the various half-cells with various active materials, it is important to understand the failure the mechanisms of these half-cells. As we know that inorganic SSEs, especially ceramics, are brittle in nature. They crack and delaminate due to having a very high Young's Modulus (due to which they are rigid and hard). Upon teardown of these cells after cycling, we notice widespread electrolyte cracking and delamination of the particles from the surface of the electrolyte. During repeated lithiation and delithiation of active materials, these materials undergo a cyclic expansion and contraction – which over time applies stresses to the SSE. We see (from Figure 40a and b) notice widespread cracking of the electrolyte surrounding the silicon particles and delamination of the electrolyte. When the electrolyte loses contact with the AM material, the charge transfer and SEI resistance increases. The loss in contact from the

electrolyte surface will lead the quicker capacity fade which is reflected in long term in silicon-carbon composite anode half-cell performance (which will be explained in detailed in the last section with EIS data).

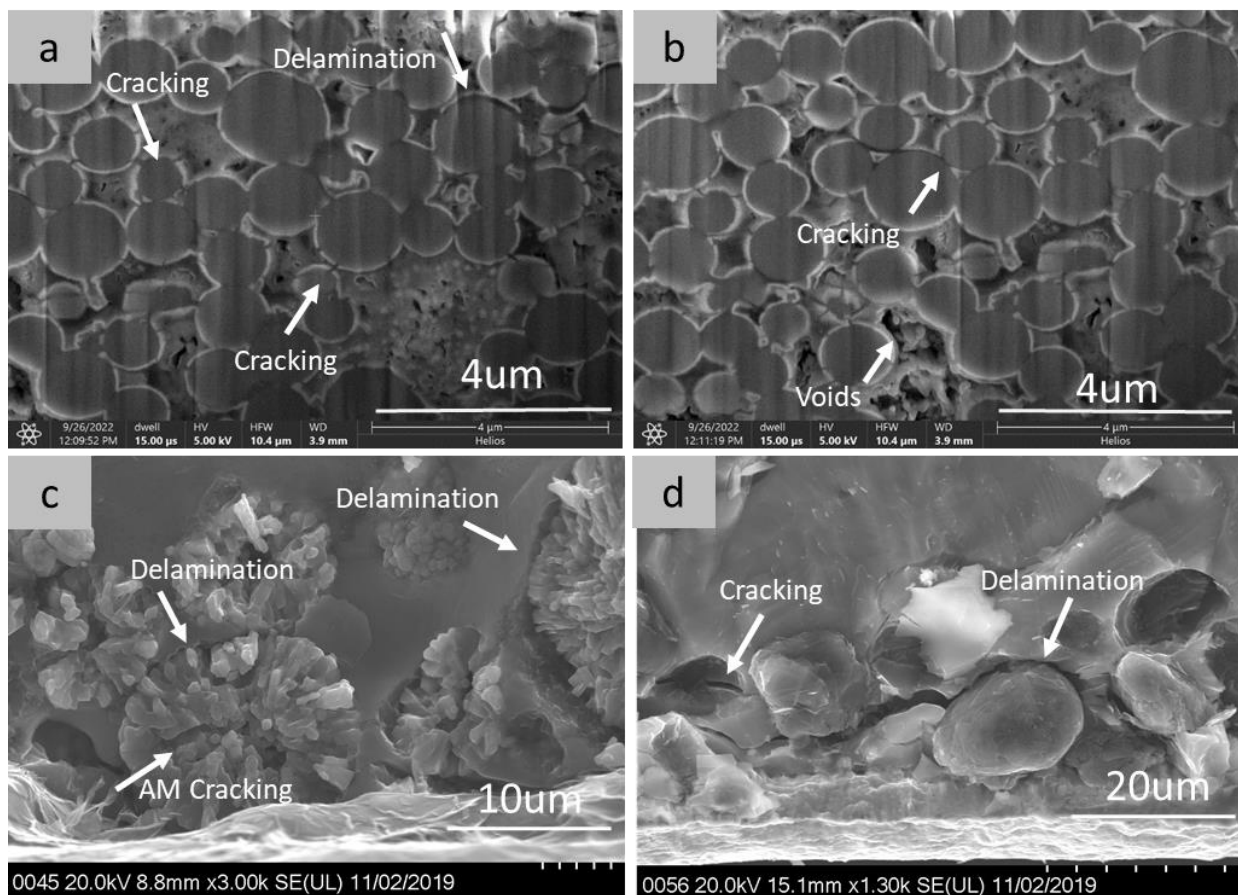


Figure 40. (a) and (b) spherical silicon-carbon composite - based anodes after cycling for 50 cycles at 800 mAh g⁻¹ between 1V to 0.1V (vs. Li⁺/Li); we notice widespread cracking and delamination of the particles from the electrolytes; (c) NCM particles which have delaminated and cracking after cycling at 100 mAh g⁻¹ for 100 cycles and finally; (d) the graphite particles which have delaminated after cycling at 250 mAh g⁻¹ for 50 cycles.

For NMC and graphite we see very similar failure mechanisms compared to that of silicon-carbon composite anodes. For NMC specially, we notice that in addition to delamination from the Li₂OHCl electrolyte, the NMC111 particles tend to crack and

deform during cycling which is a sign of poor NMC quality. Doped version of NMC111 or single crystal versions NMC111, could help NCM111 half-cell performance since AM cracking leads to loss in usable capacity.^[125] Finally graphite half-cells are relatively stable when the capacity is limited to $\sim 150 \text{ mAh g}^{-1}$ since the volumetric expansion of graphite is limited.

Full cells (NCM/SSE/Si-C) (Si-C is a silicon-carbon nanocomposite based anode) were made to further assess the melt-infiltration technology and understand the compatibility of the $3\text{LiBH}_4\text{-LiCl}$ with various electrolyte systems used for cathode infiltration. The voltage ranges for cycling full cells are determined by the operating potentials of the cathode material and the anode materials. The delithiation potential for NCM is $\sim 3.75 \text{ V vs. Li/Li}^+$ (Figure 38) and the lithiation potential for silicon-carbon composites is starting from $\sim 0.21 \text{ V vs. Li/Li}^+$ (Figure 37), so the nominal voltage for NCM/SSE/Si-C cells is $\sim 2.8 \text{ V}$. For NCM/SSE/Si-C full cells, the potential of Li-intercalation into silicon-carbon composites starts from $\sim 0.21 \text{ V vs. Li}$ (Figure 37), so the NCM/SSE/Si-C cells should be able to charge to $\sim 4.1 \text{ V}$ (equivalent to $4.2 \text{ V vs. Li/Li}^+$). However, the cells failed to directly charge to 4.1 V . Most NCM/SSE/Si-C cells could only charge to 4.0 V , but the voltage could be raised to 4.05 V and 4.1 V in the subsequent cycles. This may be explained by the decomposition of the SSE and the formation of a SEI layer at the SSE – silicon-carbon composites or SEI - graphite interface during the first charging process. This process is analogous to the formation of SEI layer on the silicon-carbon composite or graphite anode in a conventional LIB cell in its first charge. For an NCM/SSE/Si-C cell (NCM mass loading: 1 mg) cycled at $100 \text{ }^\circ\text{C}$ and in the voltage range of $3\text{-}4 \text{ V}$, the initial NCM capacity of $\sim 120 \text{ mAh g}^{-1}$ at 30 mA g^{-1} decreases to $\sim 75 \text{ mAh g}^{-1}$

¹ at 100 cycles, as shown in figure 41b. At the current of 10 mA g⁻¹, another NCM/SSE/Si@C cell (NCM mass loading: 3 mg) delivers an initial capacity of ~145 mAh g⁻¹ (Figure 41C) with a capacity retention of over 50% after 100 cycles. The voltage hysteresis does not significantly change after 100 cycles (Figure 41D).

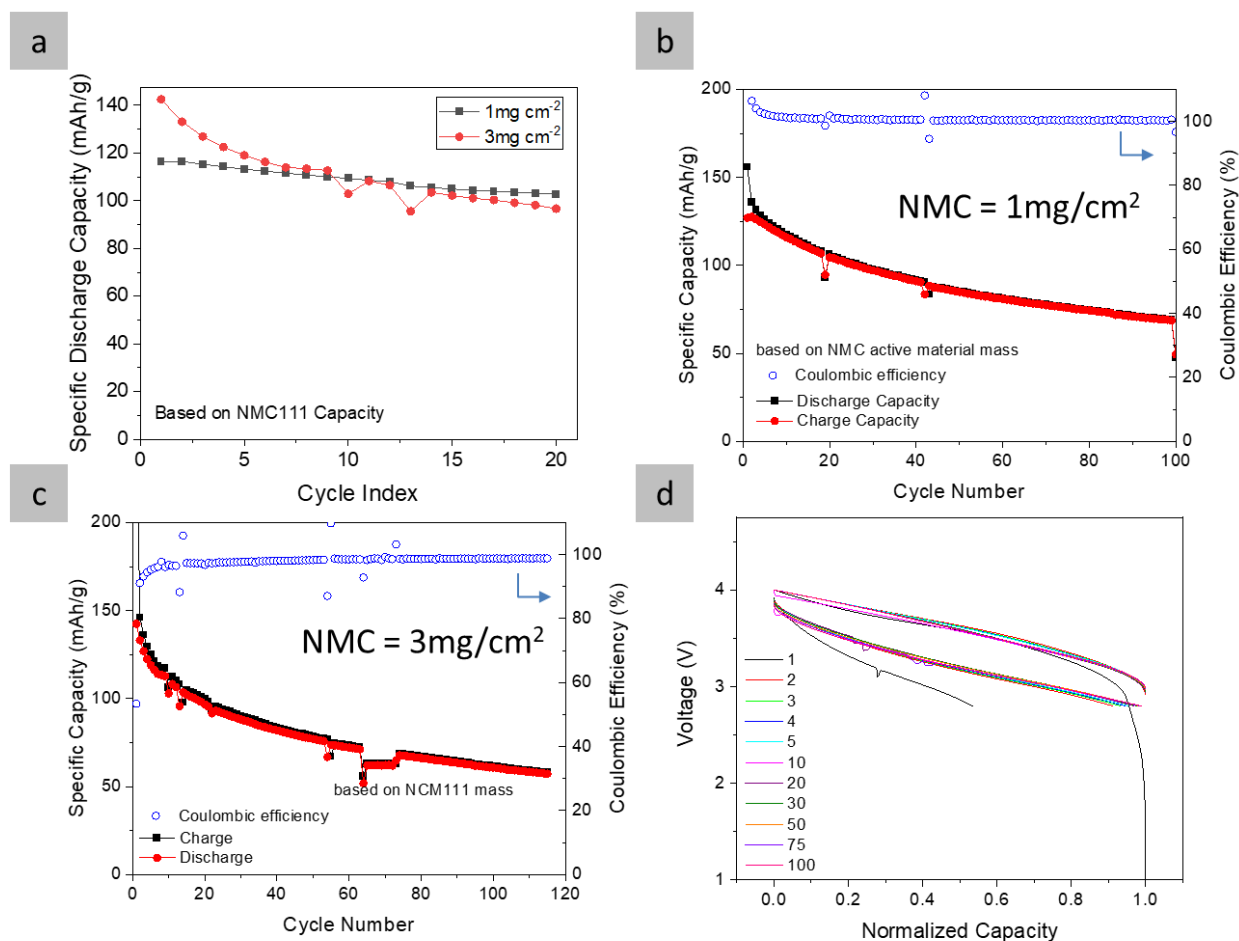


Figure 41. (a) comparison of initial discharge capacity of varying mass loading of NMC111; (b) the long-term cycling of NMC111 with a mass loading of 1 mg cm⁻²; (c) is a long term cycling plot of a higher mass loading full cell; (d) voltage vs normalized capacity curve to study the hysteresis of the cell.

The capacity retention over 100 cycles of the full cells is well below 80%, which is considered to be benchmark performance metric for full cell performance. However, these

full cells don't use high pressure to constrain and hinder delamination and SSE cracking which has been commonly used in past work. Though the voltage hysteresis of the full cells is very low, which points out that there is no change in the overpotential and resistance in the cell, the capacity fade is still very aggressive. The capacity fade for both half cells and full cells can be studied using EIS and post cycling SEM. As we have seen cracking in AM particles and delamination, we expect the charge transfer resistance and the SEI resistance in the cell to increase. During the expansion and contraction, we hypothesize that the SEI would crack and the particle would subsequently be exposed to new SSE, forming new SEI again. As this phenomenon happens occurs multiple cycles, we would expect the growth of a thick SEI layer. Thick SEI layers will lead to capacity fade during cycling.^[127, 128] In addition to the formation of a thick SEI layer, delamination of the SSE from the AM particle will lead to increase in the resistance (charge transfer resistance), which also leads to capacity fade. To investigate this hypothesis we studied the EIS of both half cells and full cells at different cycle times.

EIS data was collected at various stages of cycling for the silicon-carbon composites half-cell, and we notice an overall increase in the resistance over cycling time. The impedance before cycling is higher than the impedance after the formation step, which is due to the formation of a conductive SEI layer. The interface before SEI formation is not conducive for lithium-ion conduction and hence we notice an increase in the resistance. There is a major difference between the impedance at cycle 2 (after the formation of a conductive SEI) and cycle 100 due to the SSE cracking and delamination from the AM. The impedance semicircle (single semi-circle and then Warburg diffusion) at the initial cycles can be de-convoluted into R_{SEI} and R_{CT} . But we notice that, at cycle 100, we see two

distinct semicircles: R_{SEI} (high to mid frequency range) and R_{CT} (Mid to low frequency range). There is a drastic increase in the R_{CT} due to cracking and delamination as seen in figure 40(a) and (b), which as a result reduces the number of active sites available for the redox reaction to take place.

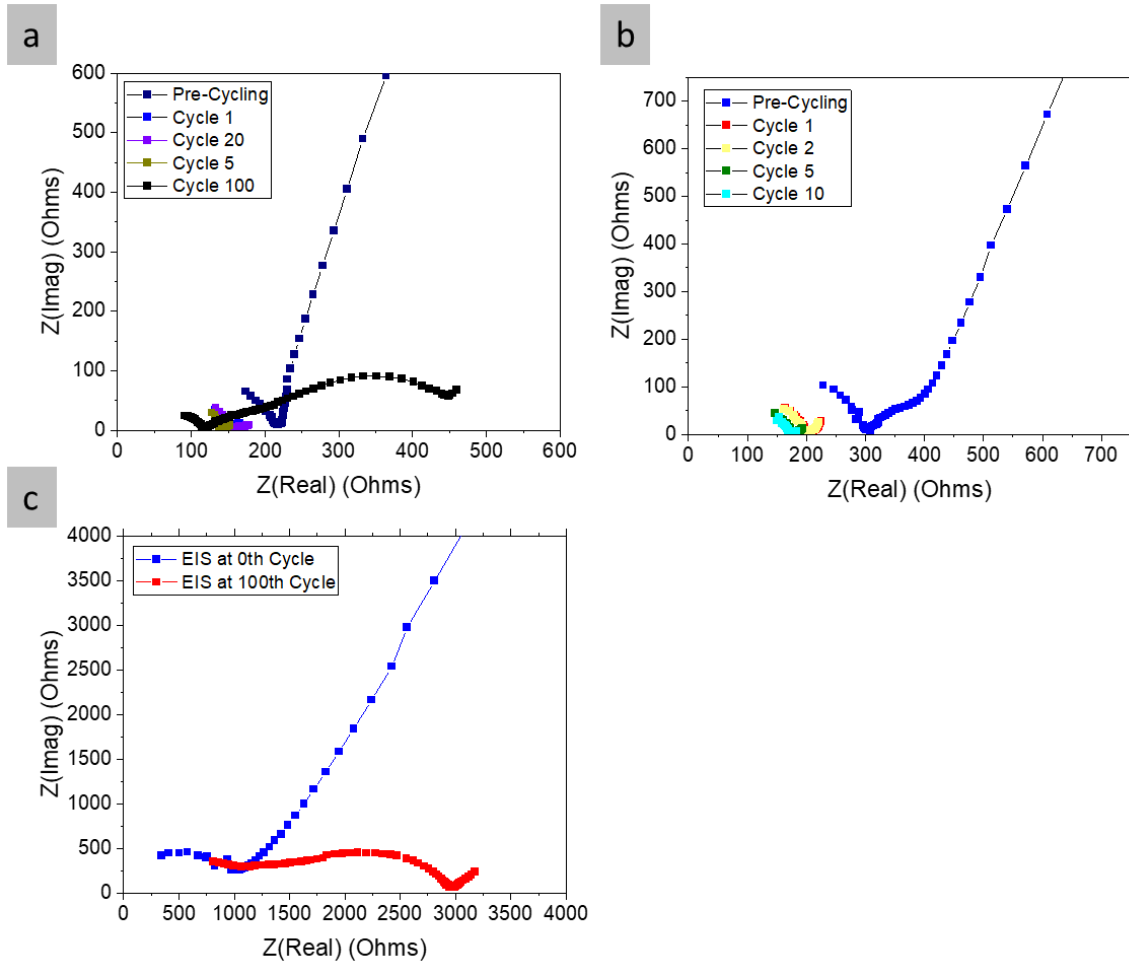


Figure 42. (a) EIS curves for a Si half-cell at various cycling times; (b) is the EIS curves for the graphite half-cell at various cycling times; (c) EIS curves for the NMC/SSE/Si-C nanocomposite before and after cycling.

We see a very familiar trend with both graphite half cells and full cells with NMC111 and the silicon-carbon nanocomposite. The results indicate that cycling-induced

stresses at the SSE/active material interfaces are a key failure mechanism that controlled overall cell cycling performance in melt-infiltration produced.

3.4 Conclusions

In this chapter, we have successfully able to show and prove the synthesis of the borohydride-based SSEs using a melt-synthesis and used advanced characterization methods to systematically investigate the SSEs made. We were able to mechanistically understand the difference between the doping of borohydride with various salts and with varying LiCl concentration. In addition to understand how fundamental crystal properties changed with respect to varying halide salts and LiCl concentration, we systematically investigated how these effected the phase transition temperature and the ionic conductivity. Since $3\text{LiBH}_4\text{-LiCl}$ and LiI showed the most promising performance, we study fundamental electrochemical properties, such as CV, EIS and Li-symmetric cell testing, of these selected SEs. The melting point of $300\text{ }^\circ\text{C}$ made $3\text{LiBH}_4\text{-LiCl}$ a good choice for the proof-of-concept demonstration and exploration of the proposed melt-infiltration method.

We then study the performance of the SSE with various active materials such as silicon-carbon composite, and graphite anodes and NMC111 cathode using melt-infiltration as the method of fabrication. Though the electrochemical performance of the cells were limited by the moderate conductivity of the SSE. SSE full cells with silicon-carbon composites anodes generally showed undesirably faster degradation, which may be expected from previous work and their liquid electrolyte analogs. EIS data taken before and after cycling suggested the formation and growth of resistive interfacial layers at the SSE/electrode interfaces. A drastic increase impedance component was observed in the

NCM/SSE/Si-C cells after 100 cycles. This observation found a correlation to the formation of cracks in the electrodes, separation of active material particles and the delamination of active materials from the SSE and current collectors in the post-mortem SEM images.

CHAPTER 4. A NANODIAMOND-ENHANCED NANOFIBER SEPARATOR FOR HIGH-ENERGY LITHIUM-ION BATTERIES

The following is reproduced and reformatted from the author's manuscript which has been submitted and accepted by the journal: ACS Applied Materials and Interfaces. The publication will be entitled: "A Nanodiamond-Enhanced Nanofiber Separator for High-Energy Lithium-Ion Batteries" and its authors include Aashray Narla, Wenbin Fu, Alp Kulaksizoglu, Atsushi Kume, Billy R. Johnson, Ashwin Sankara Raman, Fujia Wang, Alexandre Magasinski, Doyoub Kim, Mohammed Kousa, Yiran Xiao, Samik Jhulki, Kostiantyn Turcheniuk, Gleb Yushin.^[129] The primary differences between the manuscript and this chapter are the inclusion of the supplemental information into the main text as well.

4.1 Introduction and Background

With climate change being an overhanging concern, there is a growing need for environmentally friendly renewable energy sources (such as solar and wind) as well as efficient energy storage devices to store renewable energy.^[130] LIBs are ideal energy storage devices due to their high energy and power density, efficiency, long cycle life and low self-discharge.^[131] The demand for LIBs is further fueled by the automotive industry and the growing usage of portable electronics.^[132] Over the past decade, extensive research has shown pathways for improving energy density of LIBs by incorporating high-voltage cathodes, conversion-type electrodes, and solid-state electrolytes, silicon or Li metal anode since higher energy density directly relates to longer mileages for EVs and usage times for

portable electronics respectively.^[31, 133-135] Despite the rapid advances in LIBs/LMBs with high energy density over the past few years, many safety concerns still remain, which could hinder their wide-scale adoption in everyday use. Separators are an inactive component in batteries, which do not directly participate in the redox reactions but physically separates battery anode and cathode, prevent short circuits and serve as reservoirs of liquid electrolytes and as conduits for Li-ion transport between the electrodes.^[136] In general, separators play a recognizable role in determining battery rate capability, lifespan and perhaps most importantly, safety.^[137-139]

Conventional separators are made from thermoplastic polyolefins such as polyethylene (PE) and polypropylene (PP), and they can be produced at large scale by wet processing but they tend to suffer from low porosity, poor thermal stability (excessive shrinking at elevated temperatures), and high tortuosity, which are likely to cause premature failures of high-energy density cells.^[140, 141] To illustrate, as LIBs are cycles for extended periods of time, heat-triggered exothermic “thermal runaway” reactions occur due to large variety of reasons in the cells. Side reactions or high overpotentials lead to an overall increase of temperature in the cell, which caused the separator to shrink, the SEI to break down, and eventually short-circuit, resulting in explosions and fires in some (fortunately rare) cases, a relatively common shortcoming in PE and PP separators.^[132, 142] A separator that minimizes the overpotentials (has low impedance) in the first place through a facile conduction of Li-ions, and that is aided with tools (i.e., thermally stable, and able to prevent shrinkage at high temperatures) to dissipate heat in the case of a thermal runaway, is required to reduce the probability of short circuiting, improve cycle life, and ensure safety.^[143-145] Moreover, a thin, porous, and ionically conductive separator is

required for the next-generation LIBs to garner the benefits of high-energy dense electrodes. Polymer-nanoparticle composites have been of growing interest for the past two decades as candidates for separators in high-energy density LIBs. Nanoparticles, inorganic or organic, when embedded in the polymer matrix tend to improve mechanical, thermal and structural properties of the polymer-composite.^[146] With widespread availability of nanostructured and nano-sized particles such as carbon nanotubes, inorganics nanowires, inorganic nanospheres and graphene with tunable size and surface functionalization, there have been significant efforts to improve appropriate properties of the composite for their use as separators in high-energy-density LIBs and LMBs.^[147-149] Yet, drawbacks such as poor cycle life, large overpotentials, and complicated processing methods still remain, which call for further innovation in their chemistry and engineering aspects.

NDs are a relatively unexplored class of carbon nanoparticles, which are considered 0-dimension particles, featuring high surface-to-volume ratio, tunable size and surface functionalization, high elasticity moduli, and exceptional thermal conductivity.^[150-152] They have been explored towards diverse applications such as biomedical fields, supercapacitors and batteries.^[153-156] Based on past work, spraying NDs on a commercial separator can provide favorable electrolyte affinity for regulating Li⁺ distribution, high Young's modulus against Li dendrite growth and excellent thermal diffusion ability.^[156] Recent studies also revealed that NDs can be used as an additive to liquid electrolytes to plate lithium uniformly and hinder dendrite growth, and ND thin film can provide interfacial protection for Li metal anode.^[156-158] Considering these unique properties of NDs, in this work we developed a functionalized composite separator based on NDs incorporated with poly(vinylidene fluoride-co-hexafluoropropylene) (PVDF-HFP)

nanofibers, characterize their thermal, mechanical, and morphological properties, which all deemed suitable for use in high-energy dense LIBs. Then we explored the electrochemical properties of these separators in LIBs using high-voltage $\text{LiNi}_{0.8}\text{Mn}_{0.1}\text{Co}_{0.1}\text{O}_2$ (NMC811) as the cathode. We report excellent performance of these separators in these cells, especially when compared to standard PP separators. This study reintroduces NDs for composite membrane fabrications, opening up a wide variety of possibilities for its future use.

4.2 Experimental Section

4.2.1 Preparation of ND-functionalized membranes

ND dispersions (1 wt.%) were prepared by mixing 0.017 g of ND-Si-PPG (Daicel Corporation), 2.41 g of N, N-dimethylacetamide (DMAc, Sigma-Aldrich, purity $\geq 99.5\%$), and 6.52 g of acetone (Sigma-Aldrich; purity $\geq 99.8\%$). The 5 wt% ND dispersions were prepared by mixing 0.11 g of ND-Si-PPG, 2.41 g of DMAc, and 6.52 g of acetone. The dispersions were stirred for 30 min at a speed of 300 rpm, and to each solution was added 1.64 g of PVDF-HFP (Sigma-Aldrich avg. Mw $\sim 455,000$). The subsequent mixtures were stirred at 50 °C for 24 h to achieve a homogeneous and viscous gel. The mixed gel was tip-sonicated (Misonix S-4000 at 1W) for 1 min before electrospinning to further improve the dispersion. Electrospinning was conducted using 3 mL of dispersion for each sample in a syringe and then secured onto a syringe pump to extrude the slurry at a rate of 0.5 mL/h with a rotating drum at 150 rpm. The distance and accelerating voltage between the syringe's tip and the rotating drum were 16 cm and 16 kV. After electrospinning, the subsequent membrane was separated from the aluminum sheet, folded in half, and hot

pressed at 110 °C for 2 h under a pressure of 30 MPa using press (Across International, Swingpress) to decrease the porosity. The membranes were then dried for 24 h at 80 °C for subsequent studies.

4.2.2 *Materials characterizations*

The Hitachi SU8230 was used to take images of the polymer membrane structure after electrospinning. Single polymer composite fibers and ND plane distance was determined by using a TEM (Tecnai G2 F30 TEM). TGA was done using a TA instrument TGA (TA Q600), where the heat was ramped up from room temperature to 400 °C at 5 °C/min. DSC (TA instruments Q200) was used to figure out the % of crystallinity of the samples with respect to the ND concentration. The temperature of the samples was ramped from room temperature to 160 °C and cooled back to room temperature at 10 °C/min. The DSC test was run 4 times to ensure consistent results between cycles. XRD was performed on the Panalytical XPert PRO Alpha-1 XRD instrument by placing the samples on a zero-background holder.

To study and investigate stress/strain behaviour of the separators, tensile tests were performed following ASTM D882 Standards using a 25 N force gauge on a Mark-10 ESM303 test stand. Gurley values were obtained by measuring the time taken for 100 mL of air to pass through a fixed area (19.6 cm²) under a pressure of 0.02 MPa using a Gurley Precision Instrument (TROY). The porosity of separators was determined by the absorption experiment of n-butanol for 10 h, as reported by previous studies and calculated based on the equation (18):^[154, 159]

$$\text{Porosity (\%)} = (m_1/\rho_1)/(m_1/\rho_1 + m_2/\rho_2) \times 100\% \quad 18$$

where m_1 and m_2 are the weights of pristine and n-butanol-saturated separators and ρ_1 and ρ_2 are the densities of the separator polymer and n-butanol, respectively. The surface wettability of separators was investigated by using a static contact angle measurements on a drop shape Model 250 goniometer (USA) with a drop of electrolyte solution onto the surface of separator membranes. Different membranes with the same gurley value was used to ensure, wetting values are purely dependent on material properties and synthesis methodology. The electrolyte solution is 1 M LiPF_6 dissolving in ethylene carbonate (EC) and diethyl carbonate (DEC) (50:50 v/v %). To calculate the electrolyte uptake, the separators were soaked in the electrolyte solution for 2 h and measure the weight before (M_0) and after (M_1) electrolyte absorption based on the equation (19):

$$Uptake (\%) = ((M_1 - M_0)/M_0) \times 100 \% \quad 19$$

The sample preparation for the pulsed-field gradient (PFG) NMR experiment is very similar to that reported previously.^[160] Polymer composites were thoroughly dried at 80 °C for 24 h in a vacuum oven. Then, the polymer composites were stacked together into a 4 mm disc and loaded into a 5 mm diameter NMR probe. The 1M LiPF_6 - EC/DEC (50/50 v/v %) solution was dropped into the NMR tube to completely soak the membranes. The Bruker AVIIIHD-500 NMR instrument was used to measure diffusion coefficients for different nuclei (D_{Li} , D_{H} and D_{F}) at 25 and 40 °C. Pulsed-field gradient spin-echo NMR technique was used to probe the nuclear species: ^7Li at 116.8 MHz, ^{19}F at 282.7 MHz, and ^1H at 300.5 MHz.

4.2.3 Cell assembly and electrochemical tests

In an argon environment inside a glovebox ($\text{H}_2\text{O} < 0.1$ ppm), 2032-type coin cells were assembled using a commercial NMC811 electrode (mass loading, ~ 10 mg/cm² secured from NEI Corp.) as cathode, dried membrane as the separator, Li metal as the reference/counter electrode, and 70 μ L of 1M LiPF₆ in EC/DEC (1:1, v/v%) as the electrolyte. CV was performed using a Gamry Potentiostat at cycling rate 0.1 mV s⁻¹ with a step size of 1 mV. The electrochemical stability of separators was evaluated by using liner sweep voltammetry (LSV) for a coin cell of Li//separator//SS from 3 to 6.5 V (vs Li/Li⁺) at a scan rate of 10 mV s⁻¹ on a Gamry Potentiostat. The cycling stabilities of the membranes were tested at different C-rate (1C = 190 mAh g⁻¹) using an Arbin system. To calculate ionic conductivity, EIS was performed in the frequency range of 1 MHz – 0.1 Hz at room temperature.

4.3 Results and discussion

NDs-functionalized nanofiber membranes can be produced by electrospinning, as shown in the illustration in figure 43(a). The NDs were produced by Daicel Corp.- were surface-functionalized using ball milling of polypropylene glycol (PPG) and silane coupling agent (ND-Si-PPG-CH₃) and then dispersed in *N,N*-dimethylacetamide (DMAc) to form a homogeneous dispersion (NDs were surface functionalized to ensure minimum agglomeration between the nanoparticles). To prepare the polymer solution for electrospinning, PVDF-HFP and NDs in a mixed solvent was prepared by dissolving PVDF-HFP into a mixture of DMAc and acetone. In this process, we used tip ultrasonication to improve the homogeneity of ND distribution in the polymer matrix in

the solution phase. The resulting ND/PVDF-HFP/DMAc mixed solution was electrospun onto an aluminum foil using a high voltage field (16 kV) to form a free-standing, non-woven membrane of PVDF-HFP nanofibers intercalated with NDs. The membrane was then dried and hot pressed for future tests and use. For comparison, we produced membranes with ND mass fractions of 0%, 1% and 5% (ND by weight relative to the polymer), which were denoted as PVDF-HFP, PVDF-HFP@1%ND and PVDF-HFP@5%ND. Generally, commercial separators made from thermoplastic polyolefins such as PP or PE could suffer from low porosity, low heat resistance and slow ionic transport, leading to low-rate capability, and capacity degradation due to the sharp dendrite formation that may destroy cathode particles in the vicinity, as illustrated in figure 43(b). In contrast to these separators, ND functionalized nanofiber membranes could overcome these difficulties, because the nanofiber network offers a higher porosity and faster ion diffusion, which could facilitate electrolyte uptake and Li transport. NDs could guide the uniform plating/stripping of Li on the Li anode surface, without the formation of sharp dendrites. Besides, the hardness and thermal stability of NDs can also improve mechanical stability and thermal stability that allows cells to operate within a wider temperature range.

Figure 43(a) shows photos of produced PVDF-HFP membrane, ND-functionalized membrane and commercial (Celgard 2400) PP separator (cut into a similar size for comparison). The uniform color and contrast indicates a homogenous distribution of NDs within the membranes. XRD (as shown in Figure 44(b)) patterns of the ND-functionalized samples (both 1 and 5 wt. %) are similar to that of the pure PVDF-HFP, suggesting that ND incorporation did not change the packing of polymer significantly in the solid state.

However, it is noted that the employed ND concentration was too low to observe their characteristic diffraction peaks.

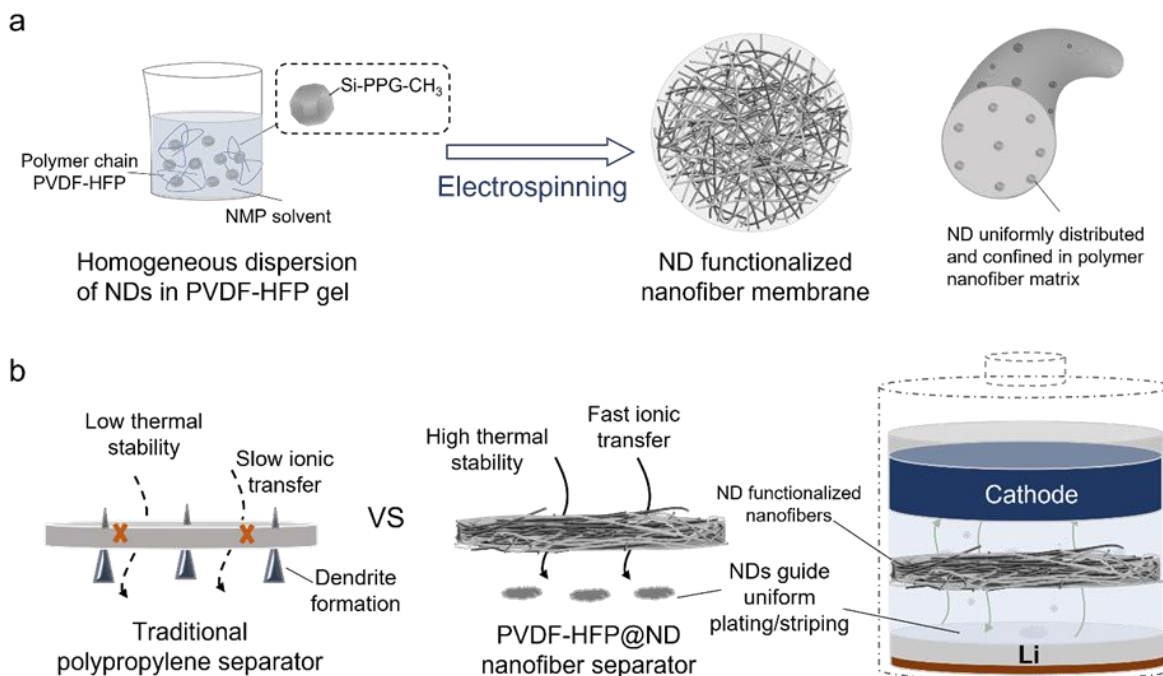


Figure 43. (a) Schematic of the synthesis of ND functionalized nanofiber separator and (b) its advantages over traditional polypropylene separator in Li batteries.

To further identify their chemical bonding features in the membranes, we performed Fourier transform infrared spectroscopy (FT-IR, Figure 44(c)). In the FT-IR spectra of PVDF-HFP (0 wt.% ND) and the composites with 1 and 5 wt.% NDs, the bands for -CF stretching (1400 cm^{-1}), anti-symmetric -CF_2 stretching (1172 cm^{-1}), CF_3 out-of-plane stretching/bending (1072 cm^{-1}), and the characteristic bands at 838, 871 and 1168 cm^{-1} due to γ phase crystalline structure of PVDF-HFP are observed. The obtained FT-IR spectra are essentially identical to that of pure PVDF-HFP, suggesting non-destructive nature of the membrane fabrication process. After hot press, we find three stretching positions at 613, 761, 795 and 974 cm^{-1} corresponding to the α phase of PVDF. This could

indicate a phase transition between γ to α after hot press as well as the impact from acetone as a co-solvent, as observed in previous study.

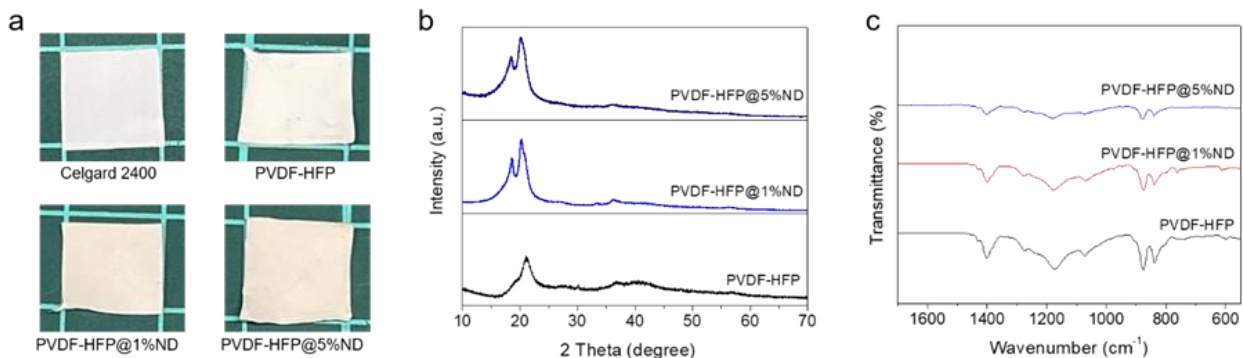


Figure 44. (a) Photo of produced membranes containing 0 wt%, 1% and 5 wt% NDs; (b) FTIR and (b) XRD profiles of the pristine polymer and composite polymers.

SEM shows that non-woven, porous membranes composed of uniform fibers with a diameter of ca. 0.5 μm were produced (as shown in figure 45a and d), but NDs could not be detected. To better observe the NDs and their distribution in the fibers, we performed transmission electron microscopy (TEM). The TEM images show that individual NDs are relatively uniformly dispersed in patches and there are also domains of agglomerated NDs as well along the polymer matrix (figures 45b, 45e). It is well known that both the chemical nature and ND surface (e.g., their surface functional groups) and their concentration in the initial dispersion play important roles in their agglomeration during polymer-ND composite fabrication^[161]. Our fabrication process resulted in NDs/their clusters with diameters in the range of 7–40 nm, which can be confirmed through high-resolution TEM (Figure 2c and f). The crystalline regions are present in polymer fiber represented by parallel patterns and the distance between the parallel lines were calculated to be ~ 0.204 nm which is similar to the interplanar distance of that of NDs.^[162, 163] Forming a composite where NDs are not agglomerated is challenging and requires use of energy-intensive

methods. Our results suggest a homogeneous dispersion of NDs in polymer matrix can be achieved through the surface functionalization of NDs, sonication mixing and electrospinning process. As such, the ND dispersion enable the impartments in the thermal, mechanical, and electrochemical properties for the polymer.

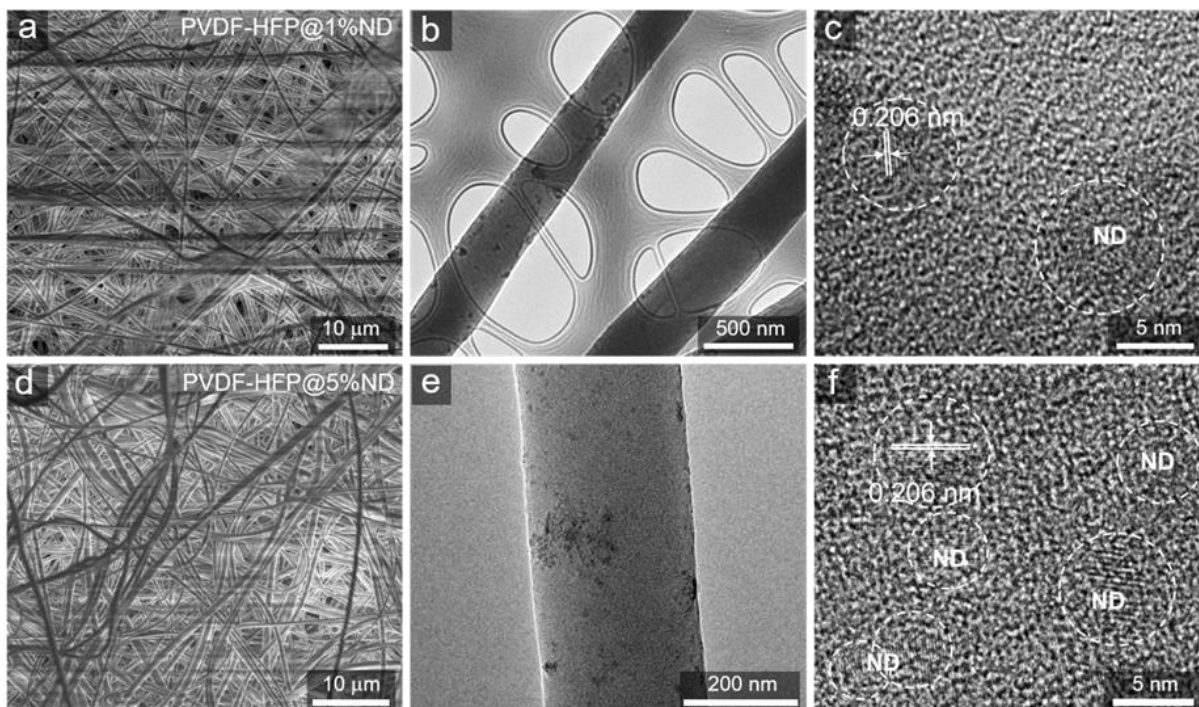


Figure 45. (a) SEM and (b-c) TEM images of PVDF-HFP@1%ND. (d) SEM and (e-f) TEM images of PVDF-HFP@5%ND.

To explore the thermal stability, we heated different membranes from 50 °C to 175 °C, kept them at each temperature for 20 min and checked their thermal shrinkage. As can be seen in figure 46(a), both Celgard 2400 PP and pure PVDF-HFP exhibit rather poor dimensional stability, and their shrinkages start at as low as 125 and 75 °C, respectively. Adding NDs can significantly improve the thermal properties, with the onset of shrinkage being approximately 100 °C. It is noted that the PVDF-HFP@5%ND membrane shows much better thermal stability than PVDF-HFP@1% ND. Thermogravimetric analysis

(TGA) and differential scanning calorimetry (DSC) were employed to investigate the thermal properties of produced membranes. The DSC results reveal that these membrane materials are stable up to 150 °C, irrespective of the ND concentrations in the sample (figure 46b). The decomposition temperatures (T_{ds}) of both samples are much higher than that of a standard PP separator (130 °C), suggesting a higher heat tolerance of these membranes during processing as well as inside the electrochemical cells. DSC data reveals that increasing the ND concentration in the composite membrane results in higher melting point (T_m) for the polymer (figure 46b). Indeed, the 5 wt.% ND-containing separators exhibit the highest T_m of 156 °C and are dimensionally stable at 130 °C for long periods of time (Figure 3c). This was seen by heating polymer membrane at 130 °C for 10 days and the area was calculated during regular intervals. It is noted that the membrane with 5 wt.% ND has a significantly enhanced dimensional stability without a virtually shrinkage at 125 °C. In contrast, commercial PP separators cannot survive high temperatures and they start a shrinkage at about 120 °C. This clearly suggests that the developed 5 wt.% ND-PVDF-HFP composite membranes could serve as a better alternative to the PP separator for long-term LIB cycling, as they are likely to eliminate cell failures due to short circuits caused by thermal shrinkage of the separators at elevated temperatures. Furthermore, the enhanced T_m and T_m due to ND incorporation allows flexibility in thermal processing; for example, drying of these membranes to remove volatiles can be performed at high temperatures. As the thermal and mechanical properties of PVDF-HFP@5% ND were superior compared to those made with either PVDF-HFP@1% ND or pure PVDF-HFP, the former membranes were used for further electrochemical tests.

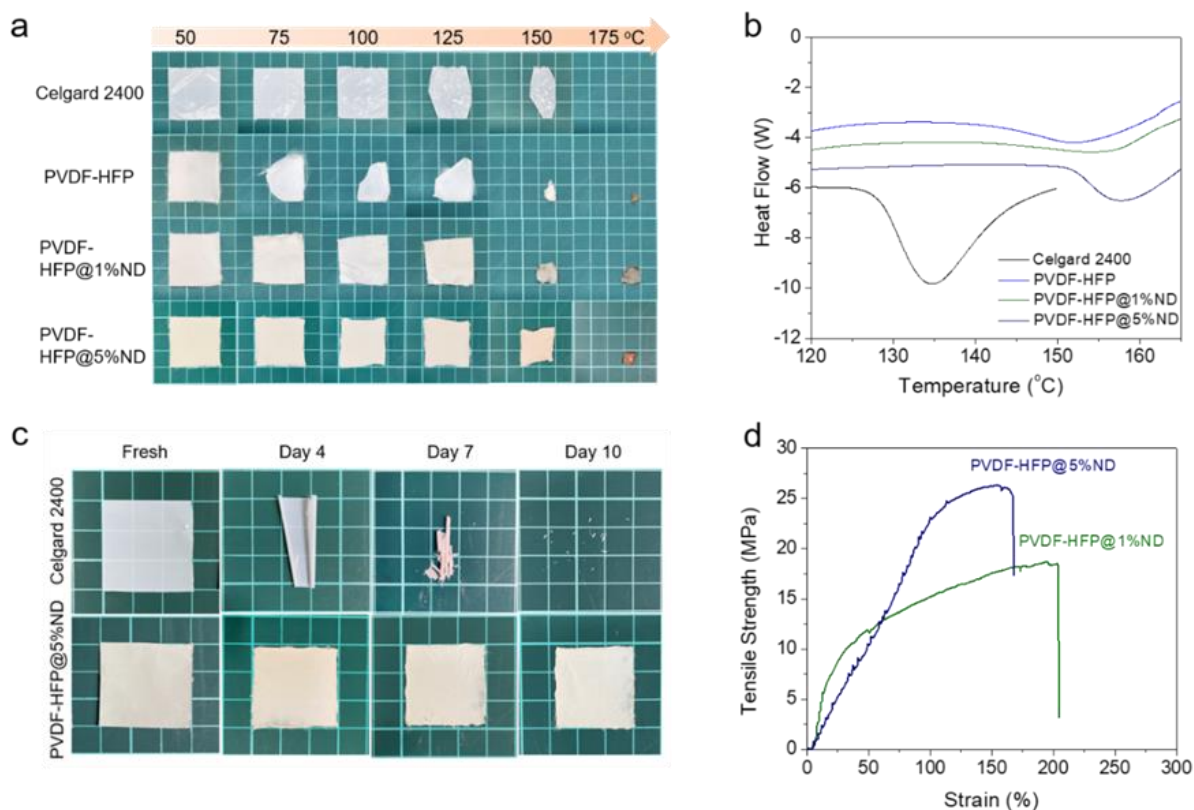


Figure 46. (a) Thermal stability of different membranes at temperatures from 50 to 175 °C (kept 20 min at each temperature); (b) DSC curves of different samples; (c) a shape-retention study of PVDF-HFP@5%ND and PP membranes (~area of 9 cm²) at 130 °C for up to 10 days; (d) strength-strain plots of ND-functionalized PVDF-HFP membranes after hot press.

Gurley value provides an understanding of the tortuosity and porosity of a membrane. While membranes with high tortuosity (low porosity) are desirable for high-energy dense LIBs, excessive porosity may also cause premature cell failure due to short-circuit caused by the electrodeposited Li dendrites (particularly in case of Li metal anodes) that can easily penetrate the membranes.^[164, 165] Therefore, a tradeoff between porosity and tortuosity is typically necessary and is generally achieved through optimization for newly developed membranes. Our as-synthesized membranes show a very high air-permeability with an incredibly low Gurley value of only 4 s. Thus, we hot-pressed the membranes to

improve the layer-to-layer stacking and reduce the air-permeability. To allow comparison of electrochemical data obtained from the use of different membranes, their Gurley values were made similar (420 s), through optimization, by densification of the membranes by hot-pressing them for different amounts of time. We observed that the PVDF-HFP@5%-ND membranes required longer time to change the porosity of membrane when compared to PVDF-HFP@1% ND under the applied pressure and heat. Based on tension tests, it is noteworthy that the tensile strength of the membranes tends to increase with the increase in ND concentration, with the values for PVDF-HFP@5% ND and 1% ND samples being 25 and 18 MPa, respectively (Figure 4d). This difference in the mechanical strength is presumably due to a much stronger polymer-ND interaction, which can overcome the disruption in the packing of polymer chains. To further evaluate separator porosity, we conducted an n-butanol absorption experiment for the separators (detailed in the experimental section). Based on the calculations from Equation (1), we find the porosity of PVDF-HFP@5%ND is up to 71%, much higher than commercial PP separator (43%). Besides, contact angle tests (figure 47) reveal ND-functionalized separator has an excellent wettability due to its small contact angle with the electrolyte. The high porosity and wettability of the functional separator ensure its higher electrolyte uptake (162%) than PP (57%).

DSC cycles were conducted in the temperature range 25–175 °C to observe the crystalline behavior change with the increase in ND concentration (figure 48(a–c)). The crystallinity (X_c) of PVDF-HFP in the composites can be estimated by dividing the enthalpy of fusion (ΔH_f , area under the melting curve) of the samples to that (ΔH_f) of 100% crystalline pure PVDF-HFP, as shown below in the Equation (20).

$$Xc = \frac{\Delta H_f}{\Delta H_f^0} \times 100\% \quad (20)$$

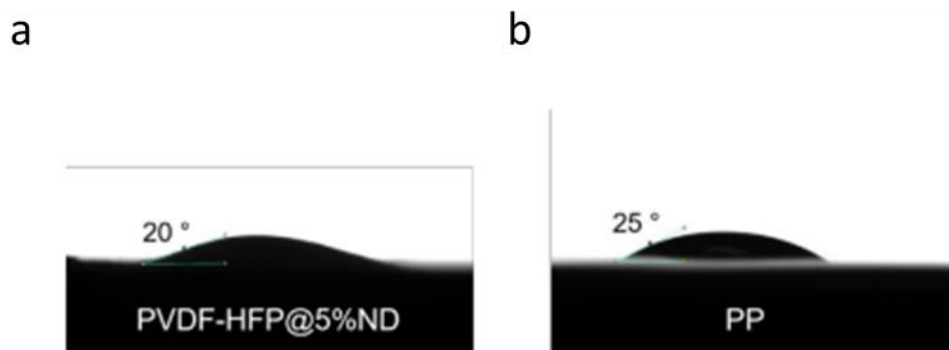


Figure 47. A comparison for the contact angles of ND functionalized and Celgard PP separators after contacting a drop of electrolyte solution for 1 s.

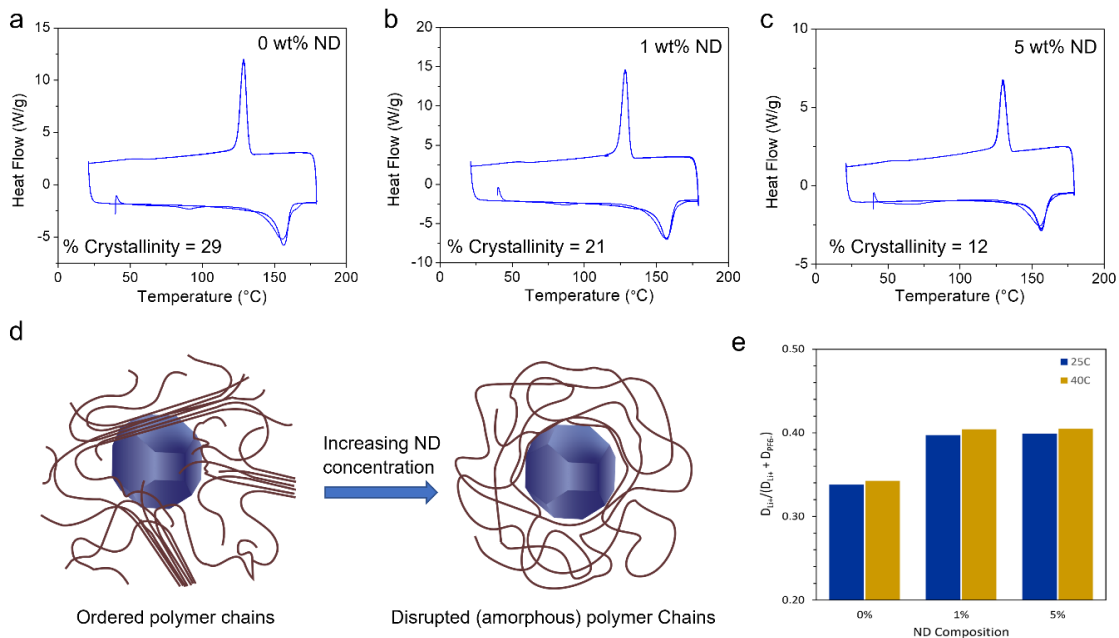


Figure 48. DSC cycles and crystallinity of (a) pure PVDF-HFP (0 wt. % ND); (b) PVDF-HFP@1%ND and PVDF-HFP@5%ND membranes; (d) a graphical representation of how semi-crystalline polymer are disrupted by NDs to form disordered polymer chains and reduce crystallinity; (e) Li⁺ diffusion coefficients of PVDF-HFP membranes with different mass fractions of NDs calculated by NMR.

The crystallinity of pristine PVDF-HFP nanofibers was 29%, which reduced to 12% for 5 wt.% ND-PVDF-HFP composite, clearly suggesting that the packing of the polymer chains is disrupted by the presence of NDs. NDs with their high exposed surface areas interact with the polymer chains, resulting in an overall more amorphous polymer network (figure 48d). This engineered microstructure is beneficial for the facile conduction of Li ions across the polymer surface, which therefore would improve the Li-ion conductivity of the membranes made thereof. Furthermore, the utilized NDs have a negatively charged -Si-PPG surface functionalization, which is beneficial for improving the Li-ion conductivity via Lewis acid-base-type interactions with the Li ions.^[166] This is consistent with the data obtained from the ⁷Li NMR pulse field gradient (PFG) experiment, which suggests enhanced Li-ion diffusivity (D_{Li}) with the increase in concentration of the NDs in the composite membranes (figure 48e). At 25 °C, the D_{Li} of 5% ND sample is $1.12 \times 10^{-10} \text{ m}^2 \text{ s}^{-1}$, which is much higher than pure PVDF-HFP ($8.69 \times 10^{-11} \text{ m}^2 \text{ s}^{-1}$) and 1% ND ($9.08 \times 10^{-11} \text{ m}^2 \text{ s}^{-1}$), and the Li ion transference number is also higher than that of PE-based separators as reported in literature.^[167]

The electrochemical properties of different separators were evaluated in coin cells (2032 type) with commercial high-loading $\text{LiNi}_{0.8}\text{Mn}_{0.1}\text{Co}_{0.1}\text{O}_2$ (NMC811) as a cathode ($\sim 10 \text{ mg cm}^{-2}$), Li foil as an anode (or reference electrode) and 1 M LiPF_6 in ethylene carbonate/diethyl carbonate (EC/DEC) as a classical electrolyte used in most publications. To check the electrochemical stability window, linear sweep voltammetry (LSV) tests were conducted for Li/separator/stainless steel cells with different separators. From the obtained LSV curves (figure 50(a)), we can find the functionalized separator (PVDF-HFP@5%ND) is more electrochemically stable than commercial PP separator in the Li cell environment.

In order to obtain high specific capacity and energy density, the assembled cells were first cycled within a voltage range of 2.8–4.4 V (vs Li/Li+) at a rate of C/3. As can be seen from figure 49a, the cell with PVDF-HFP@5%ND separator shows more stable performance and higher Coulombic efficiencies (CEs) compared to the one based on conventional separator (Celgard 2400). The initial specific capacity is up to 210 mAh g⁻¹ (stable at the 2nd cycle) and retains 204 mAh g⁻¹ (~97%) after 50 cycles, while the cell based on Celgard has a fast capacity degradation from 190 to 171 mAh g⁻¹. The stable performance of ND-based separator can be confirmed by their voltage profiles at different charge/discharge cycles (figure 49). The plateau features are obviously stable as cycles, which means that the separator is electrochemically stable and doesn't cause any side reaction. Besides, the PVDF-HFP@5%ND separator can help reduce the voltage hysteresis of the NCM811 cathode (figure 50(a)), leading to a good reversibility with high energy efficiency.

To further probe electrochemical stability of the membranes in the presence of NMC811, we cycled the cells in a lower cutoff voltage of 4.2 V (vs Li/Li+) at C/2, as compared in Figure 5c. The cell with ND functionalized separator still shows better performance with a higher capacity retention of 149 mAh g⁻¹ and high CE of 99.4% after cycling. The stable performance can be reflected by their voltage profiles at different cycles (Figure 5d). Besides, the cyclic voltammetry (CV) scans at a rate of 0.2 mV/s can also suggest that this membrane is stable in the cells (figure 52a). In addition to typical redox peaks for NCM811, there is no additional peaks that would indicate any side reactions – either due to decomposition of the separator or unwanted redox events in the presence of the separator. The electrochemical impedance was evaluated based on the Nyquist plots of the cell before and after cycling (figure 52b), the cells with ND-functionalized separator

also show a small semi-cycle after cycling, reflecting a small change in its charge-transfer resistance.

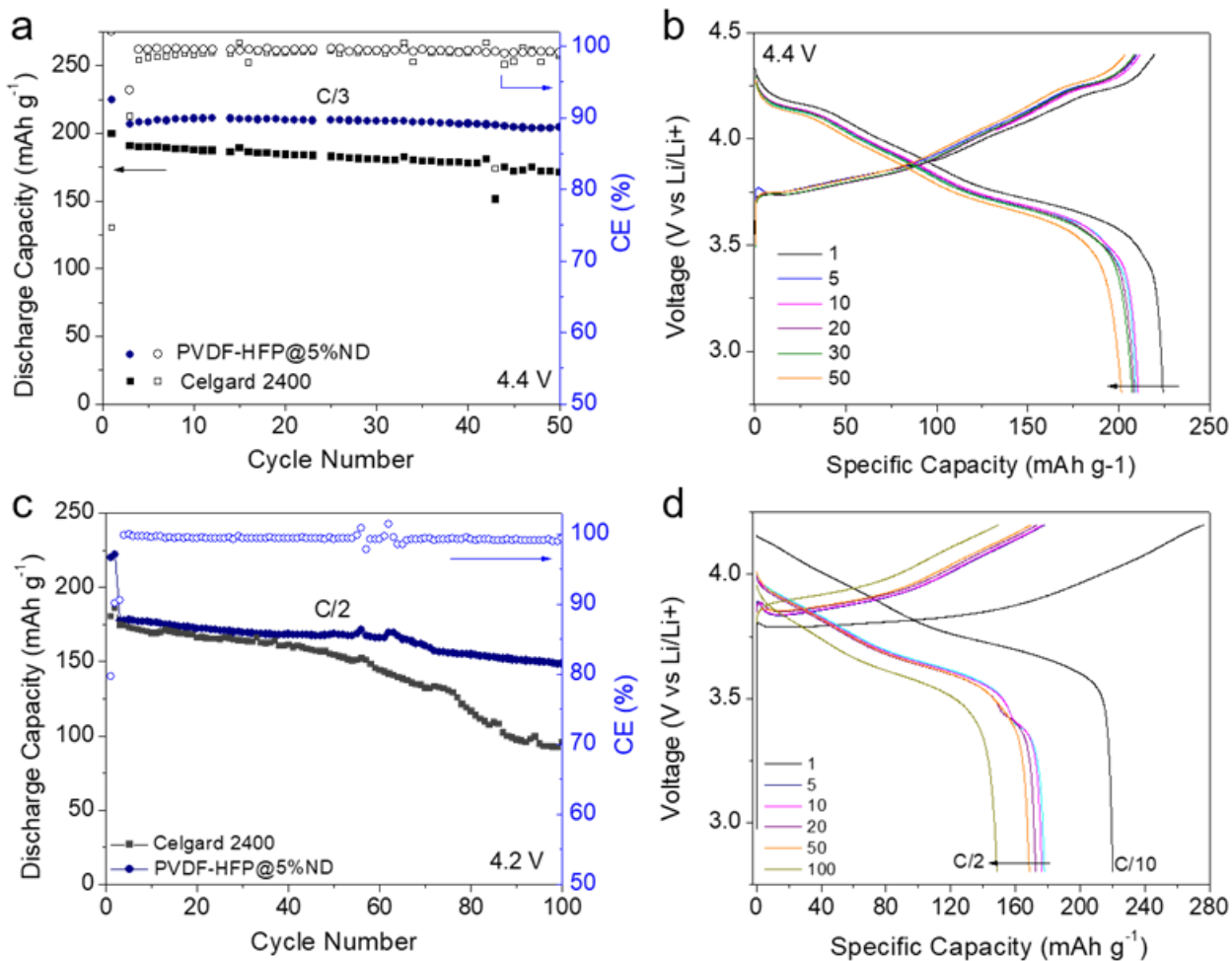


Figure 49. (a) Cycling performance of Li cells with Celgard 2400 and PVDF-HFP@5%ND separators in the potential range 2.8–4.4 V (vs Li/Li⁺); (b) voltage profiles at different stages of cycling; (c) long-term cycling performance and (d) voltage profile of the cells at C/3 between 2.8–4.2 V (vs Li/Li⁺).

We conducted post-mortem analysis for the cells with different separators after cycling to gain a better insight into the changes in Li metal anode and the function of separators. We captured SEM of the Li foils from different cells with ND-functionalized (PVDF-HFP@5%ND) and Celgard 2400 PP separators after cycling (2.8–4.2 V vs Li/Li⁺).

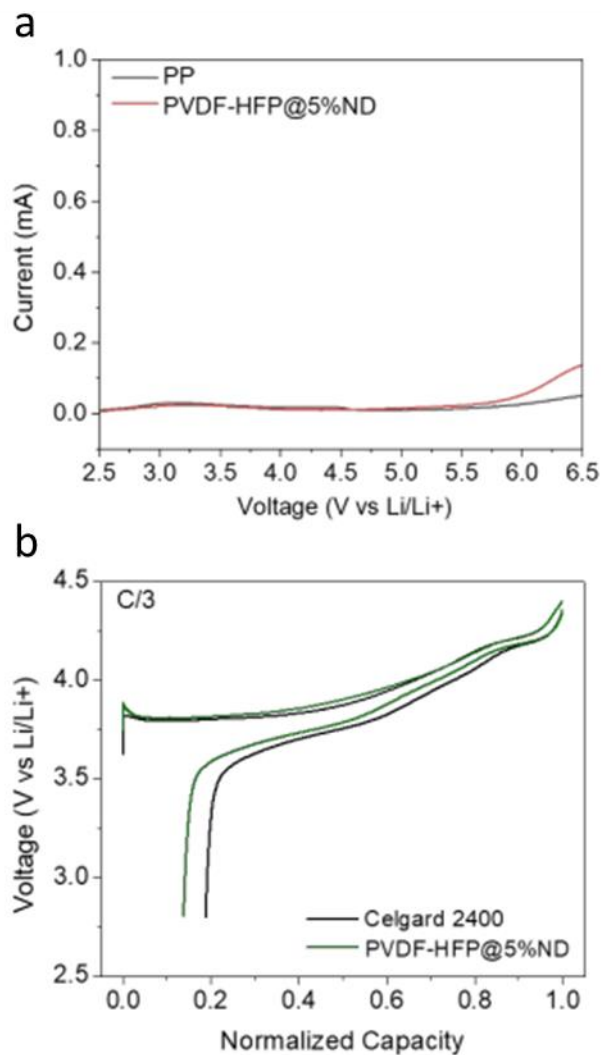


Figure 50. (a) LSV curves of Li/separator/stainless steel cells with PP and PVDF-HFP@5%ND separators at a scan rate of 10 mV s^{-1} from 2.5 to 6.5 V (vs Li/Li⁺); (b) voltage hysteresis of the cells using Celgard and PVDF-HFP@5%ND separators.

From the top-view SEM images (figure 51a and d), we can distinguish that the Li foil from the cell with PVDF-HFP@5%ND separator is significantly smoother than the one from the cell with PP separator that underwent non-uniform Li deposition with large dendrites. Cross-section SEM images (figure 51b and c; e and f) show that a very thick surface layers (mixed solid electrolyte interphase (SEI) and nanostructured Li metal) with

a porous structure formed on the anode surface in all cells, which is expected as Li shows poor plating stability in these electrolytes. However, with the PVDF-HFP@5%ND separator, the surface layer was very uniform and porous, which structure could allow ions to more easily penetrate into /extract from the inner dense Li for further plating/stripping process. In contrast, with PP separator, we noticed a non-uniform deposition/stripping of Li which could result in poor packing layer (and slightly thickness), large dead Li particles and cracks. These results indicate our ND-functionalized membranes are promising as a separator in LIBs even with a Li metal as anode.

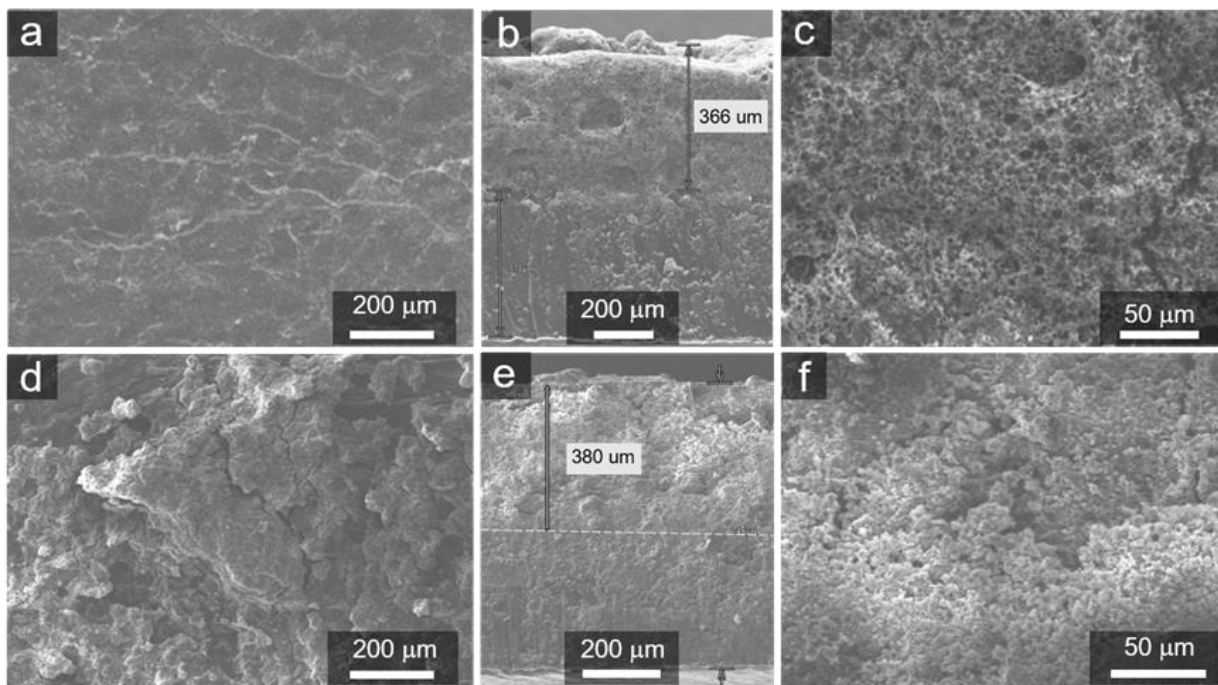


Figure 51. (a) Top-view and (b, c) cross-section SEM images of the Li anode from the cell with PVDF-HFP@5%ND separator after cycling; (d) Top-view and (e, f) cross-section SEM images of the Li anode from the cell with PP separator after cycling.

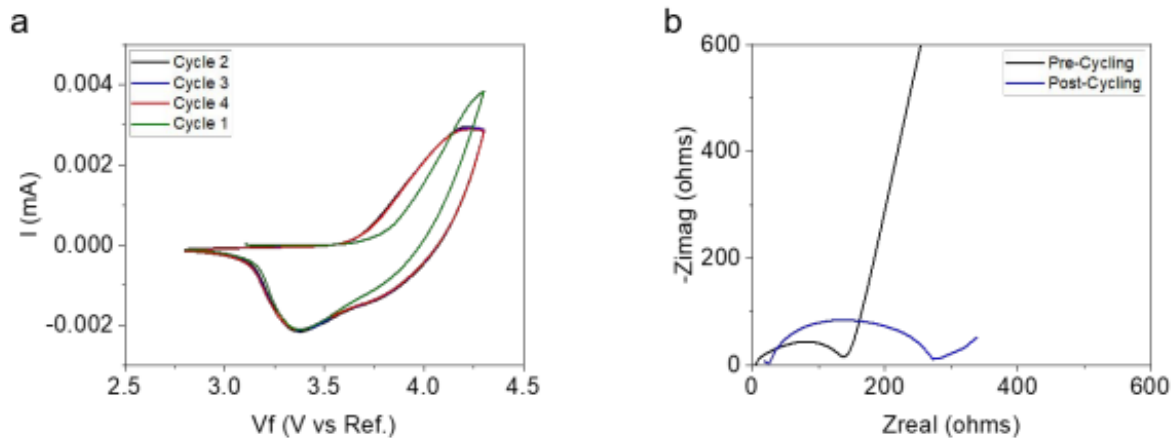


Figure 52. (a) CV curves of the cells with PVDF-HFP@5%ND separator at a scan rate of 0.2 mV s^{-1} ; (b) Nyquist plots of the cells before and after long-term cycling at $C/2$.

4.4 Conclusion

In summary, we demonstrated a facile electrospinning strategy for the fabrication of ND-functionalized PVDF-HFP nanofiber membranes as battery separators and this strategy allowed us to homogeneously disperse NDs as agglomerates along the nanofiber matrix, with dominant tendency of the agglomerate formation with increasing ND concentrations. We found that even with 5 wt.% ND incorporation in PVDF-HFP, which changed the polymer microstructure to be amorphous, the composites exhibited significantly improved thermal, mechanical and electrochemical properties with respect to the pristine polymer and traditional PP separator. DSC measurements confirmed the effective role of NDs in reducing the crystalline regions (i.e., increasing local disordering polymer chains) of the polymer in the composites and improving the Li-ion conductivity. PFG experiments further confirmed that the Li ion diffusions within the membrane increase with the increase in ND concentration. Benefiting from these promising features, the assembled cells with ND-functionalized nanofiber separator and NMC811 cathode

achieved excellent cycling stability with very small capacity loss and good rate performance, which were much better than otherwise analogous cells built by using conventional separators. This work could constitute a grand entry of NDs in the field of porous membranes and open the untapped potential of NDs for applications in LIBs and other energy storage devices.

CHAPTER 5. CONCLUSIONS AND FUTURE WORK

5.1 Anion Substituted Borohydride-based Solid Electrolytes for High Energy Lithium-Ion Batteries (LIBs)

5.1.1 Conclusions

Various halide doped LiBH_4 were synthesised using a melt-synthesis method which is much more efficient than the ubiquitously used ball-milling process. We noticed that the bromide halide salts didn't form a proper molten solution with LiBH_4 , but all the remaining tested halide salts form a molten solution with LiBH_4 when mixed in a 3:1 ratio. We noticed an increasing crystal volume size with increasing halide size, and a drastic difference between electrolytes doped with LiCl and LiF . LiBH_4 was also doped with various concentrations of LiCl and we notice that LiCl doping saturates at around 1:1 mole ratio of $\text{LiBH}_4 - \text{LiCl}$. The XRD Reitveld refinement shows no drastic difference in unit volume sizes between 1:1 and 3:1 ratios of $\text{LiBH}_4\text{-LiCl}$. The $3\text{LiBH}_4\text{-LiCl}$ when observed under a SEM showed LiCl -rich regions in the LiBH_4 bulk. The phase transitions of all these various electrolytes were investigated by DSC, and we noticed that for various halide doping, the phase transition temperature decreases with increasing halide size. The ionic conductivities of these various SSEs were studied using impedance spectroscopy, to observe that $3\text{LiBH}_4\text{-LiCl}$ shows that highest ionic conductivity compared to other halide doped LiBH_4 (and this composition was further used for other experiments). We then studied the critical current density of $3\text{LiBH}_4\text{-LiCl}$, by examining the performance of the SSE in Li symmetric cells. We observed that the critical current density is around 0.5 Ah cm^{-2} and is also stable when cycled with Li_2OHCl . Using melt-infiltration methods, which was previously studied by

our lab, half cells were made using various anodes and cathodes. Full cells were also assembled using NMC111 cathodes and silicon-carbon composites anodes. We notice that the degradation of the cells of the cells was due to mechanical failures, such as particle delamination and cracking, likely caused by the volume changes in active materials during cycling.

5.1.2 *Future Work Directions*

The NCM, graphite and silicon-carbon nanocomposite particles coated with Al₂O₃ demonstrated outstanding wetting by the SSE. We haven't systematically investigated the wetting of the electrode materials without such coatings by the SSE, but qualitatively it was significantly worse. Therefore, Al₂O₃ ALD coating was used to increase the wettability of electrodes. However, the thickness of the alumina coating and its chemistry was not optimized in this thesis, it simply was used to increase the wetting of the SSE with AM particles. The effect of thickness and chemistry of the ALD coating on SSE wetting and cell performance should be studied in future work. We also should investigate how these coatings help with SEI/CEI formation and eventually study the cycling performance with optimized coating layers. Since ALD is a very expensive process, one may investigate coating active material particles using a sol-gel process, with alumina or another desired oxide layer.

Since Li₂OHCl was used as the electrolyte for cathode infiltration since 3LiBH₄-LiCl reacts with NMC, to further understand the high-voltage performance of 3LiBH₄-LiCl, we may use cobalt-boride coated NMC111 to prevent the reaction between cathode and the SE.^[168] Also, in addition to robust coatings (in addition the alumina), we could test

lithium-sulfide (a conversion type cathode) to study cathode cycling performance. Another way to improve performance of full cells, is by using high conductivity SSEs for cathode infiltration such as tetrachloroaluminates doped with oxygen, to improve performance since using two SEs (one for anode and cathode) is becoming more common.^[169]

Finally, half cells and full cells post-mortem analyses showed particle cracking and delamination, so we may need to explore electrodes with zero-volume changing active materials and/or use external pressure to hinder electrolyte delamination and cracking. Swagelock cells are widely used to apply pressure on solid electrolyte cells, and hence we could systematically investigate the performance of the half cells and full cells under pressure using swagelock cells.^[170]

5.2 A Nanodiamond Enhanced Separator for High Energy Dense Lithium Ion Batteries (LIBs)

5.2.1 Conclusions

We have demonstrated the facile synthesis of PVDF-HFP polymer embedded with surface functionalized NDs, and we have confirmed through TEM and FTIR that these NDs are embedded through merely physical intercalation. Since the electrospun membranes had low gurley values, the membranes are hot-pressed to tune porosity, tortuosity, and thickness. These membranes realized higher mechanical and thermal properties of that of the pure polymer by 400% and 15%, respectively. The electrochemical properties of the membranes were investigated by impedance spectroscopy and CV. CV data shows that the polymer membrane, as a separator is stable between a wide voltage window of -1V to 6.5V. The Li⁺ ion diffusion co-efficient was determined using PFG NMR

and we realize that the D_{Li^+} is lower than that of the pristine polymer and is also higher than that of commercial LIB separators. Half-cells were tested to compare the performance of 5% ND PVDF-HFP samples with Celgard separators using an electrolyte that is notorious of lithium dendrite growth. We notice that ND based separators outperform Celgard separators by realizing higher capacity and longer cycling life.

5.2.2 *Future Work*

Based on our experimental results, we observed that the NDs embedded in the polymer matrix is mostly physical, rather than chemical. It would be interesting to understand the structure-property relationships in terms of electrochemical and mechanical properties, when the NDs are intercalated chemically in the polymer matrix. We hope to see increased mechanical properties and thermal properties. In addition to NDs being physically intercalated and agglomerated, we hope to use methods such as longer tip sonication times and various surface functionalization to reduce ND agglomeration. We would like to investigate the mechanical, thermal, and electrochemical properties as a result of lower ND agglomeration and effect surface functionalization.

Since our work shows the synthesis of PVDF-HFP based ND polymer composites, we hope to study the intercalation of NDs in various other polymer systems such as m-aramid. Since ma-aramid is a mechanically and thermally robust polymer compared to PVDF-HFP, it would be interesting to study the effects of ND intercalation (as seen in figure 53). Finally it will be interesting to study the use as ND as fillers for SPEs since there have been multiple studies, using inorganics nano-fillers for SPEs.^[171] We would like to investigate the mechanical, thermal and electrochemical properties as a result of ND

intercalation and effect surface functionalization in SPEs. We hypothesize that the surface functionalize should play an engaging role in Li^+ conduction along the polymer chains and SEI formation with various anode materials.

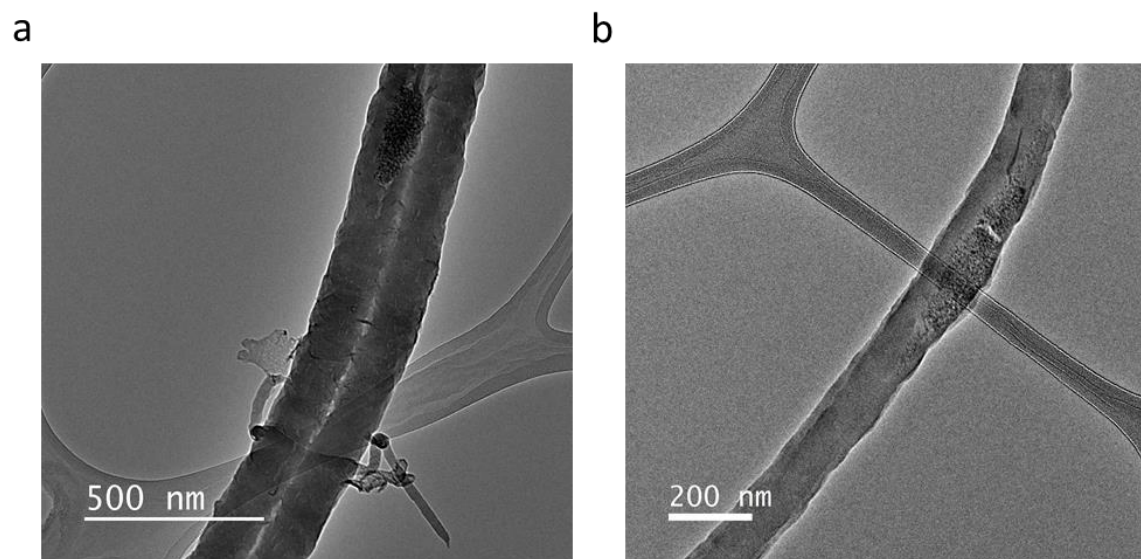


Figure 53. ND m-aramid polymer composite with high degree of ND agglomeration.

APPENDIX A. PERMISSION LICENSES FOR THE REUSE OF COPYRIGHT MATERIALS

Permission for schematic of inorganic solid electrolyte battery:

12/11/23, 11:06 AM

RightsLink - Your Account

SPRINGER NATURE LICENSE TERMS AND CONDITIONS

Dec 11, 2023

This Agreement between Georgia Institute of Technology -- Aashray Narla ("You") and Springer Nature ("Springer Nature") consists of your license details and the terms and conditions provided by Springer Nature and Copyright Clearance Center.

License Number	5685971288673
License date	Dec 11, 2023
Licensed Content Publisher	Springer Nature
Licensed Content Publication	Nature Energy
Licensed Content Title	Batteries: Getting solid
Licensed Content Author	Yong-Sheng Hu
Licensed Content Date	Apr 7, 2018
Type of Use	Thesis/Dissertation
Requestor type	academic/university or research institute
Format	print and electronic
Portion	figures/tables/illustrations
Number of figures/tables/illustrations	1
Would you like a high resolution image with your order?	no
Will you be translating?	no
Circulation/distribution	50000 or greater
Author of this Springer Nature content	no
Title of new work	PhD Dissertation - Aashray
Institution name	GaTech
Expected presentation date	Dec 2023
Portions	1
Requestor Location	Georgia Institute of Technology Rm 252, Love Manufacturing Building 771 Ferst Dr. ATLANTA, GA 30332 United States Attn: Georgia Institute of Technology
Total	0.00 USD

Terms and Conditions

Springer Nature Customer Service Centre GmbH Terms and Conditions

The following terms and conditions ("Terms and Conditions") together with the terms specified in your [RightsLink] constitute the License ("License") between you as Licensee and Springer Nature Customer Service Centre GmbH as Licensor. By clicking 'accept' and completing the transaction for your use of the material ("Licensed Material"), you confirm your acceptance of and obligation to be bound by these Terms and Conditions.

1. Grant and Scope of License

Permissions for XPS schematic:

11/3/23, 4:36 PM

RightsLink - Your Account

SPRINGER NATURE LICENSE TERMS AND CONDITIONS

Nov 03, 2023

This Agreement between Georgia Institute of Technology -- Aashray Narla ("You") and Springer Nature ("Springer Nature") consists of your license details and the terms and conditions provided by Springer Nature and Copyright Clearance Center.

License Number	5641410609347
License date	Oct 03, 2023
Licensed Content Publisher	Springer Nature
Licensed Content Publication	Springer eBook
Licensed Content Title	X-Ray Photoelectron Spectroscopy (XPS) and Auger Electron Spectroscopy (AES)
Licensed Content Author	Richard T. Haasch
Licensed Content Date	Jan 1, 2014
Type of Use	Thesis/Dissertation
Requestor type	academic/university or research institute
Format	electronic
Portion	figures/tables/illustrations
Number of figures/tables/illustrations	1
Will you be translating?	no
Circulation/distribution	50000 or greater
Author of this Springer Nature content	no
Title	PhD Dissertation - Aashray
Institution name	GaTech
Expected presentation date	Dec 2023
Portions	Figure 3.5
Requestor Location	Georgia Institute of Technology Rm 252, Love Manufacturing Building 771 Ferst Dr. ATLANTA, GA 30332 United States Attn: Georgia Institute of Technology
Total	0.00 USD

Terms and Conditions

Springer Nature Customer Service Centre GmbH Terms and Conditions

The following terms and conditions ("Terms and Conditions") together with the terms specified in your [RightsLink] constitute the License ("License") between you as Licensee and Springer Nature Customer Service Centre GmbH as Licensor. By clicking 'accept' and completing the transaction for your use of the material ("Licensed Material"), you confirm your acceptance of and obligation to be bound by these Terms and Conditions.

1. Grant and Scope of License

- 1.1. The Licensor grants you a personal, non-exclusive, non-transferable, non-sublicensable, revocable, world-wide License to reproduce, distribute, communicate to the public, make available, broadcast, electronically transmit or create derivative works using the Licensed Material for the purpose(s) specified in your RightsLink License Details only.

<https://s100.copyright.com/MyAccount/web/jsp/viewprintablelicensefrommyorders.jsp?ref=ed849b3a-9b65-4688-92b4-814a5749b490&email=>

1/4

Permission for the stripping and plating schematic:

11/3/23, 4:34 PM

RightsLink - Your Account

SPRINGER NATURE LICENSE TERMS AND CONDITIONS

Nov 03, 2023

This Agreement between Georgia Institute of Technology -- Aashray Narla ("You") and Springer Nature ("Springer Nature") consists of your license details and the terms and conditions provided by Springer Nature and Copyright Clearance Center.

License Number	5651030458058
License date	Oct 16, 2023
Licensed Content Publisher	Springer Nature
Licensed Content Publication	Nature Materials
Licensed Content Title	Critical stripping current leads to dendrite formation on plating in lithium anode solid electrolyte cells
Licensed Content Author	Jitti Kasemchainan et al
Licensed Content Date	Jul 29, 2019
Type of Use	Thesis/Dissertation
Requestor type	academic/university or research institute
Format	electronic
Portion	figures/tables/illustrations
Number of figures/tables/illustrations	1
Would you like a high resolution image with your order?	no
Will you be translating?	no
Circulation/distribution	50000 or greater
Author of this Springer Nature content	no
Title of new work	PhD Dissertation - Aashray
Institution name	GaTech
Expected presentation date	Dec 2023
Portions	Figure 4
Requestor Location	Georgia Institute of Technology Rm 252, Love Manufacturing Building 771 Ferst Dr. ATLANTA, GA 30332 United States Attn: Georgia Institute of Technology
Total	0.00 USD

Terms and Conditions

Springer Nature Customer Service Centre GmbH Terms and Conditions

The following terms and conditions ("Terms and Conditions") together with the terms specified in your [RightsLink] constitute the License ("License") between you as Licensee and Springer Nature Customer Service Centre GmbH as Licensor. By clicking 'accept' and completing the transaction for your use of the material ("Licensed Material"), you confirm your acceptance of and obligation to be bound by these Terms and Conditions.

Permission for the borohydride structure schematic:

11/3/23, 4:39 PM

RightsLink - Your Account

ELSEVIER LICENSE TERMS AND CONDITIONS

Nov 03, 2023

This Agreement between Georgia Institute of Technology – Aashray Naria ("You") and Elsevier ("Elsevier") consists of your license details and the terms and conditions provided by Elsevier and Copyright Clearance Center.

License Number	5661531422414
License date	Nov 03, 2023
Licensed Content Publisher	Elsevier
Licensed Content Publication	Journal of Solid State Chemistry
Licensed Content Title	Structure and vibrational dynamics of isotopically labeled lithium borohydride using neutron diffraction and spectroscopy
Licensed Content Author	Michael R. Hartman, John J. Rush, Terrence J. Udovic, Robert C. Bowman, Son-Jong Hwang
Licensed Content Date	Apr 1, 2007
Licensed Content Volume	180
Licensed Content Issue	4
Licensed Content Pages	8
Start Page	1298
End Page	1305
Type of Use	reuse in a thesis/dissertation
Portion	figures/tables/illustrations
Number of figures/tables/illustrations	2
Format	electronic
Are you the author of this Elsevier article?	No
Will you be translating?	No
Title of new work	PhD Dissertation - Aashray
Institution name	GaTech
Expected presentation date	Dec 2023
Portions	Figure 3 and Figure 4
Requestor Location	Georgia Institute of Technology Rm 252, Love Manufacturing Building 771 Ferst Dr. ATLANTA, GA 30332 United States Attn: Georgia Institute of Technology
Publisher Tax ID	98-0397604
Total	0.00 USD
Terms and Conditions	

INTRODUCTION

1. The publisher for this copyrighted material is Elsevier. By clicking "accept" in connection with completing this licensing transaction, you agree that the following terms and conditions apply to this transaction (along with the Billing and Payment terms and conditions established by Copyright Clearance Center, Inc. ("CCC"), at the time that you opened your RightsLink account and that are available at any time at <https://myaccount.copyright.com>).

GENERAL TERMS

<https://s100.copyright.com/MyAccount/web/jsp/viewprintablelicensefrommyorders.jsp?ref=0526b4ef-e3f1-498b-b305-467#30731b0&email=>

1/4

REFERENCES

1. Manthiram, A., X. Yu, and S. Wang, *Lithium battery chemistries enabled by solid-state electrolytes*. Nature Reviews Materials, 2017. **2**(4): p. 16103.
2. Wang, C., et al., *Garnet-Type Solid-State Electrolytes: Materials, Interfaces, and Batteries*. Chemical Reviews, 2020. **120**(10): p. 4257-4300.
3. Chen, T., et al., *Argyrodite Solid Electrolyte with a Stable Interface and Superior Dendrite Suppression Capability Realized by ZnO Co-Doping*. ACS Applied Materials & Interfaces, 2019. **11**(43): p. 40808-40816.
4. Kato, Y., et al., *High-power all-solid-state batteries using sulfide superionic conductors*. Nature Energy, 2016. **1**(4): p. 16030.
5. Ye, L. and X. Li, *A dynamic stability design strategy for lithium metal solid state batteries*. Nature, 2021. **593**(7858): p. 218-222.
6. Hu, Y.-S., *Batteries: Getting solid*. Nature Energy, 2016. **1**(4): p. 16042.
7. Famprakis, T., et al., *Fundamentals of inorganic solid-state electrolytes for batteries*. Nature Materials, 2019. **18**(12): p. 1278-1291.
8. Zhao, Q., et al., *Designing solid-state electrolytes for safe, energy-dense batteries*. Nature Reviews Materials, 2020. **5**(3): p. 229-252.
9. Zhang, Y., et al., *Field assisted sintering of dense Al-substituted cubic phase $\text{Li}_7\text{La}_3\text{Zr}_2\text{O}_{12}$ solid electrolytes*. Journal of Power Sources, 2014. **268**: p. 960-964.
10. Duan, H., et al., *Stability of garnet-type Li ion conductors: An overview*. Solid State Ionics, 2018. **318**: p. 45-53.
11. López-Aranguren, P., et al., *Crystalline LiPON as a Bulk-Type Solid Electrolyte*. ACS Energy Letters, 2021. **6**(2): p. 445-450.
12. Cuan, J., et al., *Borohydride-Scaffolded Li/Na/Mg Fast Ionic Conductors for Promising Solid-State Electrolytes*. Advanced Materials, 2019. **31**(1): p. 1803533.
13. Feng, X., et al., *Mitigating thermal runaway of lithium-ion batteries*. Joule, 2020. **4**(4): p. 743-770.
14. Liu, J., et al., *Experimental study of thermal runaway process of 18650 lithium-ion battery*. Materials, 2017. **10**(3): p. 230.
15. Nitta, N., et al., *Li-ion battery materials: present and future*. Materials Today, 2015. **18**(5): p. 252-264.

16. Goodenough, J.B. and K.-S. Park, *The Li-Ion Rechargeable Battery: A Perspective*. Journal of the American Chemical Society, 2013. **135**(4): p. 1167-1176.
17. Yuan, L.-X., et al., *Development and challenges of LiFePO₄ cathode material for lithium-ion batteries*. Energy & Environmental Science, 2011. **4**(2): p. 269-284.
18. Liu, C., Z.G. Neale, and G. Cao, *Understanding electrochemical potentials of cathode materials in rechargeable batteries*. Materials Today, 2016. **19**(2): p. 109-123.
19. An, S.J., et al., *The state of understanding of the lithium-ion-battery graphite solid electrolyte interphase (SEI) and its relationship to formation cycling*. Carbon, 2016. **105**: p. 52-76.
20. Fuller, T.F.H., John N, *Electrochemical Engineering*. 2018: Wiley.
21. Bard, A.J., Faulkner, L. R., *Electrochemical Methods: Fundamentals and Applications*. 2nd Edition ed. 2000: John Wiley & Sons, Incorporated.
22. Manthiram, A., *A reflection on lithium-ion battery cathode chemistry*. Nature Communications, 2020. **11**(1): p. 1550.
23. Whittingham, M.S., *Electrical energy storage and intercalation chemistry*. Science, 1976. **192**(4244): p. 1126-1127.
24. Li, J., et al., *Structural origin of the high-voltage instability of lithium cobalt oxide*. Nature Nanotechnology, 2021. **16**(5): p. 599-605.
25. Dahn, J.R., et al., *Thermal stability of Li_xCoO₂, Li_xNiO₂ and λ-MnO₂ and consequences for the safety of Li-ion cells*. Solid State Ionics, 1994. **69**(3): p. 265-270.
26. Li, W., et al., *Collapse of LiNi_{1-x-y}CoxMnyO₂ Lattice at Deep Charge Irrespective of Nickel Content in Lithium-Ion Batteries*. Journal of the American Chemical Society, 2019. **141**(13): p. 5097-5101.
27. Li, W., et al., *Long-Term Cyclability of NCM-811 at High Voltages in Lithium-Ion Batteries: an In-Depth Diagnostic Study*. Chemistry of Materials, 2020. **32**(18): p. 7796-7804.
28. Li, W., E.M. Erickson, and A. Manthiram, *High-nickel layered oxide cathodes for lithium-based automotive batteries*. Nature Energy, 2020. **5**(1): p. 26-34.
29. Park, K.-J., et al., *Degradation Mechanism of Ni-Enriched NCA Cathode for Lithium Batteries: Are Microcracks Really Critical?* ACS Energy Letters, 2019. **4**(6): p. 1394-1400.

30. Zhao, X. and G. Ceder, *Zero-strain cathode materials for Li-ion batteries*. Joule, 2022. **6**(12): p. 2683-2685.
31. Wang, H., et al., *Y-F co-doping behavior of LiFePO₄/C nanocomposites for high-rate lithium-ion batteries*. New Journal of Chemistry, 2021. **45**(12): p. 5695-5703.
32. Wu, F. and G. Yushin, *Conversion cathodes for rechargeable lithium and lithium-ion batteries*. Energy & Environmental Science, 2017. **10**(2): p. 435-459.
33. Kim, H., et al., *In Situ Formation of Protective Coatings on Sulfur Cathodes in Lithium Batteries with LiFSI-Based Organic Electrolytes*. Advanced Energy Materials, 2015. **5**(6): p. 1401792.
34. Lee, J.T., et al., *Sulfur-Infiltrated Micro- and Mesoporous Silicon Carbide-Derived Carbon Cathode for High-Performance Lithium Sulfur Batteries*. Advanced Materials, 2013. **25**(33): p. 4573-4579.
35. Shi, H., et al., *Structure and Lithium Intercalation Properties of Synthetic and Natural Graphite*. Journal of The Electrochemical Society, 1996. **143**(11): p. 3466.
36. Evanoff, K., et al., *Nanosilicon-Coated Graphene Granules as Anodes for Li-Ion Batteries*. Advanced Energy Materials, 2011. **1**(4): p. 495-498.
37. Magasinski, A., et al., *Toward Efficient Binders for Li-Ion Battery Si-Based Anodes: Polyacrylic Acid*. ACS Applied Materials & Interfaces, 2010. **2**(11): p. 3004-3010.
38. Magasinski, A., et al., *High-performance lithium-ion anodes using a hierarchical bottom-up approach*. Nature Materials, 2010. **9**(4): p. 353-358.
39. Ng, S.-H., et al., *Highly Reversible Lithium Storage in Spheroidal Carbon-Coated Silicon Nanocomposites as Anodes for Lithium-Ion Batteries*. Angewandte Chemie International Edition, 2006. **45**(41): p. 6896-6899.
40. Jaumann, T., et al., *Lifetime vs. rate capability: Understanding the role of FEC and VC in high-energy Li-ion batteries with nano-silicon anodes*. Energy Storage Materials, 2017. **6**: p. 26-35.
41. Nguyen, C.C. and B.L. Lucht, *Comparative Study of Fluoroethylene Carbonate and Vinylene Carbonate for Silicon Anodes in Lithium Ion Batteries*. Journal of The Electrochemical Society, 2014. **161**(12): p. A1933.
42. Kalhoff, J., et al., *Safer Electrolytes for Lithium-Ion Batteries: State of the Art and Perspectives*. ChemSusChem, 2015. **8**(13): p. 2154-2175.
43. Xu, K., *Nonaqueous Liquid Electrolytes for Lithium-Based Rechargeable Batteries*. Chemical Reviews, 2004. **104**(10): p. 4303-4418.

44. Xu, K., *Electrolytes and Interphases in Li-Ion Batteries and Beyond*. Chemical Reviews, 2014. **114**(23): p. 11503-11618.
45. Krause, L.J., et al., *Corrosion of aluminum at high voltages in non-aqueous electrolytes containing perfluoroalkylsulfonyle imides; new lithium salts for lithium-ion cells*. Journal of Power Sources, 1997. **68**(2): p. 320-325.
46. Huang, X. and J. Hitt, *Lithium ion battery separators: Development and performance characterization of a composite membrane*. Journal of Membrane Science, 2013. **425-426**: p. 163-168.
47. Zhang, Y., et al., *A thin inorganic composite separator for lithium-ion batteries*. Journal of Membrane Science, 2016. **509**: p. 19-26.
48. Kovalenko, I., et al., *A Major Constituent of Brown Algae for Use in High-Capacity Li-Ion Batteries*. Science, 2011. **334**(6052): p. 75-79.
49. Shi, Y., X. Zhou, and G. Yu, *Material and Structural Design of Novel Binder Systems for High-Energy, High-Power Lithium-Ion Batteries*. Accounts of Chemical Research, 2017. **50**(11): p. 2642-2652.
50. Lux, S.F., et al., *Low Cost, Environmentally Benign Binders for Lithium-Ion Batteries*. Journal of The Electrochemical Society, 2010. **157**(3): p. A320.
51. Nguyen, V.A. and C. Kuss, *Review—Conducting Polymer-Based Binders for Lithium-Ion Batteries and Beyond*. Journal of The Electrochemical Society, 2020. **167**(6): p. 065501.
52. Zhao, Y.-M., et al., *Advances of polymer binders for silicon-based anodes in high energy density lithium-ion batteries*. InfoMat, 2021. **3**(5): p. 460-501.
53. Jin, S., et al., *Advanced 3D Current Collectors for Lithium-Based Batteries*. Advanced Materials, 2018. **30**(48): p. 1802014.
54. Myung, S.-T., Y. Hitoshi, and Y.-K. Sun, *Electrochemical behavior and passivation of current collectors in lithium-ion batteries*. Journal of Materials Chemistry, 2011. **21**(27): p. 9891-9911.
55. Zhu, P., et al., *A review of current collectors for lithium-ion batteries*. Journal of Power Sources, 2021. **485**: p. 229321.
56. Qi, X., et al., *Understanding the influence of conductive carbon additives surface area on the rate performance of LiFePO₄ cathodes for lithium ion batteries*. Carbon, 2013. **64**: p. 334-340.
57. Zhang, W., et al., *The Detrimental Effects of Carbon Additives in Li₁₀GeP₂S₁₂-Based Solid-State Batteries*. ACS Applied Materials & Interfaces, 2017. **9**(41): p. 35888-35896.

58. Zhang, Z. and L.F. Nazar, *Exploiting the paddle-wheel mechanism for the design of fast ion conductors*. Nature Reviews Materials, 2022. **7**(5): p. 389-405.
59. Yang, H. and N. Wu, *Ionic conductivity and ion transport mechanisms of solid-state lithium-ion battery electrolytes: A review*. Energy Science & Engineering, 2022. **10**(5): p. 1643-1671.
60. Wang, Y., et al., *Design principles for solid-state lithium superionic conductors*. Nature Materials, 2015. **14**(10): p. 1026-1031.
61. Dawson, J.A., et al., *Atomic-Scale Influence of Grain Boundaries on Li-Ion Conduction in Solid Electrolytes for All-Solid-State Batteries*. Journal of the American Chemical Society, 2018. **140**(1): p. 362-368.
62. Han, F., et al., *Electrochemical Stability of Li₁₀GeP₂S₁₂ and Li₇La₃Zr₂O₁₂ Solid Electrolytes*. Advanced Energy Materials, 2016. **6**(8): p. 1501590.
63. Marchiori, C.F.N., et al., *Understanding the Electrochemical Stability Window of Polymer Electrolytes in Solid-State Batteries from Atomic-Scale Modeling: The Role of Li-Ion Salts*. Chemistry of Materials, 2020. **32**(17): p. 7237-7246.
64. Song, A.-Y., et al., *Protons Enhance Conductivities in Lithium Halide Hydroxide/Lithium Oxyhalide Solid Electrolytes by Forming Rotating Hydroxy Groups*. Advanced Energy Materials, 2018. **8**(3): p. 1700971.
65. Uhlmann, C., et al., *Interface and grain boundary resistance of a lithium lanthanum titanate (Li_{3x}La_{2/3-x}TiO₃, LLTO) solid electrolyte*. Journal of Power Sources, 2016. **307**: p. 578-586.
66. Li, Y., et al., *Fluorine-Doped Antiperovskite Electrolyte for All-Solid-State Lithium-Ion Batteries*. Angewandte Chemie International Edition, 2016. **55**(34): p. 9965-9968.
67. Liu, Q., et al., *Challenges and perspectives of garnet solid electrolytes for all solid-state lithium batteries*. Journal of Power Sources, 2018. **389**: p. 120-134.
68. Wolfenstine, J., et al., *Mechanical behavior of Li-ion-conducting crystalline oxide-based solid electrolytes: a brief review*. Ionics, 2018. **24**(5): p. 1271-1276.
69. Kerman, K., et al., *Review—Practical Challenges Hindering the Development of Solid State Li Ion Batteries*. Journal of The Electrochemical Society, 2017. **164**(7): p. A1731.
70. Thangadurai, V., S. Narayanan, and D. Pinzaru, *Garnet-type solid-state fast Li ion conductors for Li batteries: critical review*. Chemical Society Reviews, 2014. **43**(13): p. 4714-4727.

71. Li, C., et al., *NaSICON: A promising solid electrolyte for solid-state sodium batteries*. *Interdisciplinary Materials*, 2022. **1**(3): p. 396-416.
72. Dias, J.A., S.H. Santagneli, and Y. Messaddeq, *Methods for Lithium Ion NASICON Preparation: From Solid-State Synthesis to Highly Conductive Glass-Ceramics*. *The Journal of Physical Chemistry C*, 2020. **124**(49): p. 26518-26539.
73. Wang, C., K. Adair, and X. Sun, *All-Solid-State Lithium Metal Batteries with Sulfide Electrolytes: Understanding Interfacial Ion and Electron Transport*. *Accounts of Materials Research*, 2022. **3**(1): p. 21-32.
74. Miura, A., et al., *Liquid-phase syntheses of sulfide electrolytes for all-solid-state lithium battery*. *Nature Reviews Chemistry*, 2019. **3**(3): p. 189-198.
75. Qiu, J., et al., *Enabling Stable Cycling of 4.2 V High-Voltage All-Solid-State Batteries with PEO-Based Solid Electrolyte*. *Advanced Functional Materials*, 2020. **30**(22): p. 1909392.
76. Zhao, Q., et al., *Solid-state polymer electrolytes with in-built fast interfacial transport for secondary lithium batteries*. *Nature Energy*, 2019. **4**(5): p. 365-373.
77. Kelly, T., et al., *In Situ Study of Strain-Dependent Ion Conductivity of Stretchable Polyethylene Oxide Electrolyte*. *Scientific Reports*, 2016. **6**(1): p. 20128.
78. Talaie, E., et al., *Methods and Protocols for Electrochemical Energy Storage Materials Research*. *Chemistry of Materials*, 2017. **29**(1): p. 90-105.
79. Britannica, T.E.o.E. *Bragg Diffraction*. 2023 October 3 2023]; Available from: <https://www.britannica.com/science/Bragg-law#/media/1/76973/17859>.
80. Haasch, R.T., *X-Ray Photoelectron Spectroscopy (XPS) and Auger Electron Spectroscopy (AES)*, in *Practical Materials Characterization*, M. Sardela, Editor. 2014, Springer New York: New York, NY. p. 93-132.
81. Chang, B.-Y. and S.-M. Park, *Electrochemical Impedance Spectroscopy*. *Annual Review of Analytical Chemistry*, 2010. **3**(1): p. 207-229.
82. Lu, Z. and F. Ciucci, *Metal Borohydrides as Electrolytes for Solid-State Li, Na, Mg, and Ca Batteries: A First-Principles Study*. *Chemistry of Materials*, 2017. **29**(21): p. 9308-9319.
83. Payandeh, S., et al., *Nido-Borate/Closo-Borate Mixed-Anion Electrolytes for All-Solid-State Batteries*. *Chemistry of Materials*, 2020. **32**(3): p. 1101-1110.
84. White, J.L., et al., *Understanding and Mitigating the Effects of Stable Dodecahydro-closo-dodecaborate Intermediates on Hydrogen-Storage Reactions*. *The Journal of Physical Chemistry C*, 2016. **120**(45): p. 25725-25731.

85. Shevlin, S.A., C. Cazorla, and Z.X. Guo, *Structure and Defect Chemistry of Low- and High-Temperature Phases of LiBH₄*. The Journal of Physical Chemistry C, 2012. **116**(25): p. 13488-13496.
86. Soulié, J.P., et al., *Lithium boro-hydride LiBH₄: I. Crystal structure*. Journal of Alloys and Compounds, 2002. **346**(1): p. 200-205.
87. Hartman, M.R., et al., *Structure and vibrational dynamics of isotopically labeled lithium borohydride using neutron diffraction and spectroscopy*. Journal of Solid State Chemistry, 2007. **180**(4): p. 1298-1305.
88. Cascallana-Matias, I., et al., *Phase Behavior in the LiBH₄-LiBr System and Structure of the Anion-Stabilized Fast Ionic, High Temperature Phase*. Chemistry of Materials, 2015. **27**(22): p. 7780-7787.
89. Gulino, V., et al., *Enhancing Li-Ion Conductivity in LiBH₄-Based Solid Electrolytes by Adding Various Nanosized Oxides*. ACS Applied Energy Materials, 2020. **3**(5): p. 4941-4948.
90. Matsuo, M., et al., *Lithium superionic conduction in lithium borohydride accompanied by structural transition*. Applied Physics Letters, 2007. **91**(22): p. 224103.
91. Blanchard, D., et al., *Nanoconfined LiBH₄ as a Fast Lithium Ion Conductor*. Advanced Functional Materials, 2015. **25**(2): p. 184-192.
92. Oguchi, H., et al., *Experimental and computational studies on structural transitions in the LiBH₄-LiI pseudobinary system*. Applied Physics Letters, 2009. **94**(14): p. 141912.
93. Maekawa, H., et al., *Halide-Stabilized LiBH₄, a Room-Temperature Lithium Fast-Ion Conductor*. Journal of the American Chemical Society, 2009. **131**(3): p. 894-895.
94. Das, S., et al., *All-Solid-State Lithium-Sulfur Battery Based on a Nanoconfined LiBH₄ Electrolyte*. Journal of The Electrochemical Society, 2016. **163**(9): p. A2029.
95. Choi, Y.S., et al., *Interface-enhanced Li ion conduction in a LiBH₄-SiO₂ solid electrolyte*. Physical Chemistry Chemical Physics, 2016. **18**(32): p. 22540-22547.
96. Lu, F., et al., *A High-Performance Li-B-H Electrolyte for All-Solid-State Li Batteries*. Advanced Functional Materials, 2019. **29**(15): p. 1809219.
97. Unemoto, A., et al., *Pseudo-binary electrolyte, LiBH₄-LiCl, for bulk-type all-solid-state lithium-sulfur battery*. Nanotechnology, 2015. **26**(25): p. 254001.

98. Sveinbjörnsson, D., et al., *The LiBH₄-LiI Solid Solution as an Electrolyte in an All-Solid-State Battery*. Journal of The Electrochemical Society, 2014. **161**(9): p. A1432.
99. Hu, L., et al., *Interface Modification and Halide Substitution To Achieve High Ionic Conductivity in LiBH₄-Based Electrolytes for all-Solid-State Batteries*. ACS Applied Materials & Interfaces, 2022. **14**(1): p. 1260-1269.
100. Unemoto, A., et al., *Stable Interface Formation between TiS₂ and LiBH₄ in Bulk-Type All-Solid-State Lithium Batteries*. Chemistry of Materials, 2015. **27**(15): p. 5407-5416.
101. Han, F., et al., *High electronic conductivity as the origin of lithium dendrite formation within solid electrolytes*. Nature Energy, 2019. **4**(3): p. 187-196.
102. Kasemchainan, J., et al., *Critical stripping current leads to dendrite formation on plating in lithium anode solid electrolyte cells*. Nature Materials, 2019. **18**(10): p. 1105-1111.
103. Raj, V., et al., *Direct correlation between void formation and lithium dendrite growth in solid-state electrolytes with interlayers*. Nature Materials, 2022. **21**(9): p. 1050-1056.
104. Jørgensen, M., et al., *Understanding Superionic Conductivity in Lithium and Sodium Salts of Weakly Coordinating Closo-Hexahalocarborate Anions*. Chemistry of Materials, 2020. **32**(4): p. 1475-1487.
105. Paskevicius, M., et al., *First-order phase transition in the Li₂B₁₂H₁₂ system*. Physical Chemistry Chemical Physics, 2013. **15**(38): p. 15825-15828.
106. Dimitrievska, M., et al., *Carbon Incorporation and Anion Dynamics as Synergistic Drivers for Ultrafast Diffusion in Superionic LiCB₁₁H₁₂ and NaCB₁₁H₁₂*. Advanced Energy Materials, 2018. **8**(15): p. 1703422.
107. Pitt, M.P., et al., *Thermal Stability of Li₂B₁₂H₁₂ and its Role in the Decomposition of LiBH₄*. Journal of the American Chemical Society, 2013. **135**(18): p. 6930-6941.
108. Verdal, N., et al., *Complex high-temperature phase transitions in Li₂B₁₂H₁₂ and Na₂B₁₂H₁₂*. Journal of Solid State Chemistry, 2014. **212**: p. 81-91.
109. Her, J.-H., et al., *Crystal Structure of Li₂B₁₂H₁₂: a Possible Intermediate Species in the Decomposition of LiBH₄*. Inorganic Chemistry, 2008. **47**(21): p. 9757-9759.
110. Matsuo, M., et al., *Stabilization of lithium superionic conduction phase and enhancement of conductivity of LiBH₄ by LiCl addition*. Applied Physics Letters, 2009. **94**(8).

111. Maltsev, A.P., I.V. Chepkasov, and A.R. Oganov, *Order–Disorder Phase Transition and Ionic Conductivity in a Li₂B₁₂H₁₂ Solid Electrolyte*. ACS Applied Materials & Interfaces, 2023. **15**(36): p. 42511-42519.
112. Miyazaki, R., et al., *Room temperature lithium fast-ion conduction and phase relationship of LiI stabilized LiBH₄*. Solid State Ionics, 2011. **192**(1): p. 143-147.
113. Renaudin, G., et al., *Structural and spectroscopic studies on the alkali borohydrides MBH₄ (M = Na, K, Rb, Cs)*. Journal of Alloys and Compounds, 2004. **375**(1): p. 98-106.
114. Cronau, M., et al., *How to Measure a Reliable Ionic Conductivity? The Stack Pressure Dilemma of Microcrystalline Sulfide-Based Solid Electrolytes*. ACS Energy Letters, 2021. **6**(9): p. 3072-3077.
115. Huggins, R.A., *Simple method to determine electronic and ionic components of the conductivity in mixed conductors a review*. Ionics, 2002. **8**(3): p. 300-313.
116. Vadhva, P., et al., *Electrochemical Impedance Spectroscopy for All-Solid-State Batteries: Theory, Methods and Future Outlook*. ChemElectroChem, 2021. **8**(11): p. 1930-1947.
117. Arnbjerg, L.M., et al., *Structure and Dynamics for LiBH₄–LiCl Solid Solutions*. Chemistry of Materials, 2009. **21**(24): p. 5772-5782.
118. Ohta, S., T. Kobayashi, and T. Asaoka, *High lithium ionic conductivity in the garnet-type oxide Li_{7–X}La₃(Zr_{2–X}, Nb_X)O₁₂ (X=0–2)*. Journal of Power Sources, 2011. **196**(6): p. 3342-3345.
119. Kamaya, N., et al., *A lithium superionic conductor*. Nature Materials, 2011. **10**(9): p. 682-686.
120. Kotobuki, M., et al., *Fabrication of all-solid-state lithium battery with lithium metal anode using Al₂O₃-added Li₇La₃Zr₂O₁₂ solid electrolyte*. Journal of Power Sources, 2011. **196**(18): p. 7750-7754.
121. Liu, K., et al., *Molecular Design of a Highly Stable Single-Ion Conducting Polymer Gel Electrolyte*. ACS Applied Materials & Interfaces, 2020. **12**(26): p. 29162-29172.
122. Chen, K.-H., et al., *Dead lithium: mass transport effects on voltage, capacity, and failure of lithium metal anodes*. Journal of Materials Chemistry A, 2017. **5**(23): p. 11671-11681.
123. Xiao, Y., et al., *Electrolyte melt infiltration for scalable manufacturing of inorganic all-solid-state lithium-ion batteries*. Nature Materials, 2021. **20**(7): p. 984-990.

124. El Moutchou, S., et al., *Thermal stability of Lithium-ion batteries: Case study of NMC811 and LFP cathode materials*. Materials Today: Proceedings, 2022. **51**: p. A1-A7.
125. Zhang, K., et al., *Unveiling the roles of alumina as a sintering aid in Li-Garnet solid electrolyte*. International Journal of Energy Research, 2020. **44**(11): p. 9177-9184.
126. Wagner, A.C., et al., *Hierarchical Structuring of NMC111-Cathode Materials in Lithium-Ion Batteries: An In-Depth Study on the Influence of Primary and Secondary Particle Sizes on Electrochemical Performance*. ACS Applied Energy Materials, 2020. **3**(12): p. 12565-12574.
127. Wen, Y., et al., *Expanded graphite as superior anode for sodium-ion batteries*. Nature Communications, 2014. **5**(1): p. 4033.
128. Ekström, H. and G. Lindbergh, *A Model for Predicting Capacity Fade due to SEI Formation in a Commercial Graphite/LiFePO₄ Cell*. Journal of The Electrochemical Society, 2015. **162**(6): p. A1003.
129. Wang, A., et al., *Review on modeling of the anode solid electrolyte interphase (SEI) for lithium-ion batteries*. npj Computational Materials, 2018. **4**(1): p. 15.
130. Narla, A., et al., *Nanodiamond-Enhanced Nanofiber Separators for High-Energy Lithium-Ion Batteries*. ACS Applied Materials & Interfaces, 2023. **15**(27): p. 32678-32686.
131. Pacala, S. and R. Socolow, *Stabilization Wedges: Solving the Climate Problem for the Next 50 Years with Current Technologies*. Science, 2004. **305**(5686): p. 968-972.
132. Blyr, A., et al., *Self-Discharge of LiMn₂O₄/C Li-Ion Cells in Their Discharged State: Understanding by Means of Three-Electrode Measurements*. Journal of The Electrochemical Society, 1998. **145**(1): p. 194.
133. Tarascon, J.M. and M. Armand, *Issues and challenges facing rechargeable lithium batteries*. Nature, 2001. **414**(6861): p. 359-367.
134. Choi, J.W. and D. Aurbach, *Promise and reality of post-lithium-ion batteries with high energy densities*. Nature Reviews Materials, 2016. **1**(4): p. 16013.
135. Liu, B., J.-G. Zhang, and W. Xu, *Advancing lithium metal batteries*. Joule, 2018. **2**(5): p. 833-845.
136. Zhao, Q., S. Stalin, and L.A. Archer, *Stabilizing metal battery anodes through the design of solid electrolyte interphases*. Joule, 2021. **5**(5): p. 1119-1142.

137. Lagadec, M.F., R. Zahn, and V. Wood, *Characterization and performance evaluation of lithium-ion battery separators*. Nature Energy, 2019. **4**(1): p. 16-25.
138. Cavers, H., et al., *Perspectives on Improving the Safety and Sustainability of High Voltage Lithium-Ion Batteries Through the Electrolyte and Separator Region*. Advanced Energy Materials, 2022. **12**(23): p. 2200147.
139. Pan, R., et al., *Nanocellulose Modified Polyethylene Separators for Lithium Metal Batteries*. Small, 2018. **14**(21): p. 1704371.
140. Sun, S., et al., *Thermally Stable and Dendrite-Resistant Separators toward Highly Robust Lithium Metal Batteries*. Advanced Energy Materials, 2022. **12**(41): p. 2202206.
141. Wang, E., C.-H. Chiu, and P.-H. Chou, *Safety assessment of polyolefin and nonwoven separators used in lithium-ion batteries*. Journal of Power Sources, 2020. **461**: p. 228148.
142. Zhang, S.S., *A review on the separators of liquid electrolyte Li-ion batteries*. Journal of Power Sources, 2007. **164**(1): p. 351-364.
143. Bandhauer, T.M., S. Garimella, and T.F. Fuller, *A Critical Review of Thermal Issues in Lithium-Ion Batteries*. Journal of The Electrochemical Society, 2011. **158**(3): p. R1.
144. Choi, J. and P.J. Kim, *A roadmap of battery separator development: Past and future*. Current Opinion in Electrochemistry, 2022. **31**: p. 100858.
145. Deng, Y., et al., *Novel Thermotolerant and Flexible Polyimide Aerogel Separator Achieving Advanced Lithium-Ion Batteries*. Advanced Functional Materials, 2022. **32**(4): p. 2106176.
146. Patel, A., et al., *High Modulus, Thermally Stable, and Self-Extinguishing Aramid Nanofiber Separators*. ACS Applied Materials & Interfaces, 2020. **12**(23): p. 25756-25766.
147. Balazs, A.C., T. Emrick, and T.P. Russell, *Nanoparticle Polymer Composites: Where Two Small Worlds Meet*. Science, 2006. **314**(5802): p. 1107-1110.
148. Ding, H., et al., *TiO₂ quantum dots decorated multi-walled carbon nanotubes as the multifunctional separator for highly stable lithium sulfur batteries*. Electrochimica Acta, 2018. **284**: p. 314-320.
149. Hu, W., et al., *Heat-resistant Al₂O₃ nanowire-polyetherimide separator for safer and faster lithium-ion batteries*. Journal of Materials Science & Technology, 2023. **142**: p. 112-120.

150. Lei, D., et al., *Transformation of bulk alloys to oxide nanowires*. Science, 2017. **355**(6322): p. 267-271.
151. Arnault, J.-C., et al., *Surface chemical modifications and surface reactivity of nanodiamonds hydrogenated by CVD plasma*. Physical Chemistry Chemical Physics, 2011. **13**(24): p. 11481-11487.
152. Kidalov, S., F. Shakhov, and A.Y. Vul, *Thermal conductivity of sintered nanodiamonds and microdiamonds*. Diamond and Related Materials, 2008. **17**(4-5): p. 844-847.
153. Mochalin, V.N., et al., *The properties and applications of nanodiamonds*. Nature Nanotechnology, 2012. **7**(1): p. 11-23.
154. Li, Z., et al., *In-depth Li⁺ transportation in three-dimensionalized nanodiamond network for improved liquid and solid lithium metal batteries*. Nano Energy, 2023. **110**: p. 108370.
155. Polino, G., et al., *Nanodiamond-Based Separators for Supercapacitors Realized on Paper Substrates*. Energy Technology, 2020. **8**(6): p. 1901233.
156. Turcheniuk, K. and V.N. Mochalin, *Biomedical applications of nanodiamond (Review)*. Nanotechnology, 2017. **28**(25): p. 252001.
157. Zhou, Y., et al., *Synergistic effects of nanodiamond modified separators toward highly stable and safe lithium metal batteries*. Journal of Materials Chemistry A, 2021. **9**(29): p. 16046-16055.
158. Cheng, X.-B., et al., *Nanodiamonds suppress the growth of lithium dendrites*. Nature Communications, 2017. **8**(1): p. 336.
159. Liu, Y., et al., *An Ultrastrong Double-Layer Nanodiamond Interface for Stable Lithium Metal Anodes*. Joule, 2018. **2**(8): p. 1595-1609.
160. Raja, M., et al., *Thin, flexible and thermally stable ceramic membranes as separator for lithium-ion batteries*. Journal of Membrane Science, 2014. **471**: p. 103-109.
161. Saito, Y., et al., *Ion Transport in Separator Membranes of Lithium Secondary Batteries*. The Journal of Physical Chemistry C, 2015. **119**(9): p. 4702-4708.
162. Mochalin, V.N. and Y. Gogotsi, *Nanodiamond–polymer composites*. Diam. Relat. Mater., 2015. **58**: p. 161-171.
163. Daenen, M., et al., *Diamond Nucleation by Carbon Transport from Buried Nanodiamond TiO₂ Sol-Gel Composites*. Adv. Mater., 2009. **21**(6): p. 670-673.

164. Liao, M.Y., et al., *Nanodiamond formation by hot-filament chemical vapor deposition on carbon ions bombarded Si*. J. Cryst. Growth, 2002. **236**(1): p. 85-89.
165. Bai, P., et al., *Transition of lithium growth mechanisms in liquid electrolytes*. Energy & Environmental Science, 2016. **9**(10): p. 3221-3229.
166. Jana, A., D.R. Ely, and R.E. García, *Dendrite-separator interactions in lithium-based batteries*. Journal of Power Sources, 2015. **275**: p. 912-921.
167. Kume, A. and V.N. Mochalin, *Sonication-assisted hydrolysis of ozone oxidized detonation nanodiamond*. Diamond and Related Materials, 2020. **103**: p. 107705.
168. Zahn, R., et al., *Improving Ionic Conductivity and Lithium-Ion Transference Number in Lithium-Ion Battery Separators*. ACS Applied Materials & Interfaces, 2016. **8**(48): p. 32637-32642.
169. Jing, Y., Y. Shao, and H.L. Xin, *On The Efficacy of Cobalt Boride Coating on NMC-811 Cathode Under Vinylene Carbonate Additive, High Temperature and Air Shelving Conditions*. Journal of The Electrochemical Society, 2023. **170**(1): p. 010519.
170. Dai, T., et al., *Inorganic glass electrolytes with polymer-like viscoelasticity*. Nature Energy, 2023.
171. Yan, Y., et al., *A Lithium Amide-Borohydride Solid-State Electrolyte with Lithium-Ion Conductivities Comparable to Liquid Electrolytes*. Advanced Energy Materials, 2017. **7**(19): p. 1700294.
172. Klongkan, S. and J. Pumchusak, *Effects of Nano Alumina and Plasticizers on Morphology, Ionic Conductivity, Thermal and Mechanical Properties of PEO-LiCF₃SO₃ Solid Polymer Electrolyte*. Electrochimica Acta, 2015. **161**: p. 171-176.